New Methods of Characterizing Fractional Josephson Junctions and Majorana Excitations

Von der Fakultät für Elektrotechnik, Informationstechnik, Physik
der Technischen Universität Carolo-Wilhelmina zu Braunschweig

zur Erlangung des Grades eines Doktors

der Naturwissenschaften (Dr. rer. nat.)

genehmigte Dissertation

von Daniel Michael Frombach

aus Uelzen

eingereicht am: 16.09.2020

Disputation am: 03.02.2021

1. Referent: Prof. Dr. Patrik Recher
2. Referentin: Prof. Dr. Ewelina Hankiewicz

Druckjahr: 2021

Dissertation an der Technischen Universität Braunschweig,
Fakultät für Elektrotechnik, Informationstechnik, Physik

Abstract

In this thesis we propose and discuss new ways to probe and characterize fractional Josephson junctions and Majorana excitations forming inside of such junctions.

First we propose a Josephson junction based on silicene. By using the buckled structure of silicene, topological edge states can be defined using electric fields. When mediating the Josephson effect with such edge states, the resulting Josephson junction can be tuned electrically between a fractional junction hosting two Majorana excitations and a nonfractional junction hosting no Majorana excitations. An experimental setup to use this effect as an indicator for the topology of the junction is proposed and discussed.

Such signatures will typically only be visible in measurements if the quasiparticle poisoning is slow in these junctions. We analyze the effects that such poisoning events have on the dynamics of fractional Josephson junctions. Using a Fokker-Planck equation approach, we consider thermal noise in the analysis as well as discuss the effects poisoning events have on the current voltage characteristic in the zero temperature limit. Experimental schemes to measure the poisoning rate through voltage measurements are proposed for different parameter regimes. Extended junctions where two sets of spin-helical topological edge states mediate the Josephson effect are discussed as well. Considering a constriction between these two sets of edge states allows for tunneling of electrons between these two edges.

Many of the proposed setups use the fact that the Josephson junction is in the long junction regime. We propose a setup in which the topological edge states mediating the fractional Josephson effect are coupled to additional states. As an example we consider the cases where the edge states either couple to an additional nondispersive channel or to a single level quantum dot.

Due to this coupling, the electrons and holes forming the Andreev bound states pick up an additional phase during one round trip, which alters their energy phase relation. The resulting setups mimic junctions with an effective length that is longer than the physical length of the junction. We characterize these junctions including coupling to additional states by an effective junction length and consider multiple limiting cases. By employing such coupling short junctions can potentially be tuned to the long junction regime, which would make many of the proposed measurements possible even in junctions that are physically in the short junction regime.

This thesis also contains a brief overview of the current experimental situation surrounding this field of study as well as a short review of the Kane-Mele model as an example model featuring a quantum spin Hall insulating phase including spin-helical topological edge states.

Zusammenfassung

In dieser Dissertation schlagen wir neue Methoden zur Untersuchung und Charakterisierung sowohl von fraktionalen Josephson Kontakten als auch von Majorana Anregungen, welche sich in solchen Kontakten bilden, vor und diskutieren diese.

Als erstes schlagen wir einen Josephson Kontakt in Silicen vor. Aufgrund der wellenförmigen Struktur von Silicen können wir topologische Randkanäle mit Hilfe von elektrische Feldern definieren. Wenn der Josephson Effekt über diese topologischen Randkanäle vermittelt wird, kann der resultierende Josephson Kontakt elektrisch zwischen einem fraktionalen Josephson Kontakt, in welchem sich zwei Majorana Anregungen bilden, und einem nicht fraktionalen Josephson Kontakt, in welchem sich keine Majorana Anregungen bilden, geschaltet werden. Ein experimenteller Aufbau, in welchem dieser Effekt als Indikator für die Topologie des Kontaktes genutzt wird, wird vorgeschlagen und diskutiert.

Solche Signaturen sind in Messungen typischerweise nur sichtbar, falls die Quasiteilchenvergiftung langsam ist. Wir untersuchen den Effekt, der eine solche Vergiftung auf die Dynamik von fraktionalen Josephson Kontakten hat. Mit Hilfe eines Ansatzes über die Fokker-Planck Gleichung betrachten wir thermisches Rauschen. Ebenfalls wird der Effekt von Quasiteilchenvergiftung auf die Strom-Spannungs-Charakteristik im Limes verschwindender Temperatur untersucht. Experimentelle Konstruktionen zum Messen der Quasiteilchenvergiftungsrate über Spannungsmessungen werden für verschiedene Parameterbereiche vorgeschlagen. Erweiterte Kontakte, wo zwei Sätze an Spin helikalen topologischen Randkanälen den Josephson Effekt vermitteln, werden ebenfalls diskutiert. Wenn weiterhin eine Verengung in diesen Randkanäle angenommen wird, wird Tunneln von Elektronen zwischen diesen zwei Sätzen an Randkanälen möglich.

Viele dieser vorgeschlagenen Konstruktionen basieren darauf, dass sich die Josephson Kontakte in dem langen Kontakt Regime befinden. Wir schlagen einen Aufbau vor, in dem die topologischen Randkanäle, welche den fraktionalen Josephson Effekt vermitteln, an weitere Zustände gekoppelt werden. Als Beispiele betrachten wir die Fälle, wo die Randkanäle entweder an einen weiteren nicht dispersiven Kanal oder an einen Quantenpunkt mit einem einzigen Zustand gekoppelt werden. Aufgrund dieser Kopplung sammeln die Elektronen und Löcher, welche die gebundenen Andreev Zustände bilden, in einem vollen Umlauf eine weitere Phase auf, wodurch sich ihre Energie-Phase-Beziehung verändert. Die resultierenden Kontakte ähneln solchen, welche länger sind als die ihnen unterliegenden Kontakte physisch sind. Wir charakterisieren diese Kontakte mit Kopplungen an weitere Zustände über eine effektive Länge und betrachten verschiedene Grenzfälle. Mit Hilfe solcher Kopplungen können kurze Kontakte potentiell in den langen Kontakt Regime gebracht werden, was viele der vorgeschlagenen Messungen selbst in Kontakten, welche sich physisch im kurzen Kontakt Regime befinden, möglich machen würde.

Diese Dissertation enthält ebenfalls sowohl einen kurzen Überblick über die experimentelle Lage des umliegenden Forschungsfeldes als auch eine kleine Übersicht des Kane-Mele Modells als ein Beispiel für ein Modell, welches eine Quanten-Spin-Hall isolierende Phase inklusive Spin helikalen topologischen Randkanälen besitzt.

List of publications

1. *Electrically controlled crossover between 2π- and 4π- Josephson effects through topologically-confined channels in silicene*

   D. Frombach, S. Park, A. Schroer, P. Recher

   Phys. Rev. B **98**, 205305 (2018)

2. *Transport signatures of Majorana bound states in superconducting hybrid structures*

   A. Schuray, D. Frombach, S. Park, P. Recher

   Eur. Phys. J. Spec. Top. **229**, 593 (2020)

3. *Quasiparticle poisoning effects on the dynamics of topological Josephson junctions*

   D. Frombach, P. Recher

   Phys. Rev. B **101**, 115304 (2020)

Acknowledgments

First and foremost I would like to thank my supervisor Prof. Dr. Patrik Recher. He not only provided me with the opportunity to work in this exciting field, but also took time out of his busy schedule to have many long and fruitful discussions with me and our collaborators. This opportunity and his focus on details are part of what made this thesis a possibility.

I would also like to thank Dr. Alexander Schroer, Dr. Sunghun Park, and Alexander Schuray who were directly involved in some of the projects discussed in this thesis. A special mention is warranted for Alexander Schuray, who always had an open ear for difficult and fundamental questions surrounding our joint field of study. Getting to the bottom of these questions together with him in many discussions played a significant role in my understanding of the field and hence the creation of this thesis.

My colleagues deserve a special thanks as they made my time in Braunschweig not just scientifically enlightening, but also fun and also broadened my horizon outside of science.

Finally, I would like to thank Prof. Dr. Ewelina Hankiewicz for agreeing to coreferee this thesis as well as Prof. Dr. Peter Lemmens for chairing the defense exam.

Contents

1

Introduction

The beginning of the last century saw a big revolution in science. With many experimental results contradicting the classical theories of the time much work needed to be done to reconcile these experiments with theoretical models. This work ultimately culminated in the discovery of quantum mechanics in the early 1920s. While quantum mechanics was able to predict experimental results with very high accuracy, its rules and more importantly its interpretation is often times counterintuitive and still puzzle many physicists today. This counterintuitive nature of quantum mechanics has driven physicists to try to gain full control over individual quantum systems in order to probe its quantum me-

chanical properties.

While this development was mostly driven by general curiosity, an interesting question arose. Can these individual quantum systems be used to perform computations such as classical physical systems can perform classical computations? For instance, Feynman proposed to use quantum mechanical systems to simulate quantum properties [1]. In order to describe quantum mechanical problems in a classical computer, an exponentially large number of complex values are needed. For instance, in order to describe N two level systems, e.g. electronic spins, 2^N complex numbers are needed to fully describe the system quantum mechanically. This already exceeds the memory capacity of even the largest supercomputers for multiple tens of spin 1/2's. By using quantum mechanical systems to perform these simulations they can potentially be made accessible.

While this example of a quantum mechanical calculation is of particular interest to physicists, there also exist examples of quantum computations of much broader interest. The prime factorization of an m-digit integer when performed on a classical computer takes time on the order of $\sim \exp(m^{1/3})$ to complete [2]. The important thing to note here is that the time it takes to find the prime factorization of such an integer increases exponentially with the digit length of said integer. For long integers it is therefore computationally unfeasible to calculate these prime factors. On the other hand, it is computationally very simple, to the point of being possible to be done manually on a piece of paper, to verify that given prime factors multiply to a specific integer. This asymmetry in computational complexity is the foundation of many encryption schemes used today in everyday life. One of the most widely known quantum algorithm, often called the Shor algorithm after its founder, removes exactly this asymmetry. When performed on a quantum computer, it can find the prime factors of an m-digit integer in times on the order of $\sim m^2 \log(m) \log(\log(m))$ [2, 3]. This time is polynomial in m and

is therefore much smaller for large integers. As many encryption schemes depend on this problem to be hard to the point of being impossible to do on a classical computer, quantum computation has garnered general interest both inside and outside of science.

While the above examples suggest that quantum computers are inherently more powerful than classical computers, this is very much still an open question [4], one that will not be addressed in this thesis. The rest of this introductory chapter organizes as follows. We will first briefly review quantum computation in general and address current difficulties in building a quantum computer. Following that we shift our focus to the field of nonabelian anyons and how they relate to quantum computation. As an example of nonabelian anyons we will focus on Majorana excitations next and discuss certain properties of nonabelian anyons in a concrete example. We will then briefly review the current situation on theoretical and experimental work that has been done to create and manipulate Majorana excitations. Having set the stage and described the context this thesis exists in, a brief overview of how this thesis is structured will be given. The nature of an introductory chapter, especially one that aims to cover multiple different fields of study, is necessarily to be unthorough, glossing over many details, and sometimes be a little bit vague. For the interested reader additional literature will be cited in the respective sections, which can be used as a jumping-off point to enter deeper into the respective fields.

1.1 Quantum Computation

A quantum computation in the most general sense can be thought of as three different steps: initialization, unitary evolution, and measurement [2, 5]. In the first step a quantum me-

chanical system is prepared in the state $|\psi_0\rangle$. This state can be thought of as the input to a quantum mechanical computation. In the second step this state gets unitarily evolved to a state $U|\psi_0\rangle$. This unitary evolution U can be achieved, for instance, by the time evolution of a state in a given quantum mechanical system as the time evolution of closed quantum systems is always unitary. This step can be thought of as performing the calculation on the quantum mechanical state. Finally, the final state $U|\psi_0\rangle$ gets measured and yields classical information.

To see how such a general process can get implemented it is helpful to first think of how computations are done on a classical computer. The most basic unit of information in a classical computer is a bit, a number, which has either the value 0 or 1. Physically, it can get implemented through different systems that can be in either of two states, such as flip-flop circuits, two directions of magnetic polarization, or two distinct voltage levels. These two states then get associated with either 0 or 1. Computations can be performed on these bits by using gates, which can change the value of individual bits. An example is the NOT gate, which transforms a 0 to a 1 and vice versa. Other gates like the AND gate combine two bits into one and implement basic truth tables. More complicated computations on multiple bits can be performed by combining these gates. It can be shown that only a single gate, e.g. the NAND gate, is necessary to build any arbitrary computation on classical bits [4]. Such gates are known as universal gates and will play an important roll in determining the computations needed in general quantum computers.

The quantum mechanical analogon to these bits is the quantum bit, or qubit for short. It is physically represented by a two level quantum system such as an electron spin. The two states in question are usually denoted with $|0\rangle$ and $|1\rangle$ and are sometimes called the computational basis. Because the system is quantum mechanical, the qubit cannot only be in these two states but in

any superposition of the two

$$|\psi\rangle = \alpha\,|0\rangle + \beta\,|1\rangle \tag{1.1}$$

where α and β are two complex numbers with the constraint $|\alpha|^2 + |\beta|^2 = 1$. This fact that qubits can be in superpositions of the computational basis, gives a first hint towards qubits somehow *"storing more information"* than a classical bit. In fact, because both α and β are complex numbers they can take an infinite number of different values, such that we should theoretically be able to encode an infinite amount of classical information (infinite number of classical bits) into one qubit. However, we need to measure the qubit at the end of the calculation to obtain classical information. A single measurement will only yield either 0 or 1 and the explicit values for α and β could only ever be obtained, if we had an infinite number of qubits prepared in the same state that we could measure. However, this superposition lies at the heart of why quantum algorithms are sometimes much faster than their classical counterparts.

Now that we have a basic understanding of the fundamental unit of information in quantum computers we can turn our attention to performing computations on them, i.e. manipulating qubits through gates. The quantum mechanical analogon to classical gates is sometimes called quantum gates[1] and facilitates changes to one or more qubits. Because the qubit state needs to stay normalized during and after the calculation, these gates are unitary transformations. As an example we can again take a look at the NOT gate. In the classical case this gate flipped a single bit such that $0 \to 1$ or $1 \to 0$. In the quantum mechanical case we may define a NOT gate to act in a manner that changes $|0\rangle \to |1\rangle$ and $|1\rangle \to |0\rangle$. When expressing the qubit states as vectors, i.e. $|0\rangle \to (1,0)^T$ and $|1\rangle \to (0,1)^T$, the NOT gate can simply be expressed as the Pauli matrix σ_x. How such gates are

[1] We will drop the "quantum" and only call them gates from here on.

physically implemented depends greatly on the physical realization chosen for the qubit but generally involves a unitary time evolution of a quantum mechanical system.

In the classical case we saw that only a single gate, the NAND gate, was necessary to any arbitrary bit manipulation. In quantum computation there is no single gate that is universal. However, it can be shown that any unitary operation on multiple qubits can be constructed by combining two types of gates, a two qubit gate called the CNOT (controlled NOT) gate and single qubit gates [4]. The CNOT gate can be summarized as $|A, B\rangle \rightarrow |A, A \oplus B\rangle$ where $\oplus$ is addition modulo 2. This gate will flip the second qubit (target qubit), i.e. perform a NOT gate, if and only if the first qubit (control qubit) is $|1\rangle$. The single qubit gates can be further broken down and it can be shown that any arbitrary single qubit gate can be built in a fault-tolerant way out of two single qubit gates, the Hadamard gate H and the $\sigma_z^{1/4}$ gate [6]. While the second gate can be understood as a $\pi/4$ rotation around the z-axis in a Bloch sphere, the first is a bit more complicated and first rotates the state by $\pi/2$ around the y-axis and then by π around the x-axis. A universal set of quantum gates can therefore be given by the set

$$\{H, \sigma_z^{1/4}, \text{CNOT}\} \tag{1.2}$$

out of which any arbitrary multi-qubit manipulation can be built.

Equipped with an understanding of qubits and logic gates we can address the question of how quantum computers may sometimes perform faster than their classical counterparts. A good example of this is *"quantum parallelism"* [4, 7]. Let $f : \{0, 1\} \rightarrow \{0, 1\}$ be a function operating on a single bit. Using gates, it is possible to implement a quantum circuit that operates on two qubits and transforms them according to $|A, B\rangle \rightarrow |A, f(A) \oplus B\rangle$ where $\oplus$ again is addition modulo 2. When we initialize the first qubit in the superposition $(|0\rangle + |1\rangle)/\sqrt{2}$ and the second qubit in the state $|0\rangle$ is is easy to verify that the output of the circuit

will be

$$\frac{|0, f(0)\rangle + |1, f(1)\rangle}{\sqrt{2}}. \tag{1.3}$$

Part of the output contains $f(0)$ while the other part contains $f(1)$. In a sense, both outputs have been calculated in parallel. This is different from classical parallelism where multiple circuits calculate the output of f for different input values in parallel. In quantum parallelism, only a single circuit evaluated a single calculation and still obtained information about both $f(0)$ and $f(1)$.

One has to keep in mind that when we measure this state we measure one state containing only one of $f(0)$ and $f(1)$. If we measure the first qubit to be $|0\rangle$, then we can obtain $f(0)$ by measuring the second qubit. After that measurement the state collapsed onto $|0, f(0)\rangle$ and the information about $f(1)$ is lost. We can however adapt the above described circuit to obtain a global property of the function f. Instead of initializing the second qubit in the state $|0\rangle$ we initialize it to also be in a superposition $(|0\rangle - |1\rangle)/\sqrt{2}$. Furthermore, we apply the Hadamard gate H to the first qubit at the end of the calculation. A straightforward calculation will show that the final state will be

$$\pm\, |f(0) \oplus f(1)\rangle \left(\frac{|0\rangle - |1\rangle}{\sqrt{2}} \right). \tag{1.4}$$

The first qubit now contains the global property $f(0) \oplus f(1)$, which can be obtained by measuring the first qubit. So while the end result of such a quantum computation will again only give a single bit of classical information, we can obtain a global property of the function f with just a single evaluation of the calculation. To obtain the same result classically we would have to perform two calculations, one to obtain $f(0)$ and one to obtain $f(1)$ to get the same global property. This method of obtaining a global property out of the function f is called Deutsch's algorithm

[7–9] and is a good example of how additional steps are generally needed to make the computational advantages of quantum computations accessible to measurements, which is necessary to obtain useful information[2].

Currently the biggest obstacle to quantum computation is errors [2]. Errors occur during calculations and while storing data both in quantum and classical computations. In classical computations this is usually addressed by storing the information in a redundant way. By checking against this redundant information erroneous bit flips, for instance, can be detected and corrected. In quantum computations this is complicated by the fact that when measuring a qubit, it collapses onto either $|0\rangle$ or $|1\rangle$ and the superposition of the qubit is destroyed. However, error correction schemes are possible in quantum computers [10–13], for instance, by saving one qubit in three two level systems and associating $|0\rangle \equiv |000\rangle$ and $|1\rangle \equiv |111\rangle$ [2]. Random bit flip errors can now be detected by measuring whether or not all three two level systems are in the same state. Because we never need to measure the qubit, its superposition never gets destroyed by this error correction scheme.

Other sources of errors, which are not present in classical bits, come from unprecise operations and decoherence. When we want to rotate a qubit by $\pi/2$, we may instead rotate it by $\pi/2 + \epsilon$ where ϵ is a small but possibly finite angle. Such errors are present due to the limited precision to which we can physically manipulate the system. Furthermore, because the qubit couples to the environment over which we have no information, the qubit can turn from a pure state to a mixed state. Because we cannot measure the state of the environment, information is lost to decoherence [2]. These types of errors arise due to our limited ability to isolate the qubit from the environment.

As the error correcting schemes can be noisy and contain

[2] A more thorough discussion of quantum parallelism and Deutsch's algorithm is presented in [4].

errors themselves, there exists a threshold for how many errors a quantum computation can withstand before it will fail due to too many errors. The threshold depends on the particular error correction scheme in question but ranges around $\sim 10^{-4} - 10^{-6}$ so that we will need to be able to perform calculations such that we have only 1 error per $\sim 10^4 - 10^6$ operations [2, 14].

1.2 Nonabelian Anyons

Having seen the potential prospects of quantum computation and also its main obstacle in form of errors we now turn our attention to exotic particles called nonabelian anyons. At first these two topics will seem disconnected from each other. However, as we will see at the end of this section, these particles can be used to implement qubits, which are intrinsically robust against errors. To understand the existence of these particles we must first go back to the distinction between fermions and bosons. When exchanging two identical particles at positions $\boldsymbol{x}_{1,2}$ adiabatically, the wave function describing both particles $\psi(\boldsymbol{x}_1, \boldsymbol{x}_2)$ can change its sign $\psi(\boldsymbol{x}_1, \boldsymbol{x}_2) \to \pm\psi(\boldsymbol{x}_1, \boldsymbol{x}_2)$. If the sign of the wave function changes, we call these particles fermions, if it does not, we call them bosons.

We can reformulate this in terms of particle paths in three spatial dimensions. Exchanging two particles twice is equivalent to moving one particle around the other while the other stays still [2]. This path that the first particle takes can be adiabatically modified to one where the first particle also did not move at all. To see this imagine the path of the particle as a piece of string whose ends come together at the initial (and final) position of the particle forming a closed loop around the other particle. When we start to slowly pull on the ends of the string while pinching

the string together at the initial position of the first particle, the loop slowly shrinks. Because we fixate the string at the initial position of the particle, these new loops are also valid trajectories of the first particle. This can be continued until the loop closes entirely, which describes the path where the first particle also did not move at all. The path where one particle encircles the other is therefore adiabatically equivalent to the path where both particles stand still [2]. The final states of both paths therefore have to be described by the same wave function. Because of this, an exchange of the two particles, which is *"half of"* the process described above, can only result in a change of sign of the wave function.

The situation becomes very different in two spatial dimensions [2, 15–17]. Again, let us imagine the path of the first particle moving around the second as a piece of string. Pulling on the ends of the string again makes the loop shrink. However, as soon as the string touches the second particle, we can no longer make the loop smaller without having to rip the string apart at the second particle, move these parts to the other side of the second particle, and reattach them on the other side. Only then can we close the loop further. This fundamental difference between loops encircling another particle and loops not encircling another particle is why these two paths are called topologically different. Because of this, the question *"How many times did one particle encircle the other?"* has a well-defined answer, unlike in three spatial dimensions. As these situations are different, their wave functions can also differ. Because the probability density must stay unchanged (the initial and final positions of the indistinguishable particles are the same), the wave function can only pick up a phase 2θ when moving one particle around another $\psi(\boldsymbol{x}_1, \boldsymbol{x}_2) \to e^{i2\theta}\psi(\boldsymbol{x}_1, \boldsymbol{x}_2)$. Like before, the exchange of these two particles is *"half of"* this path such that when two particles

get exchanged their wave function can change according to

$$\psi(\boldsymbol{x}_1, \boldsymbol{x}_2) \to e^{i\theta}\psi(\boldsymbol{x}_1, \boldsymbol{x}_2). \tag{1.5}$$

If this phase is either 0 or π (mod 2π), the particles are bosons or fermions respectively. However, this phase can also differ from 0 and π. Such particles, which pick up a phase $\theta \neq 0, \pi$ upon exchange, are called anyons with statistics θ.

When generalizing eq. (1.5) to N particles, this relation can be thought of as a one-dimensional representation of the braid group $\mathcal{B}_N$ [2]. The braid group $\mathcal{B}_N$ is similar to the permutation group S_N but differs from it such that individual elements of the braid group $\sigma_i \in \mathcal{B}_N$ do not have to square to the unity operation $\sigma_i^2 \neq 1$. As the wave function only picks up a phase when two particles are braided and the phases of different braiding operations commute (multiplicative phase factors commute), the corresponding particles are called abelian anyons.

In the above example we only considered one wave function $\psi(\{\boldsymbol{x}_i\})$ describing N anyons at positions $\boldsymbol{x}_i$. There can however be multiple degenerate states $\psi_\alpha(\{\boldsymbol{x}_i\})$ with $\alpha = 1, \ldots, g$ where g is the degeneracy describing the particles at the same positions. When this is the case, higher-dimensional representations of the braid group are possible where the braid operations are represented by $g \times g$ unitary matrices acting on the subspace spanned by the degenerate wave vectors $\psi_\alpha(\{\boldsymbol{x}_i\})$. These unitary matrices can be noncommuting. When this is the case for at least one pair of matrices, the corresponding anyons are called nonabelian anyons.

The connection to quantum computing now becomes more apparent. When we build a qubit out of states from the degenerate subspace spanned by $\psi_\alpha(\{\boldsymbol{x}_i\})$, unitary operations can be performed on them by braiding the corresponding particles around one another [2]. Furthermore, unitary operations in this subspace can only be achieved by braiding the particles around each other, given that states in this subspace are separated to

other states by an energy gap. Local perturbations can therefore not have a finite matrix element in this subspace, which makes qubits built out of nonabelian anyons particularly fault-tolerant [2]. The precise path that the particle took around another particle is also not important to the unitary evolution. The only important question is whether or not two particles were braided. Either two particles were exchanged, or they were not exchanged. There is no in-between. This therefore also removes small errors acquired during the unitary operations [2, 18].

The picture for topological quantum computations is therefore the following. Qubits are made out of multiple nonabelian anyons, which are far enough apart from each other to consider them independent of each other, and are initialized, for instance, through measurements. The computation is then performed by physically moving the particles around each other (braiding them), which performs unitary evolutions in the underlying degenerate subspace (see Sec. 1.3). Finally, the qubits can be measured, for instance, by moving them close together such that the degeneracy of the subspace spanned by $\psi_\alpha(\{\boldsymbol{x}_i\})$ is lifted. An energy measurement can now distinguish these states and determine the final state of the qubit.

1.3 Majorana Excitations

Having seen how nonabelian anyons can be beneficial to quantum computing let us turn to a specific example of such a nonabelian anyon, the Majorana excitation. For this we have to go back to the Dirac equation[3]

$$(i\partial\!\!\!/ - m)\psi = 0 \tag{1.6}$$

[3] We have used natural units $\hbar = c = 1$ here.

which was published back in 1928 by Dirac to describe electrons [19]. A remarkable feature of this equation is that it not only describes particles itself, but also their antiparticles. In the case of the electron it therefore also describes positrons. However, nine years later Majorana found different solutions to this equation, which could be purely real [20]. This meant that the corresponding particle would be its own antiparticle, similar to photons. The existence of Majorana particles in nature is still an open question [21]. Majorana himself proposed the neutrino as a possible candidate. However, the experimental picture is far from clear-cut. Another proposal comes from supersymmetry where it is predicted that every boson must have a heavier fermion counterpart. The counterpart to the photon, the photino, is predicted to mimic the properties of the photon and is thus its own antiparticle, a Majorana particle [21].

Despite the existence of Majorana particles in nature being unclear, there have been many predictions of Majorana particles forming as many body quasiparticle excitations in condensed matter [22–31]. These excitations follow the anticommutation relation

$$\{\gamma_\alpha, \gamma_\beta\} = 2\delta_{\alpha\beta} \tag{1.7}$$

as well as the Majorana condition $\gamma_\alpha^\dagger = \gamma_\alpha$, which follows from the fact that Majorana excitations are their own antiparticle. When these operators furthermore commute with a Hamiltonian describing a certain physical system $[H, \gamma_\alpha] = 0$, these excitations are eigenstates of the Hamiltonian that lie at zero energy and the corresponding Majorana excitations are called Majorana zero modes.

To see that these excitations are nonabelian anyons and how they can be used to build qubits, consider a system in which four localized Majorana zero modes γ_i $(i = 1, 2, 3, 4)$ can be freely moved in two spatial dimensions [32]. We can pair these Majo-

rana excitations

$$a_{\alpha\beta} = \frac{1}{2}(\gamma_\alpha - i\gamma_\beta), \tag{1.8}$$

which is only a change of basis. These excitations $a_{\alpha\beta}$ follow typical fermionic anticommutation relations so that the particle $a_{\alpha\beta}$ is usually called a Dirac fermion. However, unlike other Dirac fermions like electrons, the particles $a_{\alpha\beta}$ are nonlocal in space as long as the constituent Majorana excitations γ_α and γ_β are separated in space. This nonlocal Dirac fermion can either be occupied or nonoccupied, which determines the two degenerate states $|\pm\rangle$ of different parity that the combination of the two Majorana excitations can be in. The parity operator

$$P_{\alpha\beta} = 1 - 2a^\dagger_{\alpha\beta}a_{\alpha\beta} = i\gamma_\alpha\gamma_\beta \tag{1.9}$$

distinguishes between the two parity states.

In order to be able to perform computations with these excitations, we need to consider an exchange of two such excitations. Because the operators γ_α are hermitian, the exchange of two operators can at most change their signs. The total parity $P_{\alpha\beta} = i\gamma_\alpha\gamma_\beta$ of the system cannot change during this exchange process as excitations are only moved around in real space. The signs picked up by the two operators must therefore be opposite to each other. We end up at the transformation

$$\gamma_\alpha \to \gamma_\beta, \qquad \gamma_\beta \to -\gamma_\alpha \tag{1.10}$$

after exchanging the excitations γ_α and γ_β [33].

Now all the necessary pieces are in place to build a qubit out of four Majorana excitations. Consider the first two excitations to pair up to the two parity states $|\pm\rangle$ and the last two excitations to pair up to another set of parity states. The state of all four excitations can be one of the four degenerate states $|\pm\rangle\,|\pm\rangle$. As braiding cannot change the overall parity of the system, such operations are limited to a two-dimensional subspace

spanned by two states of equal total parity. Let's assume we initialize the system in the state $|+\rangle|-\rangle$ such that we are restricted to the odd parity sector. We can associate $|0\rangle \equiv |+\rangle|-\rangle$ and $|1\rangle \equiv |-\rangle|+\rangle$ for our computational basis. When moving excitation γ_2 around excitation γ_3 both operators pick up a sign. Both the parity P_{12} and P_{34} will therefore change so that the state $|0\rangle$ will be transformed to $|1\rangle$ and vice versa. Moving the second excitation around the third therefore performs a NOT gate on the qubit. It is straightforward to verify that $\sigma_x = i\gamma_2\gamma_3 = P_{23}$ is the corresponding operator performing this unitary evolution. As the exchange of excitations γ_2 and γ_3 is *"half of"* this full braid, the operator corresponding to this exchange B_{23} must fulfill $B_{23}^2 = \sigma_x$. The operator that fulfills this condition is given by $B_{23} = \sqrt{i/2}(1 + \gamma_2\gamma_3)$ and takes the computational basis states to superpositions thereof [32].

Similar considerations show that moving the first excitation around the second results in the basis states evolving according to $\sigma_z = i\gamma_1\gamma_2 = P_{12}$ while exchanging the two excitations performs the operation $B_{12} = \sqrt{i/2}(1 + \gamma_1\gamma_2)$ with $B_{12}^2 = \sigma_z$. As these braids do not commute $[B_{12}, B_{23}] = i\gamma_1\gamma_3$, the corresponding particles, the Majorana excitations, are nonabelian anyons. Combining these braids we can perform more complicated operations such as the Hadamard gate $H = e^{-i\pi/4}B_{12}B_{23}B_{12}$ and even the CNOT gate using an ancilla qubit [32].

As both the Hadamard gate H as well as the CNOT gate can be performed via braiding, this only leaves the $\pi/4$ rotation around the z-axis in the Bloch sphere $\sigma_z^{1/4}$ to make a universal set of quantum gates. This gate however cannot be achieved via braiding the Majorana excitations. We will therefore not be able to perform every operation on the chosen qubit in a topologically protected manner, i.e. through braiding. For that, we would have to take parafermions, nonabelian anyons that can be thought of as a sort of generalization of Majorana excitations [34–38], to build our qubit. However, because parafermions are even more

exotic than Majorana excitations, much research up to now has focused on Majorana excitations regardless.

1.4 Experimental Situation

Having seen how nonabelian anyons like Majorana excitations can be used to implement fault-tolerant quantum computation, we turn our attention to how to realize such Majorana excitations in physical systems. In condensed matter systems the fundamental particle is the electron and quasiparticle excitations are made out of superpositions of electrons[4]. Mathematically, we can always perform the change of basis [39]

$$c = \frac{1}{2}(\gamma_1 + i\gamma_2), \qquad c^\dagger = \frac{1}{2}(\gamma_1 - i\gamma_2) \tag{1.11}$$

where we have written the electronic excitation as a superposition of γ_1 and γ_2 excitations. This transformation can be inverted

$$\gamma_1 = c^\dagger + c, \qquad \gamma_2 = i(c^\dagger - c) \tag{1.12}$$

to see that these excitations are equal weight superpositions of electrons and holes. Using the fact that c are fermionic operators, it is straightforward to show that the operators γ_α are hermitian and fulfill

$$\{\gamma_\alpha, \gamma_\beta\} = 2\delta_{\alpha\beta} \tag{1.13}$$

where $\alpha, \beta = 1, 2$. The excitations γ_α are therefore Majorana excitations.

[4] We restrict ourselves to electronic excitations as there are also other types of nonelectronic excitations like phonons (vibrational modes) and magnons (magnetic modes).

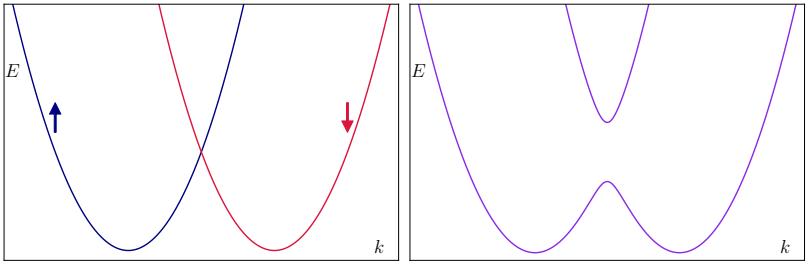

Figure 1.1: Dispersion relation of electrons in a nanowire with (right) and without (left) a magnetic field aligned perpendicular to the spin-orbit interaction direction.

To find systems in which such excitations are eigenstates we again note that Majorana excitations are equal weight superpositions of electrons and holes. Such states naturally occur in superconductors, which is why current proposals all include superconductors in their systems. Another ingredient comes from the toy model proposed by Kitaev [23]. The system needs to be effectively spinless. While Kitaevs toy model assumed a single spin polarization in combination with p-wave superconductivity, other approaches combining spin-helical systems with s-wave superconductivity have emerged [24–27].

One such system was proposed by Oreg *et al.* [27][5]. This proposal is based on nanowires where the electron movement is restricted to one dimension. The dispersion relation of the electrons is a parabola, which is degenerate due to spin. Upon including spin-orbit interaction, the two parabolas associated with the two spin directions get shifted in momentum space such that they cross at the Γ point in momentum space (Fig. 1.1). When a magnetic field perpendicular to the direction of the spin-orbit interaction is applied to the nanowire, states of these two spin

[5] It should be noted that Lutchyn *et al.* [26] have proposed a very similar setup around the same time.

directions mix and an energy gap opens at the Γ point. Tuning the chemical potential such that it lies inside of this gap, only two states exist around this chemical potential, one state with negative group velocity and a given spin polarization, and another state with positive group velocity and a spin polarization exactly opposite to the first. For low energies around the chemical potential, the system is therefore spin-helical. When this wire is brought into close proximity to an s-wave superconductor, this superconductivity is induced in the wire through the proximity effect. The two states of opposite spin polarization get paired and a superconducting gap opens around the chemical potential. It has been predicted that inside of this superconducting gap two Majorana excitations lie at zero energy, which are furthermore localized at the ends of the wire [27].

This proposal has been implemented first by Mourik *et al.* by growing the superconductor niobium titanium nitride (NbTiN) on top of indium antimonide (InSb) nanowires and connecting it to a normal conducting electrode in order to perform tunneling spectroscopy [40]. The existence of Majorana excitations should result in quantized differential conductance peaks [41, 42]. Mourik *et al.* reported on the existence of such zero bias peaks in the differential conductance for a wide array of magnetic field strengths and bias voltages. Furthermore, if the magnetic field vanishes, gets aligned perpendicular to the wire, or if the superconductor is replaced with a normal metal, these zero bias peaks will vanish, which is all consistent with these peaks resulting from Majorana excitations.

A second setup in which experimental signatures of Majorana excitations were found was built by depositing a one-dimensional chain of iron atoms on top of a superconducting lead surface [43, 44]. Scanning tunneling microscopy again showed zero bias peaks at the ends of the chains. Furthermore, spatially resolved tunneling spectroscopy showed that these peaks were localized at the ends of the chain and were not present in the bulk of the

chain.

Another proposal was published by Fu and Kane in 2009 in which a superconductor is brought into close proximity to spin-helical topological edge states of a quantum spin Hall insulator [25]. By forming both the quantum spin Hall insulator and the superconductor in a ring shape, the superconductor can be placed on only one spin-helical set forming on one edge. A small gap in the superconducting ring forms a Josephson junction that is being mediated by the spin-helical topological edge states. By threading a magnetic flux through the superconducting ring, the phase difference across this junction can be tuned. Inside of the junction two Andreev bound states will form due to consecutive Andreev reflections at energies below the superconducting gap, which feature a 4π periodic energy phase relation. When a magnetic field is applied inside of the Josephson junction (inside of the small gap), these Andreev bound states localize at the two boundaries to the superconductor. Otherwise they are entirely delocalized inside of the junction. When tuning the threaded magnetic flux such that the phase difference across the junction is equal to π, the Andreev bound states lie at zero energy and form two Majorana bound states.

Experiments trying to demonstrate the existence of Majorana excitations inside of the junction have thus far focused on the 4π periodicity of the energy phase and current phase relations [45–49]. For instance, Wiedenmann *et al.* implemented a similar system by depositing two superconducting niobium contacts on top of mercury telluride (HgTe) quantum wells [46]. These quantum wells are quantum spin Hall insulators featuring spin-helical topological edge states [50] so that this setup forms a Josephson junction similar to the one proposed by Fu and Kane. By driving the junction with an alternating current, Shapiro steps form in the current voltage characteristic of the junction [51]. In 4π periodic junctions odd Shapiro steps are predicted to vanish, an effect which could be observed in the experiment. In a similar

experiment performed by the same group Josephson radiation emitted by the junction also shows a 4π periodicity consistent with theoretical predictions [48].

1.5 Structure of this Thesis

In this introductory chapter we have seen how quantum computation can potentially have huge impacts on physics but also on the general public. We have seen how nonabelian anyons can help solve the problem of errors during quantum computations and have discussed a blueprint of how qubits and quantum gates through braiding can be achieved using Majorana excitations. We have also given a brief overview over current proposals and experimental setups hosting such Majorana excitations.

Having seen the broader context this thesis exists in, we turn our attention to this thesis, where we will follow the second approach described in the last section, i.e. Josephson junctions mediated by spin-helical topological edge states of quantum spin Hall insulators sometimes called fractional Josephson junctions. The general goal pursued in this thesis is to find new ways to characterize these junctions and experimental signatures of Majorana excitations forming in these junctions. We will start with a review of the Kane-Mele model in Chap. 2. This model features a quantum spin Hall insulating phase hosting spin-helical topological edge states at the sample edges and will be used as a basis for fractional junctions throughout this thesis. We then turn our attention to the first proposed setup in Chap. 3 in which we look at fractional Josephson junctions in silicene. Due to the electric tunability of silicene, the fractional nature of the junctions can be probed using electric fields. Using this tunability, fermion parity breaking effects can be studied without having

to fabricate multiple samples, potentially adding another experimental signature of Majorana excitations forming in such junctions. The results discussed in Chap. 3 have been published in [52] and [53]. In Chap. 4 we study the effects that quasiparticle poisoning, i.e. effects that break fermion parity conservation inside of the junction, has on the dynamics of fractional junctions. These effects are important for the stability of qubits built out of Majorana excitations as well as understanding the experimental signatures of Majorana excitations in fractional junctions. We propose experimental schemes by which the rates of these quasiparticle poisoning effects can be measured via a voltage measurement as well as study the effects that thermal noise has on the setup. This chapter is based on [54]. In order to be able to perform some of the measurements that we propose, it is necessary that the Josephson junctions lie in the long junction regime, i.e. that the distance between the two superconductors is large compared to the superconducting coherence length. In Chap. 5 we address this limitation by proposing a junction in which the edge states mediating the Josephson effect are coupled to additional states. By doing so, the resulting junction effectively behaves like a junction that is longer than the junction physically is. With this scheme some of the proposed experiments can potentially be achieved even in smaller junctions. We summarize the results of this thesis as well as give a short overview of further unanswered questions and possible research in this field in Chap. 6.

2

Kane-Mele Model

One of the goals of this thesis is to analyze possible manipulations of fractional Josephson junctions. Such junctions can be made by bringing a typical s-wave superconductor in close proximity to the spin-helical edge states of a quantum spin Hall insulator [25]. Kane and Mele proposed graphene as a possible candidate for such a quantum spin Hall insulator [55] and devised a model describing the low energy electronic states in graphene. However, the size of the gap turning the bulk of graphene into an insulator has been reevaluated since the original publication by Kane and Mele and at around $\sim 1\,\mu$eV is much smaller than initially thought. In experiments it should therefore only be ac-

cessible at temperatures below ~ 10 mK [56]. Nonetheless, there exist structures similar to graphene like silicene, germanene, and stanene which are, like graphene, 2D sheets of atoms arranged in a honeycomb lattice albeit with silicon, germanium, and tin atoms. These systems are also described by the same model as graphene but also feature a much larger bulk energy gap so that the quantum spin Hall insulating phase should be accessible at much higher temperatures [57]. Therefore, should an explicit model for a quantum spin Hall insulator be needed in this thesis, we will revert to the model described by Kane and Mele in [55], often referred to as the "*Kane-Mele model*".

In this introductory chapter we will give a short overview over the Kane-Mele model. We will first start from a tight binding description of electronic states in graphene and approximate this model around zero energy in Sec. 2.1. After also including spin-orbit interaction we will give a brief overview of the energy spectrum of this model. Following this discussion we will also include superconductivity into the model as will be necessary for the description of Josephson junctions in the following chapters. To make numerical treatments possible, we will also discretize the continuum model on a square lattice in Sec. 2.2 followed by a short summary over the three different versions of the Kane-Mele model used in this thesis in Sec. 2.3.

2.1 Low Energy Continuum Model

In their seminal paper [55] Kane and Mele proposed a model describing electronic states of graphene near the Fermi energy. They furthermore demonstrated that this model describes a time reversal symmetric quantum spin Hall insulator including two spin-helical edge states. Because this not only describes the elec-

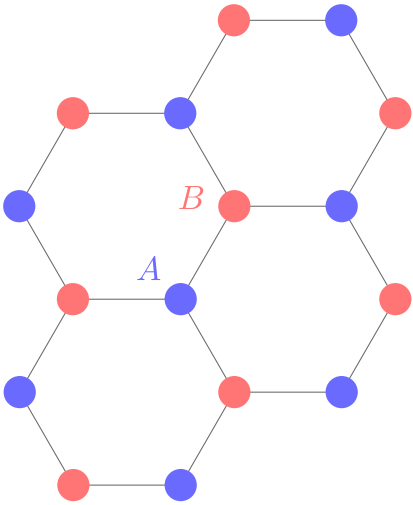

Figure 2.1: Lattice of graphene. Carbon atoms are arranged in a hexagonal lattice with two sublattices A (blue) and B (red) forming a honeycomb lattice.

tronic properties of graphene, but also similar compounds like silicene and stanene [57], it is often used as an implementation of a quantum spin Hall insulator.

2.1.1 Low Energy Approximation

The above-mentioned model can be deduced by starting from a tight binding description and approximating it around the chemical potential [58, 59]. Graphene is made up of carbon atoms arranged in a hexagonal lattice containing two sublattices A and B sometimes called a honeycomb lattice (Fig. 2.1). Considering

nearest neighbor hopping, the tight binding Hamiltonian reads

$$H = \sum_{is} \epsilon_{is} c_{is}^\dagger c_{is} - t \sum_{\langle i,j \rangle s} c_{is}^\dagger c_{js} \tag{2.1}$$

where c_{is} annihilates an electron at site i in spin polarization s and ϵ_{is} is the onsite energy. The second sum runs over nearest neighbors i, j and facilitates the electron hopping of strength t.

Since this model is translationally invariant, it can be diagonalized by Fourier transformation

$$H = \sum_{\boldsymbol{q}s} \epsilon_A c_{A\boldsymbol{q}s}^\dagger c_{A\boldsymbol{q}s} + \epsilon_B c_{B\boldsymbol{q}s}^\dagger c_{B\boldsymbol{q}s} - f(\boldsymbol{q}) c_{A\boldsymbol{q}s}^\dagger c_{B\boldsymbol{q}s} + \text{H.c.} \tag{2.2}$$

with

$$f(\boldsymbol{q}) = t \sum_{\boldsymbol{\delta}} e^{i\boldsymbol{q}\cdot\boldsymbol{\delta}} \tag{2.3}$$

where $\boldsymbol{\delta}$ are the vectors connecting nearest neighbors and $c_{\sigma\boldsymbol{q}s}$ annihilates an electron in sublattice σ, at momentum $\boldsymbol{q}$, and in spin polarization s.

From the resulting spectrum

$$\epsilon_{\boldsymbol{q}} = \mu \pm \sqrt{|f(\boldsymbol{q})|^2 + m^2}, \qquad \begin{cases} \mu = \dfrac{\epsilon_A + \epsilon_B}{2} \\ m = \dfrac{\epsilon_A - \epsilon_B}{2} \end{cases} \tag{2.4}$$

one can see that the low energy states lie around the corners of the Brillouin zone. Of these corners only two are independent of each other (i.e. are not simply separated by reciprocal lattice vectors) and are commonly called the Dirac points or Dirac valleys K and K'. These points are time reversal partners (up to a reciprocal lattice vector) and lie at opposite corners of the Brillouin zone [59].

Approximating $f(\boldsymbol{q})$ around these two points and absorbing a phase in a gauge transformation, we arrive at the low energy

Hamiltonian

$$H \approx \sum_{\boldsymbol{k}} \psi^\dagger_{\boldsymbol{k}} \mathcal{H}_{\boldsymbol{k}} \psi_{\boldsymbol{k}}, \qquad \mathcal{H}_{\boldsymbol{k}} = \mu + \hbar v_F(\tau_z \sigma_x k_x + \sigma_y k_y) + m\sigma_z \tag{2.5}$$

with

$$\psi_{\boldsymbol{k}} = (\psi_{\boldsymbol{k}\uparrow}, \psi_{\boldsymbol{k}\downarrow})^T, \qquad \psi_{\boldsymbol{k}s} = (c_{AK\boldsymbol{k}s}, c_{BK\boldsymbol{k}s}, c_{AK'\boldsymbol{k}s}, c_{BK'\boldsymbol{k}s})^T \tag{2.6}$$

where $c_{\sigma\tau\boldsymbol{k}s}$ annihilates an electron on sublattice $\sigma = A, B$ around the $\tau = K, K'$ point in spin polarization $s = \uparrow, \downarrow$ and the momentum is measured as an offset to either K or K'

$$\boldsymbol{q} = \boldsymbol{K}^{(\prime)} + \boldsymbol{k}. \tag{2.7}$$

The σ_i and τ_i are Pauli matrices acting in the sublattice (A, B) and valley (K, K') subspace respectively. The Fermi velocity $v_F = 3ta/(2\hbar)$ is determined by the hopping constant t and the lattice spacing a and is approximately $v_F \approx 10^6$ m/s [57, 58].

This model can also be expressed in real space by Fourier transformation

$$\begin{aligned} H &= \int d\boldsymbol{x}\, \psi^\dagger(\boldsymbol{x}) \mathcal{H}(\boldsymbol{x}) \psi(\boldsymbol{x}), \\ \mathcal{H}(\boldsymbol{x}) &= \mu - i\hbar v_F(\tau_z \sigma_x \partial_x + \sigma_y \partial_y) + m\sigma_z \end{aligned} \tag{2.8}$$

where $\psi(\boldsymbol{x})$ is connected to $\psi_{\boldsymbol{k}}$ by a Fourier transformation.

In the case of vanishing chemical potential μ and mass term m, the Hamiltonian features a gapless linear spectrum $E_{\boldsymbol{k}} = \pm\hbar v_F |\boldsymbol{k}|$ around the two Dirac points often called Dirac cones due to their shape. As the Hamiltonian (2.8) does not contain spin-dependent contributions, the resulting Dirac cones are spin-degenerate. While a finite chemical potential μ only shifts these cones to higher or lower energies, a finite mass term m opens a gap of $2m$ in the spectrum around the chemical potential. Clean sheets of graphene are inversion symmetric and should have both

vanishing chemical potential and mass term [58–60]. However, such terms can be induced by explicitly breaking this symmetry, for instance, by growing graphene on specific substrates [60, 61] or by applying a perpendicular electric field to silicene, another 2D system described by the Kane-Mele model [62–64].

2.1.2 Spin-Orbit Interaction

The description up to now assumes electrons of different spins to be independent of each other. However, spin-orbit coupling can generally be present and takes the form [55]

$$\mathcal{H}_{SO} = -\Delta_{SO} s_z \tau_z \sigma_z \tag{2.9}$$

where s_i are Pauli matrices acting in the spin $(\uparrow, \downarrow)$ subspace[1]. This term respects both the inversion symmetry as well as the time reversal symmetry of intrinsic graphene and hence can be generally present.

Adding this term to the Hamiltonian (2.8)

$$\begin{aligned} H &= \int d\boldsymbol{x}\, \psi^\dagger(\boldsymbol{x}) \mathcal{H}(\boldsymbol{x}) \psi(\boldsymbol{x}), \\ \mathcal{H}(\boldsymbol{x}) &= \mu - i\hbar v_F(\tau_z \sigma_x \partial_x + \sigma_y \partial_y) + m\sigma_z - \Delta_{SO} s_z \tau_z \sigma_z \end{aligned} \tag{2.10}$$

describes electrons in graphene around the Fermi energy and is often referred to as the "*Kane-Mele model*", named after its pioneers[2].

Including the spin-orbit coupling turns the previously gapless Dirac cones (in the case of vanishing mass term m) into gaped Dirac cones

$$E_{\boldsymbol{k}} = \mu \pm \sqrt{(\hbar v_F \boldsymbol{k})^2 + (m - \xi\eta\Delta_{SO})^2} \tag{2.11}$$

[1] We chose a sign convention so that $\Delta_{SO} > 0$.

[2] The original paper by Kane and Mele also described a mirror symmetry breaking Rashba term. Such a term can result from perpendicular electric fields or specific substrates.

where $\xi = 1(-1)$ in the case of spin up (down) polarized electrons and $\eta = 1(-1)$ for electrons around the $K(K')$ Dirac point. For vanishing (or small, see Chap. 3) mass term m the system is in a quantum spin Hall insulating state which is a topologically nontrivial state [55, 63–65]. This means that in finite systems spin-helical edge states localized at the sample edge emerge. Their propagation direction is locked to the electron spin so that at a single edge only spin up polarized electrons can propagate, for instance, to the left while spin down polarized electrons can only propagate to the right. The situation is reversed at the opposite sample edge. These states are topologically protected in the sense that because the states at a single edge are time reversal partners, any local perturbation preserving time reversal symmetry cannot couple these states so that elastic backscattering is forbidden. Backscattering will still be possible however if the scattering is inelastic [35, 55, 66–69] or occurs between the two edges, e.g. if the distance between the two edges is small enough to allow for a finite overlap between the states localized at opposite sample edges [70, 71].

Recent considerations on the strength of the spin-orbit coupling in graphene have predicted the gap opened by it to be on the scale of $\sim 1\,\mu$eV and is generally considered to be difficult to observe in an experiment [56]. However, similar structures, like silicene, are predicted to also be described by the Kane-Mele model around the Fermi energy, albeit with a much larger spin-orbit coupling of ~ 3.9 meV [57].

2.1.3 Superconductivity

Kane and Mele did not consider superconductivity in their original proposal of their model. However, because we will use their model as the basis to form fractional Josephson junctions throughout this thesis, it will be helpful to already include it at

this point.

To include superconductivity into the Kane-Mele model we change the basis to the Nambu basis

$$\begin{aligned}\psi(\boldsymbol{x}) &= (\psi_\uparrow(\boldsymbol{x}), \psi_\downarrow(\boldsymbol{x}), \bar{\psi}^\dagger_\downarrow(\boldsymbol{x}), -\bar{\psi}^\dagger_\uparrow(\boldsymbol{x}))^T \\ \psi_s(\boldsymbol{x}) &= (c_{AKs}(\boldsymbol{x}), c_{BKs}(\boldsymbol{x}), c_{AK's}(\boldsymbol{x}), c_{BK's}(\boldsymbol{x}))^T \\ \bar{\psi}_s(\boldsymbol{x}) &= (c_{AK's}(\boldsymbol{x}), c_{BK's}(\boldsymbol{x}), c_{AKs}(\boldsymbol{x}), c_{BKs}(\boldsymbol{x}))^T.\end{aligned} \tag{2.12}$$

In this basis the Kane-Mele model without superconductivity reads

$$\begin{aligned}H &= \frac{1}{2}\int d\boldsymbol{x}\, \psi^\dagger(\boldsymbol{x})\mathcal{H}(\boldsymbol{x})\psi(\boldsymbol{x}), \\ \mathcal{H}(\boldsymbol{x}) &= \mu\rho_z - i\hbar v_F(\rho_z\tau_z\sigma_x\partial_x + \rho_z\sigma_y\partial_y) + m\rho_z\sigma_z - \Delta_{SO}\rho_z s_z\tau_z\sigma_z\end{aligned} \tag{2.13}$$

where ρ_i are Pauli matrices acting in the particle hole subspace[3]. The reason for this change of basis is that in this basis superconducting terms take the simple form

$$\Delta(\cos(\phi)\rho_x + \sin(\phi)\rho_y) \tag{2.14}$$

where Δ and ϕ are the superconducting gap and phase respectively. Adding this term to eq. (2.13) yields the Kane-Mele model including superconductivity

$$\begin{aligned}H &= \frac{1}{2}\int d\boldsymbol{x}\, \psi^\dagger(\boldsymbol{x})\mathcal{H}(\boldsymbol{x})\psi(\boldsymbol{x}), \\ \mathcal{H}(\boldsymbol{x}) &= \mu\rho_z - i\hbar v_F(\rho_z\tau_z\sigma_x\partial_x + \rho_z\sigma_y\partial_y) + m\rho_z\sigma_z - \Delta_{SO}\rho_z s_z\tau_z\sigma_z \\ &\quad + \Delta(\cos(\phi)\rho_x + \sin(\phi)\rho_y).\end{aligned} \tag{2.15}$$

In general, the superconducting gap $\Delta \equiv \Delta(\boldsymbol{x})$ and phase $\phi \equiv \phi(\boldsymbol{x})$ can be dependent on the position $\boldsymbol{x}$. To form Josephson junctions we will assume throughout this thesis that both the

[3] We have neglected a constant in $\mathcal{H}(\boldsymbol{x})$.

superconducting gap Δ and phase ϕ will change sharply, i.e. with a drop, instead of smoothly across boundaries of different regions and be constant inside of these regions. Such superconducting terms can for instance be induced by the proximity effect, i.e. where the system described by the Kane-Mele model is brought into close proximity to an s-wave superconductor [25].

2.2 Discretization of Continuum Model

The low energy continuum model described in Sec. 2.1 can be solved analytically only for simple topologies of parameters. For more complicated spatially varying mass parameters, for instance, this model will need to be solved numerically. This can be achieved by discretizing the continuous space to a lattice. In general, any 2D lattice can be chosen to discretize this space. In the following we chose the square lattice for its simplicity.

The discretization can be performed by Fourier transforming the low energy model from momentum space to the discretized real space[4]. On the square lattice symmetric nearest neighbor hopping terms of the form $c_i^\dagger c_j + c_j^\dagger c_i$ where the sites i and j are nearest neighbors Fourier transform to terms proportional to $\cos(k_{x,y}b)$ in momentum space depending on whether the hopping is in the $x-$ or the $y-$direction. Here b is the lattice spacing of the square lattice. Similarly anti-symmetric hopping of the form $i(c_i^\dagger c_j - c_j^\dagger c_i)$ where i and j are again nearest neighbors Fourier transform to terms proportional to $\sin(k_{x,y}b)$ in momentum space. Furthermore, higher order hopping terms where i and j are not nearest neighbors transform to higher orders of

[4] This method is equivalent to starting from the continuum model in real space (2.10) and approximating the derivatives $\partial_{x,y}$ with their central finite differences.

sine and cosine functions ($\sin(nk_{x,y}b)$ or $\cos(nk_{x,y}b)$ with n being an integer).

Therefore, it is helpful to first approximate the individual terms contained in the low energy continuum model

$$\begin{aligned} H &= \sum_{\boldsymbol{k}} \psi^\dagger_{\boldsymbol{k}} \mathcal{H}_{\boldsymbol{k}} \psi_{\boldsymbol{k}}, \\ \mathcal{H}_{\boldsymbol{k}} &= \mu\rho_z + \hbar v_F(\rho_z\tau_z\sigma_x k_x + \rho_z\sigma_y k_y) + m\rho_z\sigma_z - \Delta_{SO}\rho_z s_z \tau_z \sigma_z \\ &\quad + \Delta(\cos(\phi)\rho_x + \sin(\phi)\rho_y). \end{aligned} \tag{2.16}$$

Here the only $\boldsymbol{k}$-dependent terms are linear in the momenta $k_{x,y}$. For this term we can use the approximation

$$k_{x,y} = \frac{1}{b} k_{x,y} b \approx \frac{1}{b} \sin(k_{x,y} b) \tag{2.17}$$

where b is the lattice constant of the square lattice used to discretize the continuum model. This approximation is good for small arguments $k_{x,y}b$, i.e. momenta small compared to b^{-1}.

Substituting this approximation into the low energy continuum model (2.16), we can now perform the Fourier transformation

$$\psi_{\boldsymbol{k}} = \frac{1}{\sqrt{N}} \sum_{\boldsymbol{R}} e^{-i\boldsymbol{k}\boldsymbol{R}} \psi_{\boldsymbol{R}} \tag{2.18}$$

where the sum runs over all lattice site positions $\boldsymbol{R}$ of the square lattice and N is the number of lattice sites. Performing the

Fourier transformation for the kinetic term yields

$$\begin{aligned}
&\sum_{\boldsymbol{k}} \psi^\dagger_{\boldsymbol{k}} \hbar v_F (\rho_z \tau_z \sigma_x k_x + \rho_z \sigma_y k_y) \psi_{\boldsymbol{k}} \\
&\quad \approx \frac{\hbar v_F}{b} \left(\sum_{\boldsymbol{k}} \psi^\dagger_{\boldsymbol{k}} \sin(k_x b) \rho_z \tau_z \sigma_x \psi_{\boldsymbol{k}} + \sum_{\boldsymbol{k}} \psi^\dagger_{\boldsymbol{k}} \sin(k_y b) \rho_z \sigma_y \psi_{\boldsymbol{k}} \right) \\
&\quad = -i \frac{\hbar v_F}{2b} \left(\sum_{\boldsymbol{R}} \psi^\dagger_{\boldsymbol{R}+\boldsymbol{\delta}_1^s} \rho_z \tau_z \sigma_x \psi_{\boldsymbol{R}} + \sum_{\boldsymbol{R}} \psi^\dagger_{\boldsymbol{R}+\boldsymbol{\delta}_2^s} \rho_z \sigma_y \psi_{\boldsymbol{R}} \right) + \text{H.c.} \\
&\quad = -i \frac{\hbar v_F}{2b} \sum_{\boldsymbol{R}} \left(\psi^\dagger_{\boldsymbol{R}+\boldsymbol{\delta}_1^s} \rho_z \tau_z \sigma_x \psi_{\boldsymbol{R}} + \psi^\dagger_{\boldsymbol{R}+\boldsymbol{\delta}_2^s} \rho_z \sigma_y \psi_{\boldsymbol{R}} \right) + \text{H.c.}
\end{aligned} \tag{2.19}$$

where

$$\boldsymbol{\delta}_1^s = \begin{pmatrix} b \\ 0 \end{pmatrix}, \qquad \boldsymbol{\delta}_2^s = \begin{pmatrix} 0 \\ b \end{pmatrix} \tag{2.20}$$

are the Bravais lattice vectors of the square lattice and H.c. denotes the hermitian conjugate.

Solving this discretized Hamiltonian on a square lattice for vanishing chemical potential, mass parameter and spin-orbit interaction $\mu = m = \Delta_{SO} = 0$ yields the energy spectrum

$$\epsilon_{\boldsymbol{k}} = \pm \frac{\hbar v_F}{b} \sqrt{\sin^2(k_x b) + \sin^2(k_y b)} \tag{2.21}$$

which for momenta $\boldsymbol{k}$ close to the Γ point is linear in $|\boldsymbol{k}|$ and forms a Dirac cone like in the continuum model. For large momenta however the spectrum starts to deviate from the continuum model and adds three additional spurious Dirac cones at the corners of the Brillouin zone, an effect known from particle physics as the fermion doubling problem [72–74]. Since we are interested in the topology of our systems, which is intimately linked to the number of gap openings and closings, these additional spurious Dirac cones pose a problem. To rectify this problem, we will need to add an additional term to the Hamiltonian, which

gaps these spurious Dirac cones, but leaves the Dirac cone at the Γ point intact. Furthermore, the added term should also respect all symmetries of the Kane-Mele model, i.e. time reversal symmetry. A term that fulfills all these conditions is given by [59, 75]

$$\frac{\hbar v_F}{b}\left(\frac{1}{2}(k_x b)^2+\frac{1}{2}(k_y b)^2\right)\sigma_z \approx \frac{\hbar v_F}{b}\left(2-\cos(k_x b)-\cos(k_y b)\right)\sigma_z \tag{2.22}$$

which has the form of a mass term[5].

Including this term the resulting spectrum

$$\epsilon_{\boldsymbol{k}} = \pm\frac{\hbar v_F}{b}\sqrt{\sin^2(k_x b)+\sin^2(k_y b)+\left(2-\cos(k_x b)-\cos(k_y b)\right)^2} \tag{2.23}$$

again for vanishing chemical potential, mass parameter and spin-orbit interaction $\mu = m = \Delta_{SO} = 0$ is still linear in $|\boldsymbol{k}|$ to lowest order in $\boldsymbol{k}$ around the Γ point and forms a Dirac cone. However, the spurious Dirac cones at the corner of the Brillouin zone are now gaped due to the added term (2.22). It is important to note that these spurious Dirac cones close again at finite mass parameters

$$m = -2\frac{\hbar v_F}{b}, \qquad m = -4\frac{\hbar v_F}{b} \tag{2.24}$$

despite the continuum model having no zero energy states. Furthermore, the spectrum is nondispersive if

$$m = -\frac{\hbar v_F}{b}. \tag{2.25}$$

In practice these two problems can be avoided by only applying mass parameters

$$m > -\frac{\hbar v_F}{b}, \tag{2.26}$$

[5] This is not the only possible term fulfilling these conditions.

which does not put a real constraint on the system due to the fact that one can simply choose a smaller lattice spacing b in order to reach smaller mass parameters.

Fourier transforming the added term (2.22) yields

$$\begin{aligned}
&\sum_{\boldsymbol{k}} \psi^\dagger_{\boldsymbol{k}} \frac{\hbar v_F}{b} \left(2 - \cos(k_x b) - \cos(k_y b)\right) \rho_z \sigma_z \psi_{\boldsymbol{k}} \\
&= \sum_{\boldsymbol{R}} \frac{2\hbar v_F}{b} \psi^\dagger_{\boldsymbol{R}} \rho_z \sigma_z \psi_{\boldsymbol{R}} - \frac{\hbar v_F}{2b} \Big(\psi^\dagger_{\boldsymbol{R}+\boldsymbol{\delta}_1} \rho_z \sigma_z \psi_{\boldsymbol{R}} + \psi^\dagger_{\boldsymbol{R}+\boldsymbol{\delta}_2} \rho_z \sigma_z \psi_{\boldsymbol{R}} \\
&\qquad\qquad + \text{H.c.} \Big) \\
&= \frac{2\hbar v_F}{b} \sum_{\boldsymbol{R}} \psi^\dagger_{\boldsymbol{R}} \rho_z \sigma_z \psi_{\boldsymbol{R}} - \frac{\hbar v_F}{2b} \sum_{\boldsymbol{R}} \sum_{i=1}^{2} \left(\psi^\dagger_{\boldsymbol{R}+\boldsymbol{\delta}_i} \rho_z \sigma_z \psi_{\boldsymbol{R}} + \text{H.c.} \right).
\end{aligned} \tag{2.27}$$

Combining all the individual parts, we find the discretized low energy model to read

$$\begin{aligned}
H = &\sum_{\boldsymbol{R}} \psi^\dagger_{\boldsymbol{R}} \epsilon \psi_{\boldsymbol{R}} - t_s \sum_{\langle \boldsymbol{R}, \boldsymbol{R}' \rangle} \psi^\dagger_{\boldsymbol{R}} \rho_z \sigma_z \psi_{\boldsymbol{R}'} \\
&- i t_s \sum_{\langle \boldsymbol{R}, \boldsymbol{R}' \rangle_x} \nu_{\boldsymbol{R}\boldsymbol{R}'} \psi^\dagger_{\boldsymbol{R}} \rho_z \tau_z \sigma_x \psi_{\boldsymbol{R}'} - i t_s \sum_{\langle \boldsymbol{R}, \boldsymbol{R}' \rangle_y} \nu_{\boldsymbol{R}\boldsymbol{R}'} \psi^\dagger_{\boldsymbol{R}} \rho_z \sigma_y \psi_{\boldsymbol{R}'}
\end{aligned} \tag{2.28}$$

with

$$\begin{aligned}
\epsilon &= \mu \rho_z + (m + 4t_s) \rho_z \sigma_z - \Delta_{SO} \rho_z s_z \tau_z \sigma_z \\
&\qquad + \Delta(\cos(\phi) \rho_x + \sin(\phi) \rho_y) \\
t_s &= \frac{\hbar v_F}{2b}
\end{aligned} \tag{2.29}$$

and where $\nu_{\boldsymbol{R}\boldsymbol{R}'} = \pm 1$ is a set of signs so that $\nu_{\boldsymbol{R}\boldsymbol{R}'} = 1$ if the lattice site $\boldsymbol{R}$ is to the right or top of the lattice site $\boldsymbol{R}'$ and $\nu_{\boldsymbol{R}\boldsymbol{R}'} = -1$ otherwise. The sum over $\langle \boldsymbol{R}, \boldsymbol{R}' \rangle$ runs over all nearest neighbors while the sums $\langle \boldsymbol{R}, \boldsymbol{R}' \rangle_x$ and $\langle \boldsymbol{R}, \boldsymbol{R}' \rangle_y$ run only over nearest neighbors in the $x-$ and $y-$direction respectively.

2.3 Variations of the Kane-Mele Model

In this introductory chapter we have reviewed multiple versions of the Kane-Mele model, which due to their differences make them particularly suitable in different scenarios.

First, we have the low energy continuum model as originally introduced[6] in Ref. [55]

$$\begin{aligned} H &= \int d\boldsymbol{x}\, \psi^\dagger(\boldsymbol{x})\mathcal{H}(\boldsymbol{x})\psi(\boldsymbol{x}), \\ \mathcal{H}(\boldsymbol{x}) &= \mu\rho_z - i\hbar v_F(\rho_z\tau_z\sigma_x\partial_x + \rho_z\sigma_y\partial_y) + m\rho_z\sigma_z \\ &\quad - \Delta_{SO}\rho_z s_z\tau_z\sigma_z + \Delta(\cos(\phi)\rho_x + \sin(\phi)\rho_y) \end{aligned} \tag{2.30}$$

with the basis

$$\begin{aligned} \psi(\boldsymbol{x}) &= (\psi_\uparrow(\boldsymbol{x}), \psi_\downarrow(\boldsymbol{x}), \bar{\psi}^\dagger_\downarrow(\boldsymbol{x}), -\bar{\psi}^\dagger_\uparrow(\boldsymbol{x}))^T \\ \psi_s(\boldsymbol{x}) &= (c_{AKs}(\boldsymbol{x}), c_{BKs}(\boldsymbol{x}), c_{AK's}(\boldsymbol{x}), c_{BK's}(\boldsymbol{x}))^T \\ \bar{\psi}_s(\boldsymbol{x}) &= (c_{AK's}(\boldsymbol{x}), c_{BK's}(\boldsymbol{x}), c_{AKs}(\boldsymbol{x}), c_{BKs}(\boldsymbol{x}))^T \end{aligned} \tag{2.31}$$

where $c_{\sigma\tau s}(\boldsymbol{x})$ annihilates an electron in sublattice σ, valley τ, spin polarization s, and at position $\boldsymbol{x}$.

This version is best suited for analytical treatments as analytical solutions can be found for simple forms of the mass parameter m, which can in general depend on the position $m(\boldsymbol{x})$. For a constant mass parameter it features two twofold degenerate Dirac cones at the Γ point with gaps $2\,|m \pm \Delta_{SO}|$. Should the gap close due to changing mass parameter m, the system undergoes a topological phase transition and changes its topology [63–65] (see also Chap. 3).

[6] The model in the original paper [55] did not include a chemical potential μ, superconductivity, or a mass parameter m. However, especially the mass parameter will become important in later implementations of this model.

If the mass parameter m has a more complicated dependence on the position $\boldsymbol{x}$, the continuum model (2.30) can no longer be solved analytically. However, solutions can still be obtained numerically if we discretize this model. We have done this in Sec. 2.2 for a square lattice and obtained the second variation of the Kane-Mele model in form of the discretized Hamiltonian

$$\begin{aligned} H =& \sum_{\boldsymbol{R}} \psi^\dagger_{\boldsymbol{R}} \epsilon \psi_{\boldsymbol{R}} - t_s \sum_{\langle \boldsymbol{R}, \boldsymbol{R}' \rangle} \psi^\dagger_{\boldsymbol{R}} \rho_z \sigma_z \psi_{\boldsymbol{R}'} \\ & - it_s \sum_{\langle \boldsymbol{R}, \boldsymbol{R}' \rangle_x} \nu_{\boldsymbol{R}\boldsymbol{R}'} \psi^\dagger_{\boldsymbol{R}} \rho_z \tau_z \sigma_x \psi_{\boldsymbol{R}'} - it_s \sum_{\langle \boldsymbol{R}, \boldsymbol{R}' \rangle_y} \nu_{\boldsymbol{R}\boldsymbol{R}'} \psi^\dagger_{\boldsymbol{R}} \rho_z \sigma_y \psi_{\boldsymbol{R}'} \end{aligned} \tag{2.32}$$

with

$$\begin{aligned} \epsilon =& \mu \rho_z + (m + 4t_s) \rho_z \sigma_z - \Delta_{SO} \rho_z s_z \tau_z \sigma_z \\ & + \Delta(\cos(\phi) \rho_x + \sin(\phi) \rho_y), \\ t_s =& \frac{\hbar v_F}{2b} \end{aligned} \tag{2.33}$$

where the basis $\psi_{\boldsymbol{R}}$ is proportional to $\psi(\boldsymbol{R})$[7]. Like described in Sec. 2.2, $\nu_{\boldsymbol{R}\boldsymbol{R}'} = \pm 1$ is a set of signs defined so that $\nu_{\boldsymbol{R}\boldsymbol{R}'} = 1$ if the lattice site $\boldsymbol{R}$ is to the right or top of the lattice site $\boldsymbol{R}'$ and $\nu_{\boldsymbol{R}\boldsymbol{R}'} = -1$ otherwise. The sum over $\langle \boldsymbol{R}, \boldsymbol{R}' \rangle$ runs over all nearest neighbors and the sums over $\langle \boldsymbol{R}, \boldsymbol{R}' \rangle_x$ and $\langle \boldsymbol{R}, \boldsymbol{R}' \rangle_y$ run only over nearest neighbors in the $x-$ and $y-$direction respectively.

This version of the Kane-Mele model is particularly well suited for numerical treatment in the case where a spatially dependent mass parameter m makes analytical solutions to the continuum model unfeasible. In the case of a constant mass parameter this model features the same Dirac cones as the continuum model around the Γ point, but deviates from the linear dispersion relation at higher momenta $|\boldsymbol{k}| \sim \pi/b$ as it only approximates the continuum model for small momenta.

[7] The factor combining $\psi_{\boldsymbol{R}}$ with $\psi(\boldsymbol{x})$ is determined by the definition of the discretized expectation value.

Finally, the third version of the Kane-Mele model is comprised of the tight binding model of graphene-like structures [55]

$$\begin{aligned} H = &\sum_{is\rho\rho'} \epsilon_{is} (\rho_z)_{\rho\rho'} c^\dagger_{is\rho} c_{is\rho'} - t \sum_{\langle i,j\rangle s\rho\rho'} (\rho_z)_{\rho\rho'} c^\dagger_{is\rho} c_{js\rho'} \\ &- i\frac{\Delta_{SO}}{3\sqrt{3}} \sum_{\langle\langle i,j\rangle\rangle ss'\rho\rho'} \nu_{ij} (\rho_z)_{\rho\rho'} (s_z)_{ss'} c^\dagger_{is\rho} c_{js'\rho'} \\ &+ \Delta\cos(\phi) \sum_{is\rho\rho'} (\rho_x)_{\rho\rho'} c^\dagger_{is\rho} c_{is\rho'} + \Delta\sin(\phi) \sum_{is\rho\rho'} (\rho_y)_{\rho\rho'} c^\dagger_{is\rho} c_{is\rho'} \end{aligned} \tag{2.34}$$

where $c_{is\rho}$ annihilates an electron (hole) at position i in spin polarization s when $\rho = e$ ($\rho = h$). The first sum runs over all lattice sites i of the honeycomb lattice implementing onsite energies[8]. The second sum runs over all nearest neighbors i and j so that i and j will always belong to different sublattices and implements the kinetic energy of electrons via nearest neighbor hopping. The third sum $\langle\langle i,j\rangle\rangle$ implements the spin-orbit coupling on a hexagonal lattice and runs over next nearest neighbors where the signs $\nu_{ij} = \pm 1$ are called Haldane phases and are defined like in Fig. 2.2. Furthermore, $(s_z)_{ss'}$ corresponds to the matrix element of the s_z Pauli matrix at position ss'. Similarly, $(\rho_i)_{\rho\rho'}$ corresponds to the matrix element of the ρ_i Pauli matrix at position $\rho\rho'$. The last two sums implement the superconductivity not present in the original model.

This third version of the Kane-Mele model is particularly well suited for numerical treatments in cases where specific microscopic edge configurations might be important. It describes graphene-like structures which are a possible physical implementation of the low energy continuum model (2.30). It features the full dispersion relation, which for low energies approximates to two Dirac cones at each of the independent corners K and K' of

[8] The original publication [55] by Kane and Mele does not include this term.

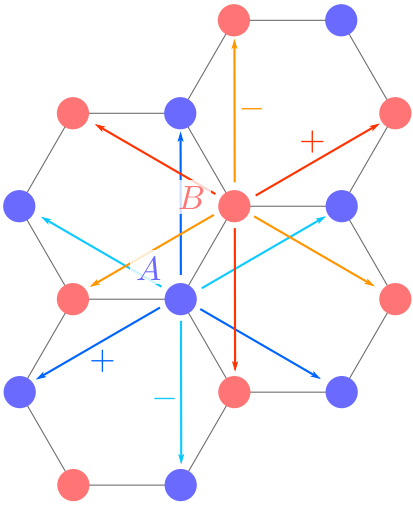

Figure 2.2: Haldane Phases ν_{ij} in graphene. Dark arrows correspond to $\nu_{ij} = 1$ whereas light arrows correspond to $\nu_{ij} = -1$.

the Brillouin zone, but deviates from this linear relationship for momenta further away from these points.

In the remainder of this thesis we will use the Kane-Mele model as a possible implementation of a quantum spin Hall insulator featuring spin-helical edge states. Where possible, analytical solutions will be based on the continuum model (2.30). Should we require numerical solutions to this model, we will, depending on the circumstances, revert to either the discretized low energy model (2.32), or the full tight binding model (2.34). In that case we will use the Kwant code to perform the numerical tight binding calculations [76] in conjunction with standard matrix diagonalization.

3

Josephson Junction in Silicene

With the preliminary description of frequently used models out of the way, we can focus on fractional Josephson junctions and possible detection schemes. Josephson junctions, when mediated by spin-helical topological edge states of quantum spin Hall insulators, feature a 4π periodic energy phase and current phase relation as opposed to the normal 2π periodicity [77], an effect known as the fractional Josephson effect. An important feature of such junctions is the existence of Majorana bound states [23,

25, 78, 79] as low energy excitations localized between the two superconductors should the phase difference across the junction be equal to π. Such excitations have been proposed as a possible building block for topological quantum computation [2, 80].

Despite the 4π periodicity being a striking signature of the fractional Josephson effect and hence the existence of Majorana bound states, experimental detection is complicated by the junction coupling to the external environment. Because the 4π periodicity is protected by fermion parity conservation inside the junction, parity breaking effects called quasiparticle poisoning [25, 81], where electrons can tunnel into or out of the junction, break this symmetry and reduce the periodicity back to 2π. Current experiments have therefore depended on ac properties of fractional junctions [45, 46, 48].

However, there has been a proposal by Beenakker *et al.* [78] to perform a critical current measurement, a dc measurement, in long junctions where the distance between the two superconductors l is large compared to the superconducting coherence length ξ_0. In such junctions the critical current is predicted to differ by a factor of 2 depending on whether the junction is topological featuring a 4π periodicity, or nontopological featuring a 2π periodicity. To support such an experiment, we propose a Josephson junction which can be tuned from the topological fractional state to the nontopological state by an external parameter. Using the electric tunability of the energy gap in silicene [57, 63–65, 82–87], we show that the topological edge states forming at mass domain walls can be tuned from spin-helical to spin-degenerate, which in turn changes a Josephson junction mediated by such edge states from topological to nontopological.

We start by introducing the proposed setup and the model we use to describe its electronic properties in Sec. 3.1. After that we turn our attention to the system neglecting the two superconductors forming the Josephson junction in Sec. 3.2 and analyze in detail edge states forming at mass domain walls in silicene. We

calculate spin- and valley-dependent Chern numbers and show how changing the electric fields applied perpendicular to the silicene sheet can tune these edge states between being spin-helical and spin-degenerate. We furthermore explicitly calculate the energy dispersion and wave function of the edge states. In Sec. 3.3 we then look at a Josephson junction mediated by the topological edge states. We show that Andreev bound states form inside the junction by directly calculating them analytically in the short junction limit ($l \ll \xi_0$) and numerically in the long junction limit ($l \gg \xi_0$). In addition we show how including intervalley scattering, which should generally be present, opens a gap in the energy phase relation of the Andreev bound states and reduces the periodicity of the junction from 4π to 2π, achieving the desired tunability. We propose a scenario where artificial tunable poisoning can be induced in a fractional Josephson junction in silicene by introducing a lead in Sec. 3.4. Finally, we summarize our findings in Sec. 3.5 and give a short overview of alternative materials in which such tunability might also be possible.

3.1 Model

The system is made up of a single sheet of silicene that is separated by the x-Axis into two regions (see Fig. 3.1). In these two regions electric fields $\boldsymbol{E}_1$ and $\boldsymbol{E}_2$ are applied perpendicular to the silicene sheet. Two superconductors with a phase difference of ϕ are placed on top of the sheet of silicene. Superconductivity is induced in the silicene sheet through the proximity effect [88] so that the system forms a Josephson junction [87, 89].

At low temperatures the system can be described by extending the Kane-Mele model (see Chap. 2) to include superconduct-

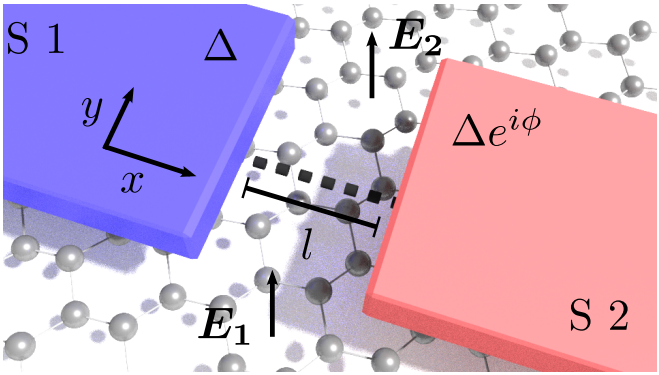

Figure 3.1: A single sheet of silicene is brought into close proximity to two superconductors forming a Josephson junction. The junction is facilitated by the edge states forming at the boundary between the two regions of different electric fields $\boldsymbol{E}_{1,2}$. Figure taken from the original publication [52]. ©2018 American Physical Society

ing terms

$$\begin{aligned} H &= \frac{1}{2}\int d\boldsymbol{x}\Psi^\dagger(\boldsymbol{x})\mathcal{H}(\boldsymbol{x})\Psi(\boldsymbol{x}), \\ \mathcal{H}(\boldsymbol{x}) &= \mathcal{H}_0 + \mathcal{H}_S + \mathcal{H}_I, \\ \mathcal{H}_0 &= -i\hbar v_F(\rho_z\tau_z\sigma_x\partial_x + \rho_z\sigma_y\partial_y) + m\rho_z\sigma_z - \Delta_{SO}\rho_z s_z\tau_z\sigma_z, \\ \mathcal{H}_S &= \Delta(\cos(\phi)\rho_x + \sin(\phi)\rho_y), \\ \mathcal{H}_I &= \delta\rho_z\tau_x \end{aligned} \tag{3.1}$$

where we use the Nambu basis

$$\begin{aligned} \Psi(\boldsymbol{x}) &= (\psi_\uparrow(\boldsymbol{x}), \psi_\downarrow(\boldsymbol{x}), \bar{\psi}^\dagger_\downarrow(\boldsymbol{x}), -\bar{\psi}^\dagger_\uparrow(\boldsymbol{x}))^T \\ \psi_s(\boldsymbol{x}) &= (c_{AKs}(\boldsymbol{x}), c_{BKs}(\boldsymbol{x}), c_{AK's}(\boldsymbol{x}), c_{BK's}(\boldsymbol{x}))^T \end{aligned} \tag{3.2}$$

and $\bar{\psi}_s(\boldsymbol{x})$ is obtained from $\psi_s(\boldsymbol{x})$ by the substitution $K \leftrightarrow K'$. The matrices σ_i, τ_i, s_i, and ρ_i are Pauli matrices acting in the

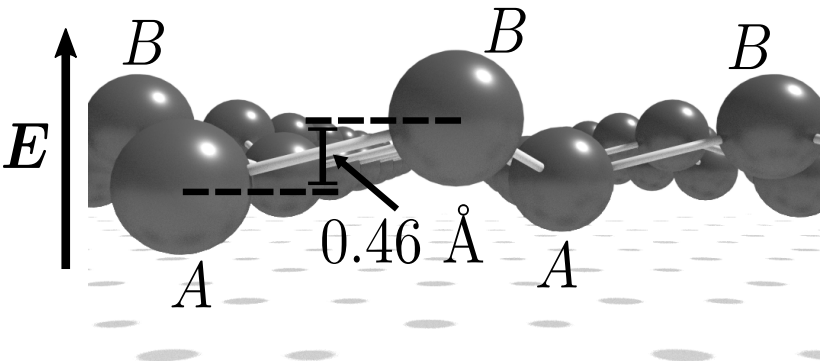

Figure 3.2: Side view of a sheet of silicene. The atoms of the A and B sublattice are offset in the z-direction by ± 0.23 Å. Due to the electric field $\boldsymbol{E}$, electrons will see different onsite energies for the two sublattices resulting in a mass term $m = 0.23 \text{ Å} \times E^z$.

sublattice (A, B), valley (K, K'), spin $(\uparrow, \downarrow)$, and particle hole subspace. The field operators $c_{\sigma\tau s}(\boldsymbol{x})$ annihilate an electron at position $\boldsymbol{x}$ in sublattice σ, valley τ, and spin polarization s.

The first part $\mathcal{H}_0$ of the Hamiltonian is made up a kinetic part, a mass term, and spin-orbit interaction and has been adapted from (2.30) to the Nambu basis as well as setting the chemical potential to zero. The Fermi velocity $v_F \approx 5.5 \times 10^5$ m/s and intrinsic spin-orbit interaction $\Delta_{SO} \approx 3.9$ meV in silicene [57, 63] are fixed and cannot be changed by external parameters. The mass parameter $m \approx 0.23 \text{ Å} \times E_i^z$ however results from the atoms in the two sublattices A and B not being in a perfect 2D plane, but rather being offset in the z-direction by ± 0.23 Å(see Fig. 3.2). The electric field E_i^z parallel to this offset results in electrons seeing different onsite energies for the two sublattices, which according to (2.4) results in a finite mass term. Because this mass parameter is proportional to the parallel electric field,

it can be tuned by an external parameter.

The second part $\mathcal{H}_S$ of the Hamiltonian describes the proximity induced superconductivity. The superconducting paring potential $\Delta e^{i\phi}$ is made up of the superconducting gap Δ and the superconducting phase ϕ, which can both depend on the position $\boldsymbol{x}$.

Finally, the third part $\mathcal{H}_I$ describes intervalley scattering. In clean silicene samples the two valleys should be independent of each other, like in the original Kane-Mele model (2.30). However, atomic scale disorder, which can in general be present, will induce scattering of strength δ between the two valleys. While this form of intervalley scattering is only one of six possible time reversal symmetric forms [90], only the presence of some kind of backscattering is important for the following discussion.

The Hamiltonian (3.1) can generally be diagonalized by

$$\begin{aligned} H &= \frac{1}{2}\sum_n \varepsilon_n \gamma_n^\dagger \gamma_n, \\ \gamma_n^\dagger &= \int d\boldsymbol{x} \Psi^\dagger(\boldsymbol{x}) \boldsymbol{\Lambda}_n(\boldsymbol{x}) \end{aligned} \tag{3.3}$$

where $\boldsymbol{\Lambda}_n$ is the 16-component eigenvector of $\mathcal{H}(\boldsymbol{x})$ with the eigenvalue ε_n. Due to the particle hole symmetry of the Hamiltonian (3.1), these eigenstates always come in pairs at $\pm\varepsilon_n$ with $\gamma_{\varepsilon_n} = \gamma_{-\varepsilon_n}^\dagger$.

3.2 Topological Edge States

To understand how the tunability of the proposed junction arises, we first focus on a simplified system $\mathcal{H}_0$ while neglecting the superconductivity $\mathcal{H}_S$ and intervalley scattering $\mathcal{H}_I$. Because $\mathcal{H}_0$ is symmetric in the spin and valley subspaces, we can treat

them as signs $\eta = \pm 1$ and $\xi = \pm 1$ where $\eta = 1(-1)$ for the $K(K')$ valley and $\xi = 1(-1)$ for spin up (down) polarized electrons. The simplified Hamiltonian now reads

$$\begin{aligned} H &= \int d\boldsymbol{x} \psi^\dagger(\boldsymbol{x}) h(\boldsymbol{x}) \psi(\boldsymbol{x}), \\ h(\boldsymbol{x}) &= -i\hbar v_F(\eta\sigma_x\partial_x + \sigma_y\partial_y) + (m - \xi\eta\Delta_{SO})\sigma_z \end{aligned} \tag{3.4}$$

in the basis

$$\psi(\boldsymbol{x}) = (c_{A\tau s}(\boldsymbol{x}), c_{B\tau s}(\boldsymbol{x}))^T. \tag{3.5}$$

In the case of a constant mass parameter (only one constant electric field) this Hamiltonian can be expressed in momentum space

$$\begin{aligned} H &= \sum_{\boldsymbol{k}} \psi^\dagger_{\boldsymbol{k}} h_{\boldsymbol{k}} \psi_{\boldsymbol{k}}, \\ h_{\boldsymbol{k}} &= \hbar v_F(\eta k_x\sigma_x + k_y\sigma_y) + (m - \xi\eta\Delta_{SO})\sigma_z \end{aligned} \tag{3.6}$$

now in the basis

$$\psi_{\boldsymbol{k}} = (c_{A\tau s\boldsymbol{k}}, c_{B\tau s\boldsymbol{k}})^T. \tag{3.7}$$

The eigenvalues of $h_{\boldsymbol{k}}$ read

$$\varepsilon_{\boldsymbol{k}} = \pm\sqrt{(\hbar v_F \boldsymbol{k})^2 + (m - \xi\eta\Delta_{SO})^2} \tag{3.8}$$

so that the spectrum $\varepsilon_{\boldsymbol{k}}$ features a gap of $2\,|m - \xi\eta\Delta_{SO}|$. In the case of spin up polarized electrons on the K valley ($\xi = \eta = 1$) tuning the mass parameter m from $m < \Delta_{SO}$ to $m > \Delta_{SO}$ tunes the system from a gapped spectrum for $m < \Delta_{SO}$ through a gapless spectrum for the critical mass $m_c = \Delta_{SO}$ to a spectrum that is again gapped for $m > \Delta_{SO}$. The critical mass m_c corresponds to the critical electric field $E_c = \Delta_{SO}/(0.23\ \text{Å}) \approx 17\ \text{meV/Å}$[62–64].

3.2.1 Chern Number

To see that this gap closing is accompanied by a topological phase transition, we can calculate the Chern number [59, 65]

$$n = \frac{1}{2\pi} \int d\boldsymbol{k} F_{xy}(\boldsymbol{k}) \tag{3.9}$$

where the Berry curvature $F_{xy}(\boldsymbol{k})$ is given by

$$\begin{aligned} F_{xy}(\boldsymbol{k}) &= \partial_{k_x}[A_y(\boldsymbol{k})] - \partial_{k_y}[A_x(\boldsymbol{k})], \\ A_i(\boldsymbol{k}) &= -i \sum_{\alpha \in \text{ filled bands}} \langle \alpha | \partial_{k_i} | \alpha \rangle \end{aligned} \tag{3.10}$$

where the sum runs over all filled bands $|\alpha\rangle$. In a two level system that can be expressed in the form

$$\sum_{ab} k_a A_{ab} \sigma_b + M \sigma_z \tag{3.11}$$

where both sums run over $a, b = x, y$ the Chern number is given by [59]

$$n = \frac{1}{2} \operatorname{sgn}(M) \operatorname{sgn}(\det(A)). \tag{3.12}$$

In our case we can parameterize the Hamiltonian $h_{\boldsymbol{k}}$ with

$$A = \hbar v_F \begin{pmatrix} \eta & 0 \\ 0 & 1 \end{pmatrix}, \qquad M = m - \xi \eta \Delta_{SO} \tag{3.13}$$

so that the valley- and spin-dependent Chern number is given by [65]

$$n_{\eta\xi} = \frac{\eta}{2} \operatorname{sgn}(m - \xi \eta \Delta_{SO}). \tag{3.14}$$

Here we can see that the gap closing and reopening described above are indeed accompanied by a topological phase transition. If this Chern number changes across a boundary for a given spin

and valley configuration, then a topological edge state[1] with this configuration will exist localized at this boundary due to the bulk boundary correspondence [91]. Because the Chern number (3.14) is proportional to η, the edge states will always come in spin-helical pairs in accordance with the time reversal symmetry of the system.

The total Chern number of the entire system

$$n = \sum_{\eta\xi} n_{\eta\xi} = \sum_{\eta\xi} \frac{\eta}{2} \operatorname{sgn}(m - \xi\eta\Delta_{SO}) = 0 \tag{3.15}$$

vanishes like we would expect for a time reversal symmetric system. However, the topological $\mathbb{Z}_2$ invariant

$$\begin{aligned} \nu &= \sum_{\eta} \frac{n_{\eta\uparrow} - n_{\eta\downarrow}}{2} \mod 2 \\ &= \frac{1}{4} \sum_{\eta} \eta[\operatorname{sgn}(m - \eta\Delta_{SO}) - \operatorname{sgn}(m + \eta\Delta_{SO})] \mod 2 \\ &= \frac{1}{2}[\operatorname{sgn}(m - \Delta_{SO}) - \operatorname{sgn}(m + \Delta_{SO})] \mod 2 \\ &= \begin{cases} 0, & |m| > \Delta_{SO} \\ 1, & |m| < \Delta_{SO} \end{cases} \end{aligned} \tag{3.16}$$

can be determined and distinguishes between the topologically trivial ($\nu = 0$) and topologically nontrivial ($\nu = 1$) regime. In the topologically nontrivial regime there exists a set of spin-helical topological edge states at the sample edge and the system is in the quantum spin Hall insulating phase. Tuning the mass term to $|m| > \Delta_{SO}$ (by applying an electric field stronger than E_c), the system gets tuned into a trivial phase with no topological edge states at the sample edge.

[1] The bulk boundary correspondence only assures there will, for instance, be one more right moving edge state than there will be left moving edge states.

In the case of a single mass parameter either a single set of spin-helical edge states can exist or no edge states at all will be present in the system. The situation becomes richer when we consider two different mass parameters m_1 and m_2 in two bordering regions like in Fig. 3.1. Now, depending on the configuration of the two mass parameters, three different scenarios can occur (see Fig. 3.3).

In the first case (Fig. 3.3, blue) both mass parameters are either smaller than the critical mass $|m_{1,2}| < m_c$, or both mass parameters are larger than the critical mass $|m_{1,2}| > m_c$ with equal signs $\mathrm{sgn}(m_1) = \mathrm{sgn}(m_2)$. If $|m_{1,2}| < m_c$, then both regions will be topologically nontrivial ($\nu = 1$). While spin-helical edge states will exist at the sample edge, no topological edge states will exist at the boundary between the two regions because the topology does not change across this boundary. Similarly, if $|m_{1,2}| > m_c$ and $\mathrm{sgn}(m_1) = \mathrm{sgn}(m_2)$, both regions will be topologically trivial ($\nu = 0$) and no edge states will exist at the boundary.

In the second case (Fig. 3.3, orange) only one of the mass parameters is smaller than the critical mass $|m_i| < m_c$ while the other one is larger $|m_{i'}| > m_c$. The region where $|m_i| < m_c$ is topologically nontrivial ($\nu = 1$) while the other one is topologically trivial ($\nu = 0$). Due to the change in topology across the boundary, spin-helical topological edge states exist localized at the boundary between the two regions. The edge states are Kramers partners and are hence protected from backscattering by time reversal symmetry.

Finally, in the third case (Fig. 3.3, green) both masses are larger than the critical mass $|m_{1,2}| > m_c$, but have opposite signs $\mathrm{sgn}(m_1) = -\mathrm{sgn}(m_2)$. Here, both regions are topologically trivial ($\nu = 0$) again. However, looking at the Chern number (3.14), we see that this number changes across the boundary for all spin and valley configurations due to the two large masses having opposite signs. This means that there will be topological edge states localized at the boundary of all spin and valley

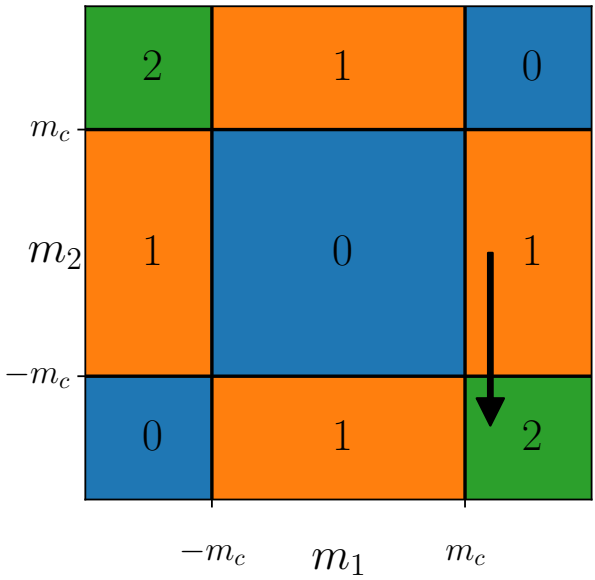

Figure 3.3: Phase diagram of silicene with two different mass parameters in different regions. The number in the rectangles indicates the number of sets of spin-helical edge states forming at the boundary between the two regions of different mass parameters. The black arrow is an example path to tune the edge states from spin-helical to spin-degenerate. Figure adapted from the original publication [53] which has been published under the Creative Commons Attribution License (https://creativecommons.org/licenses/by/4.0/).

polarizations. Overall, the edge states at this boundary are spin-degenerate, which can be separated into two sets of spin-helical edge states. The existence of these edge states does not contradict the topological $\mathbb{Z}_2$ invariant not changing across the boundary because these edge states are not topologically protected against backscattering. This lack of topological protection will become important again in the following sections.

Using these three regimes, we can make out an interesting tunability of edge states at a boundary between two regions in silicene (Fig. 3.3, black arrow). If one starts in a situation where one of the two mass parameters is larger than the critical mass, for instance $m_1 > m_c$, while the other one is vanishing $m_2 = 0$, spin-helical topologically protected edge states will exist at the boundary between the two domains. By increasing the second mass term (by applying an electric field), albeit with an opposite sign to the first mass parameter, we can tune the system into a regime where the edge states at the boundary are spin-degenerate and not topologically protected (Fig. 3.3, black arrow). By introducing the second set of spin-helical edge states, we also introduce backscattering into the channels without destroying their existence.

3.2.2 Edge States

With the Chern number we can predict the existence of topological edge states and the parameter regimes in which they are present. However, information like the energy dispersion as well as the wave function of the edge states cannot be derived from the Chern number. To obtain this information, we need to directly calculate the edge states.

One way to do this is to solve the Schrödinger equation $h(\boldsymbol{x})\boldsymbol{\Lambda}(\boldsymbol{x}) = \varepsilon\boldsymbol{\Lambda}(\boldsymbol{x})$ in both half spaces $y < 0$ and $y > 0$ independent of each other and match their wave functions at the

interface $y = 0$. Doing so reveals the linear energy dispersion

$$\varepsilon_{k_x} = \pm\eta\hbar v_F k_x \tag{3.17}$$

of the topological edge states. The sign is determined by the concrete implementation of the mass parameters. Otherwise, the energy dispersion is independent of both mass parameters and spin-orbit interaction, unlike voltage induced gaps in similar structures like bilayer graphene [92, 93].

In the case where $|m_1| < \Delta_{SO} < m_2$ the first region is topologically nontrivial and the second is topologically trivial (see Fig. 3.3, orange) so that one set of spin-helical edge states exists localized at the boundary. The corresponding eigenspinors are given by

$$\mathbf{\Lambda}(\boldsymbol{x}) = e^{-ik_x x} f(y) \frac{1}{\sqrt{2}} \begin{pmatrix} 1 \\ -1 \end{pmatrix} \tag{3.18}$$

where the basis is either $(c_{AK\uparrow}(\boldsymbol{x}), c_{BK\uparrow}(\boldsymbol{x}))^T$ for the first edge state, or $(c_{AK'\downarrow}(\boldsymbol{x}),\ c_{BK'\downarrow}(\boldsymbol{x}))^T$ for the second edge state. The first state therefore corresponds to a spin up polarized channel at the K valley while the second corresponds to a spin down polarized channel at the K' valley.

Looking at the enveloping function

$$f(y) = \frac{1}{\sqrt{\mathcal{N}}} e^{-\frac{|m-\Delta_{SO}|}{\hbar v_F}|y|}, \qquad m = \begin{cases} m_1 & y < 0 \\ m_2 & y > 0 \end{cases} \tag{3.19}$$

where $\mathcal{N}$ is a normalization factor so that $\int dy\, |f(y)|^2 = 1$ we see that the topological edge states are indeed localized at the boundary between the two regions $y = 0$ and decay exponentially away from the boundary on the length scale $\hbar v_F / |m - \Delta_{SO}|$.

3.3 Josephson Junction

With the ability of tuning topological edge states at the boundary between the two regions shown in Fig. 3.1 from spin-helical to spin-degenerate via the path shown as a black arrow in Fig. 3.3 we can turn our attention to Josephson junctions mediated by these edge states by including the superconductivity $\mathcal{H}_S$, but still neglecting intervalley scattering $\mathcal{H}_I$. Because the proximity induced superconducting gap will generally be smaller than the gap due to spin-orbit interaction and electric fields [46, 94], we can focus on the topological edge states inside the gap. To that end we first project the Hamiltonian onto the subspace spanned by the edge states.

3.3.1 Projected Hamiltonian

Without loss of generality we assume the electric fields to be configured so that $|m_1| < \Delta_{SO} < m_2$. The first region ($y < 0$) is therefore topologically nontrivial ($\nu = 1$) while the second one ($y > 0$) is topologically trivial ($\nu = 0$). While the gap parameter $M(y)$ will always be positive in the second region ($M(y > 0) > 0$), the gap parameter in the first region will be negative if $\xi\eta = 1$ and positive if $\xi\eta = -1$. Because the gap parameter must change its sign across the boundary in order for edge states to exist localized at the boundary, edge states only exist for $\xi\eta = 1$. This condition means that the edge state on valley K will be spin up polarized while the edge state on the K' valley will be spin down polarized. Using eq. (3.3) in conjunction with the wave function of the topological edge states (3.18), we can write down the field

operators of the topological edge states

$$\gamma_{k_x\sigma} = \int dx\, e^{-ik_x x} c_\sigma(x) \tag{3.20}$$

where the field operators

$$\begin{aligned} c_\uparrow(x) &= \int dy f(y) \frac{1}{\sqrt{2}} \left[c_{AK\uparrow}(\boldsymbol{x}) - c_{BK\uparrow}(\boldsymbol{x}) \right], \\ c_\downarrow(x) &= \int dy f(y) \frac{1}{\sqrt{2}} \left[c_{AK'\downarrow}(\boldsymbol{x}) - c_{BK'\downarrow}(\boldsymbol{x}) \right] \end{aligned} \tag{3.21}$$

annihilate an electron at position x along the channel in the spin up polarized channel at valley K or in the spin down polarized channel at valley K' respectively.

Using the linear dispersion of the topological edge states (3.17), we can project the Hamiltonian onto the subspace spanned by the two topological edge states (3.21)

$$\begin{aligned} H &\approx \frac{1}{2} \int dx \tilde{\psi}^\dagger(x) \tilde{h}(x) \tilde{\psi}(x), \\ \tilde{h}(x) &= \begin{pmatrix} i\hbar v_F \partial_x & 0 & \Delta e^{-i\phi} & 0 \\ 0 & -i\hbar v_F \partial_x & 0 & \Delta e^{-i\phi} \\ \Delta e^{i\phi} & 0 & -i\hbar v_F \partial_x & 0 \\ 0 & \Delta e^{i\phi} & 0 & i\hbar v_F \partial_x \end{pmatrix} \\ &= i\hbar v_F \rho_z s_z \partial_x + \Delta(\cos(\phi)\rho_x + \sin(\phi)\rho_y) \end{aligned} \tag{3.22}$$

where we have used the basis

$$\tilde{\psi}(x) = (c_\uparrow(x), c_\downarrow(x), c_\downarrow^\dagger(x), -c_\uparrow^\dagger(x))^T. \tag{3.23}$$

The Pauli matrices s_z again act in the spin subspace and therefore distinguish between the two topological edge states (3.21)[2]. Because the Hamiltonian $\tilde{h}(x)$ is symmetric in the spin subspace,

[2] Because the spin is locked to the valley, we could have also used τ_z instead of s_z to distinguish between the two edge states.

we can again replace it with the signs $\xi = \pm 1$ and obtain the simplified Hamiltonian

$$\begin{aligned} H &\approx \frac{1}{2} \int dx \hat{\psi}^\dagger(x) \hat{h}(x) \hat{\psi}(x), \\ \hat{h}(x) &= i\xi\hbar v_F \rho_z \partial_x + \Delta(\cos(\phi)\rho_x + \sin(\phi)\rho_y) \end{aligned} \tag{3.24}$$

and basis

$$\hat{\psi}(x) = \begin{cases} (c_\uparrow(x), c_\downarrow^\dagger(x))^T, & \xi = 1 \\ (c_\downarrow(x), -c_\uparrow^\dagger(x))^T, & \xi = -1. \end{cases} \tag{3.25}$$

This decoupling is a consequence of time reversal symmetry because the two topological edge states of opposite spins are Kramers partners and coupling between them is hence forbidden by symmetry.

3.3.2 Short Junction

The Hamiltonian (3.24) is valid for general (spatially dependent) forms of Δ and ϕ and can therefore be used to analyze Josephson junctions mediated by topological edge states like in Fig. 3.1. We start by looking at a short junction, i.e. a junction where the length between the two superconductors l is small compared to the superconducting coherence length $\xi_0 = \hbar v_F / \Delta$. We model such a junction with a constant $\Delta > 0$ and a spatially dependent phase

$$\phi(x) = \begin{cases} 0, & x < 0 \\ \phi, & x > 0. \end{cases} \tag{3.26}$$

Solving the Schrödinger equation in both half spaces $x < 0$ and $x > 0$ independently of each other and matching their wave

functions at the interface yields the in-gap state field operators

$$\begin{aligned}\Gamma_1 &= \int dx\, \varphi(x) \frac{1}{\sqrt{2}} \left[e^{i\theta} c_\uparrow(x) + c_\downarrow^\dagger(x) \right], \\ \Gamma_2 &= \int dx\, \varphi(x) \frac{i}{\sqrt{2}} \left[e^{-i\theta} c_\downarrow(x) - c_\uparrow^\dagger(x) \right]\end{aligned} \tag{3.27}$$

with

$$\theta = \arg\left(\varepsilon + i\sqrt{\Delta^2 - \varepsilon^2} \right). \tag{3.28}$$

They are equal weight superpositions of electrons and holes. Looking at the enveloping function

$$\varphi(x) = \sqrt{\frac{\sqrt{\Delta^2 - \varepsilon^2}}{\hbar v_F}} e^{-\frac{\sqrt{\Delta^2 - \varepsilon^2}}{\hbar v_F}|x|}, \tag{3.29}$$

we see that they are exponentially localized at the boundary between the two superconductors. These bound states are called Andreev bound states[3]. They obey the energy phase relation

$$\varepsilon(\phi) = \pm\Delta \cos\left(\frac{\phi}{2}\right), \tag{3.30}$$

which is 4π periodic in the phase difference across the junction ϕ (Fig. 3.4, blue). This 4π periodicity is the hallmark of the fractional Josephson effect and is often used as an indicator for the existence of Majorana fermions. It is protected by fermion parity conservation inside the junction. Because the current through the junction is proportional to the derivative $\partial_\phi \varepsilon$ [95], the current phase relation should also be 4π periodic.

At phase difference $\phi = \pi$ the Andreev bound states lie at zero energy $\varepsilon = 0$ so that $\theta = \pi/2$. The Andreev bound state

[3] The name arises from the possibility of explaining the existence of these bound states via two consecutive Andreev reflections at both superconductors [95].

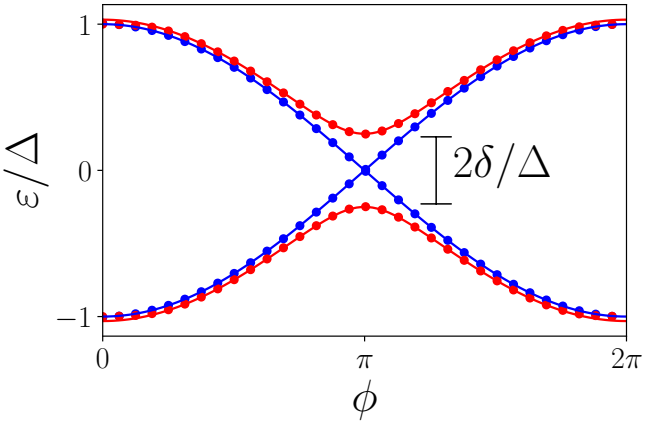

Figure 3.4: Energy phase relation of the Andreev bound states. In the spin-helical case (blue) the energy phase relation crosses zero energy at $\phi = \pi$ and is 4π periodic. When the edge states are spin-degenerate, an energy gap of δ opens at zero energy due to intervalley scattering and the resulting energy phase relation is only 2π periodic. The solid lines are the analytic results (3.30) and the dots are obtained by numerically diagonalizing the discretized Hamiltonian (2.32) (see App. A). Figure taken from the original publication [52].

field operators therefore simplify to

$$\begin{aligned}\Gamma_1|_{\varepsilon=0} &= \int dx\, \frac{\varphi(x)}{\sqrt{2}} \left[c_\downarrow^\dagger(x) + i c_\uparrow(x)\right], \\ \Gamma_2|_{\varepsilon=0} &= \int dx\, \frac{\varphi(x)}{\sqrt{2}} \left[c_\downarrow(x) - i c_\uparrow^\dagger(x)\right]\end{aligned} \tag{3.31}$$

so that it is easy to see that

$$\Gamma_1^\dagger|_{\varepsilon=0} = \Gamma_2|_{\varepsilon=0}. \tag{3.32}$$

With eq. (3.32) we can see that the linear combinations[4]

$$\begin{aligned}\gamma_1 &= \left.\frac{(\Gamma_1 + \Gamma_2)}{\sqrt{2}}\right|_{\varepsilon=0} \\ &= \int dx\, \frac{\varphi(x)}{2} \left[c_\downarrow(x) + c_\downarrow^\dagger(x) + i\left\{c_\uparrow(x) - c_\uparrow^\dagger(x)\right\}\right], \\ \gamma_2 &= \left.\frac{i(\Gamma_2 - \Gamma_1)}{\sqrt{2}}\right|_{\varepsilon=0} \\ &= \int dx\, \frac{\varphi(x)}{2} \left[c_\uparrow(x) + c_\uparrow^\dagger(x) + i\left\{c_\downarrow(x) - c_\downarrow^\dagger(x)\right\}\right]\end{aligned} \tag{3.33}$$

fulfill the Majorana condition

$$\gamma_1^\dagger = \gamma_1, \qquad \gamma_2^\dagger = \gamma_2. \tag{3.34}$$

The Josephson junction mediated by spin-helical topological edge states therefore hosts two Majorana excitations at zero energy and features a 4π periodic energy phase relation.

3.3.3 Intervalley Scattering

When we now tune the electric field in the first region ($y < 0$) from $|m_1| < \Delta_{SO}$ to $m_1 < -\Delta_{SO}$, the first region also becomes

[4] Here we have included an additional sign in the definition of γ_2 compared to the convention in [52].

topologically trivial. However, as discussed in Sec. 3.2, the edge states at the boundary between the two regions ($y = 0$) go from being spin-helical to spin-degenerate. As a consequence, these edge states are now no longer topologically protected.

Projecting the Hamiltonian onto the now spin-degenerate edge states, one can see that in the absence of intervalley scattering $\mathcal{H}_I$ the projected Hamiltonian decouples into two independent sets of Hamiltonians of the form (3.22). Therefore, the junction will host four Andreev bound states with a twofold degenerate 4π periodic energy phase relation (3.30). At phase difference $\phi = \pi$ these four Andreev bound states all lie at zero energy and form four Majorana excitations. While the two Majorana excitations from one individual decoupled Hamiltonian cannot couple due to being Kramers partners, finite matrix elements between Majorana excitations of different decoupled Hamiltonians are allowed by symmetry. The inclusion of intervalley scattering $\mathcal{H}_I$ results in such a matrix element of size $|\delta|$ and couples the four Andreev bound states. Therefore, a gap of size $2\,|\delta|$ opens in the energy phase relation

$$\varepsilon(\phi) = \pm\Delta\sqrt{\cos^2\left(\frac{\phi}{2}\right) + \left(\frac{\delta}{\Delta}\right)^2}, \tag{3.35}$$

which is now 2π periodic (Fig. 3.4, red). This gap opening is a consequence of the edge states at the boundary between the two regions ($y = 0$) no longer being topologically protected against backscattering. This scattering in turn can change the fermion parity and breaks the parity conservation, which protected the crossing at zero energy.

Up to now we have neglected a finite chemical potential as it would not have changed the results significantly. It does however have a profound impact on the intervalley scattering. Including a finite chemical potential μ, the wave function of the Andreev bound states (3.29) acquires an additional phase $e^{-i\mu x}$, which

changes the size of the matrix element between the Andreev bound states from $|\delta|$ to $|\delta|/(1+(\lambda\mu)^2)$ with $\lambda^{-1}=\sqrt{\Delta^2-\varepsilon^2}$. The scattering between the Andreev bound states therefore gets suppressed at higher chemical potentials or at energies near the superconducting gap $\varepsilon \to \pm\Delta$.

Due to the Majorana excitations coupling and creating a gap in the spectrum, these excitations no longer fulfill the Majorana condition $\gamma^\dagger = \gamma$ and are therefore rendered normal Andreev bound states. We have therefore, by changing the strength of one electric field applied perpendicular to the silicene sheet, tuned the junction from a topological state hosting Majorana excitations to a nontopological state without Majorana excitations.

3.3.4 Long Junction

The analytic calculation of the Andreev bound states was performed in the short junction limit ($l \ll \xi_0$). However, some experimental realizations of topological Josephson junctions have a distance between the two superconductors of $l \approx 400$ nm - 600 nm [47, 48]. With a Fermi velocity $v_F \approx 5.5\times10^5$ m/s and a typical superconducting gap $\Delta \approx 1$ meV, the superconducting coherence length $\xi_0 \approx 357$ nm would be shorter[5] than these distances l, which would in turn mean these junctions lie in the intermediate to long regime.

To show that the above described tunability remains into the long junction regime, we numerically diagonalize (see App. A) the discretized Hamiltonian (2.32) for $l \gg \xi_0$ (Fig. 3.5). Unlike in the short junction, we now find more than two Andreev bound states

[5] This assumes that the gap of the induced superconductivity is as large as the superconducting gap of the host superconductor. In real samples however the induced superconducting gap will generally be smaller than the superconducting gap of the host superconductor due to an imperfect interface between host superconductor and the silicene sheet.

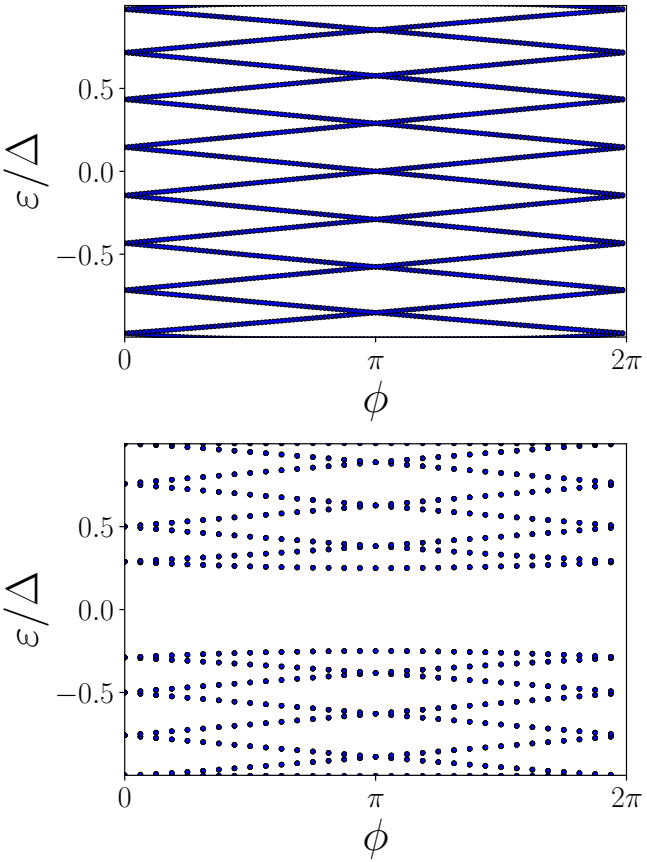

Figure 3.5: Energy phase relation of a long Josephson junction obtained by numerically diagonalizing the discretized Hamiltonian (2.32). In the spin-helical regime (top) the energies of the Andreev bound states extend to zero energy with Majorana excitations at zero energy. In the spin-degenerate regime (bottom) a gap opens due to intervalley scattering and no Majorana excitations at zero energy are present. Figure taken from the original publication [52].

localized inside the junction, which feature a linear energy phase relation [78, 96–98]. In the spin-helical case (Fig. 3.5, top) two of these Andreev bound states lie at zero energy at $\phi = \pi$ and are Majorana excitations like in the short junction case. Similarly, tuning the system to host spin-degenerate edge states (Fig. 3.5, bottom) instead of spin-helical ones opens up a gap at zero energy due to intervalley scattering. This gap opening again destroys the Majorana excitations and turns them into simple Andreev bound states. The ability to tune the Josephson junction from a topological one hosting two Majorana excitations to a nontopological one hosting no Majorana excitations by changing an applied electric field is therefore not specific to the short junction regime but is also present in the long junctions.

One way to build the proposed system is to apply the electric fields with top and bottom gates. In such a case the electric fields would not reach into the superconducting region due to the screening effect of the superconductors. The mass parameters $m_{1,2}$ would therefore vanish in the regions below the superconductor and these regions would then become topologically nontrivial ($\nu = 1$). We can treat this scenario numerically by diagonalizing the tight binding Hamiltonian (2.34). Also, we choose a setup with three electric fields where the regions with E_1 are topologically trivial and the region with E_2 is topologically nontrivial so that no Andreev bound states are localized along the sample edge to remove possible effects introduced by the hard edge boundary condition in the tight binding model.

Looking at the energy phase relation in this scenario (Fig. 3.6, top), we see that it is made up of two components. First, at lower energies the energy phase relation resembles that of the long junction where the electric fields reach into the superconductor (Fig. 3.5, top). However, at energies $\varepsilon \approx \pm\Delta/2$ we see additional states which do not disperse with the phase difference across the junction ϕ. Unlike the states at low energies (Fig. 3.6, bottom), these states are localized at the boundary between the

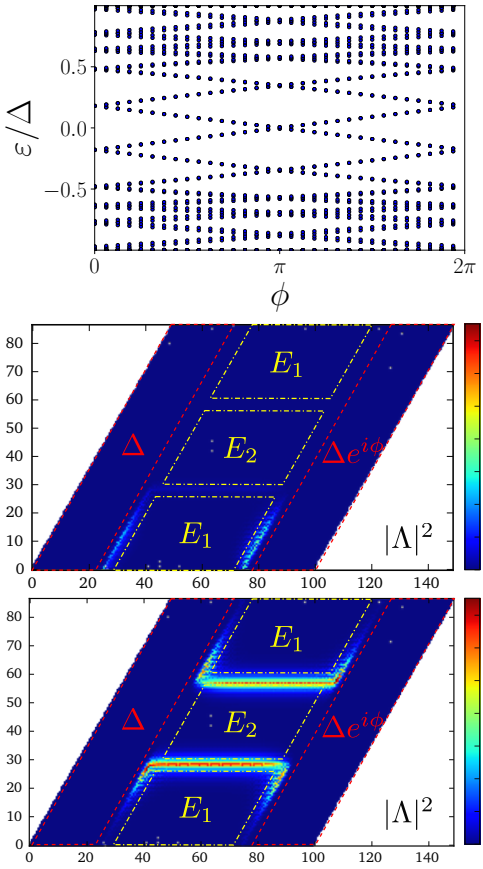

Figure 3.6: Energy phase relation (top) of a long junction without electric fields below the superconductors obtained by numerically diagonalizing the tight binding Hamiltonian (2.34). Additional nondispersive states are present at $\varepsilon \approx \pm\Delta/2$. These states are localized at the boundaries of the superconductors (middle) while the dispersive states around $\varepsilon \approx 0$ (bottom) are localized along the channels defined by the electric fields. The boundaries between the different regions touch and are only drawn with a spatial gap between them for better visibility. Figure taken from the original publication [52]. ©2018 American Physical Society

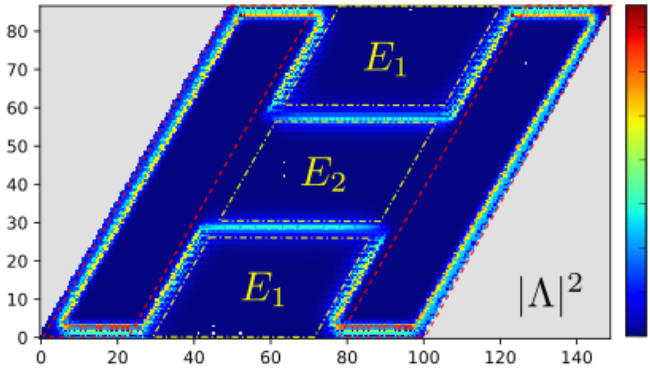

Figure 3.7: Wave function of topological edge states running around the topologically nontrivial regions E_2 and the region below the superconductors (red rectangles) in the case of a vanishing superconducting gap $\Delta = 0$. A small region around the edge of the sample was tuned to be topologically trivial to push the edge states away from the sample edge to reduce edge specific effects.

superconductor and the regions with finite electric fields (Fig. 3.6, middle) and hence do not contribute to the Josephson current.

One way to understand the existence of these additional states is to look at the system without superconductivity. The only topologically trivial regimes in the setup Fig. 3.6 are the regions with the electric field E_1. Therefore, spin-helical edge states run around the (topologically nontrivial) regions below the superconductors and bend into the sample at the boundaries between the superconductors and the electric fields (Fig. 3.7). Therefore, topological edge states exist at the boundary between the superconducting region and the topologically trivial regions with elec-

tric field E_1. Reintroducing the superconductivity, these states get gapped. But since only part of their wave function lies in the superconducting region, the gap opened is smaller than Δ. Another way to explain the existence of these in-gap states is to look at a boundary between a superconducting region and a region with a finite electric field and calculate the in-gap states analytically through solving the Schrödinger equation in both half spaces independent of each other and matching their wave functions at the interface.

However, in the case where the electric fields can reach 5 lattice sites into the superconducting regions (Fig. 3.8) and vanish beyond that point these additional states at $\varepsilon = \approx \pm\Delta/2$ are no longer present (Fig. 3.8, top). Furthermore, the wave function at zero energy (Fig. 3.8, bottom) is now well localized in the y-direction, even at the boundary to the superconducting region. In comparison, the same state will have a finite wave function localized at the boundary to the superconductor if the electric field vanishes uniformly inside the superconducting region (Fig. 3.6, bottom). This in turn supports the hypothesis that the additional states are remnants of the topological edge states running along the edge to the superconductors in the case of vanishing superconducting gap $\Delta = 0$ (Fig. 3.7).

Because these additional states do not contribute to the Josephson current due to their nondispersive energy phase relation and because the spectrum is unchanged at low energies, the ability to tune the junction from topologically nontrivial to topologically trivial by altering the electric fields stays unchanged.

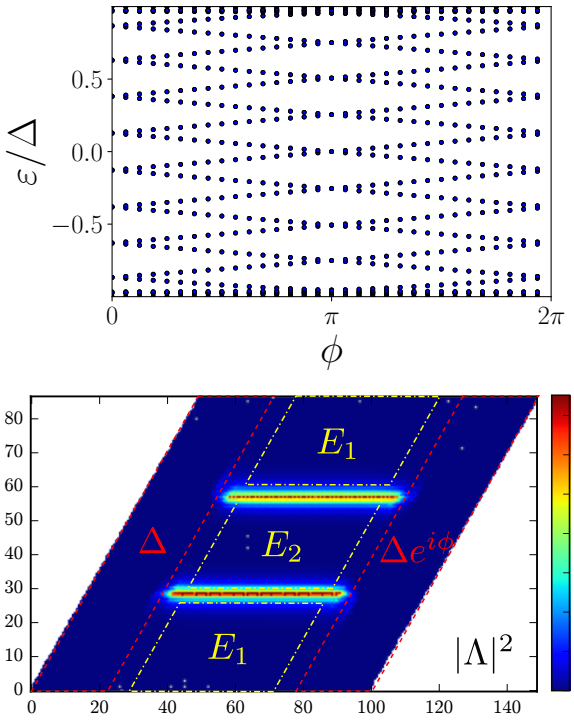

Figure 3.8: Energy phase relation (top) and wave function of a zero energy state (bottom) for electric fields reaching only 5 lattice sites into the superconducting region obtained by numerically diagonalizing the tight binding Hamiltonian (2.34). The additional states at $\varepsilon \approx \pm\Delta/2$ are no longer present and the wave function at zero energy is well localized in the y-direction. Figure taken from the original publication [52].

3.4 Tunable Poisoning

In Sec. 3.3 we have shown how the tunability described in Sec. 3.2 can be used to tune a Josephson junction in silicene from topologically nontrivial to topologically trivial. One possible way to measure the change in periodicity of the energy phase relation and therefore also the current phase relation is to look at the change in critical current predicted by Beenakker *et al.* in [78]. However, because the Josephson current is carried by two sets of spin-helical edge states in the setup proposed above, the critical current can be doubled depending on the overall parity of the junction [79] complicating a measurement. To avoid this problem, we propose a mass configuration shown in Fig. 3.9. In such a setup a single set of spin-helical edge states connects to the two superconductors carrying the Josephson current of the topological Josephson junction. A second set of spin-helical edge states connects to the first, but instead of connecting to the superconductors it connects to a separate lead instead. Due to intervalley scattering, electrons from the edge states connecting the superconductors can scatter into the other set of spin-helical edge states and tunnel into the lead. This process breaks parity conservation inside the Josephson junction and should hence also turn the junction topologically trivial with a 2π periodic energy phase relation. Because the second set of edge states does not connect the superconductors, it does not contribute to the Josephson current. Removing the second set of edge states, for instance, by removing the electric field in the lower central region of Fig. 3.9 in turn restores the topological nature of the Josephson junction and the 4π periodicity of its energy phase relation.

To verify this hypothesis, we expand the low energy Hamil-

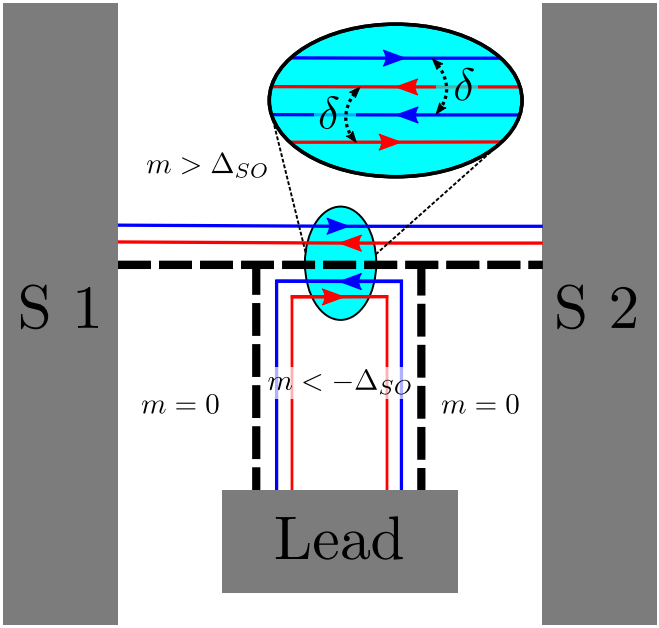

Figure 3.9: Setup for tunable poisoning in a Josephson junction. Spin-helical (with blue and red representing spin up and down polarization) edge states run from one superconductor to the other facilitating the topological Josephson junction. A second set of spin-helical edge states gets coupled to the first set but does not connect to the superconductors but to a lead allowing for dissipation. Figure taken from the original publication [52].

tonian in its instantaneous eigenstates

$$H = \frac{1}{2}\left(\varepsilon_1 \Gamma_1^\dagger \Gamma_1 + \varepsilon_2 \Gamma_2^\dagger \Gamma_2\right) = \varepsilon\left(\Gamma_1^\dagger \Gamma_1 - \frac{1}{2}\right) \tag{3.36}$$

where we have used the particle hole symmetry

$$\varepsilon_1 = -\varepsilon_2 \equiv \varepsilon, \qquad \Gamma_1 = \Gamma_2^\dagger \tag{3.37}$$

and we assume $\varepsilon > 0$ without loss of generality. The Hilbert space is spanned by the two eigenstates $|0\rangle$ and $|1\rangle$ where $|1\rangle = \Gamma_1^\dagger |0\rangle$ and $\Gamma_1 |0\rangle = 0$.

The tunneling is assumed to be limited to a pointlike region

$$H_T = t \sum_\sigma c_{L\sigma}(0) c_{R\sigma}^\dagger(0) + \text{H.c.} \tag{3.38}$$

where t is a tunnel matrix element determined by microscopic parameters. The field operators $c_{L/R\sigma}$ annihilate an electron with spin polarization σ in the edge state L/R where L denotes the edge states facilitating the Josephson effect and R denotes the edge states coupled to the lead.

If the tunneling between the two sets of edge states is weak, we can treat it perturbatively using Fermi's golden rule. To that end we expand the edge states $c_{L\sigma}$ in terms of the Andreev bound states. The Andreev bound state Γ_1 is given by

$$\Gamma_1 = \int dx \, \frac{\varphi(x)}{\sqrt{2}} (e^{i\theta}, 0, 1, 0) \mathbf{\Phi}(x) \tag{3.39}$$

where

$$\mathbf{\Phi}(x) = (c_{L\uparrow}(x), c_{L\downarrow}(x), c_{L\downarrow}^\dagger(x), -c_{L\uparrow}^\dagger(x))^T. \tag{3.40}$$

With this we can approximate the edge state field operators as[6]

$$\mathbf{\Phi}(x) \approx \frac{\varphi(x)}{\sqrt{2}}(e^{-i\theta}\Gamma_1, \Gamma_1^\dagger, \Gamma_1, -e^{i\theta}\Gamma_1^\dagger)^T. \tag{3.41}$$

The edge states connected to the lead can be expanded in plane wave states

$$c_{R\sigma}(x) = \frac{1}{\sqrt{\bar{l}}}\sum_k e^{ikx} c_{Rk\sigma} \tag{3.42}$$

where $\bar{l}$ is their quantization length.

Using these two expansions, we can rewrite the tunneling Hamiltonian (3.38) as

$$H_T = \frac{t^*\varphi(0)}{\sqrt{2\bar{l}}}\sum_k \left(c_{Rk\uparrow}\Gamma_1^\dagger e^{i\theta} + c_{Rk\downarrow}\Gamma_1\right) + \text{H.c.}. \tag{3.43}$$

The rate at which the ground state $|0\rangle$ goes to the excited state $|1\rangle = \Gamma_1|0\rangle$ is given by Fermi's golden rule

$$W_{10} = \frac{2\pi}{\hbar}\sum_{if} \rho_i \left|\langle f|H_T|i\rangle\right|^2 \delta(E_i - E_f) \tag{3.44}$$

where ρ_i is the probability of finding the system in the initial state $|i\rangle = |0\rangle|\phi_i\rangle$ with $|\phi_i\rangle$ being the initial state of the edge states coupled to the lead.

Possible final states are

$$|f\rangle = c_{Rk\downarrow}^\dagger|1\rangle|\phi_i\rangle \text{ and } |f\rangle = c_{Rk\uparrow}|1\rangle|\phi_i\rangle. \tag{3.45}$$

An excitation from $|0\rangle$ to $|1\rangle$ can therefore occur either by annihilating, or creating an electron on the edge states connected

[6] This approximation neglects the contributions from subgap states which are localized not between the two superconductors but on the outer edges of the superconductor. While these states can significantly contribute to the expansion of the edge states $\mathbf{\Phi}(x)$, they have a small wave function in the scattering region between the two superconductors and hence do not significantly contribute to the matrix element to be calculated.

to the lead, which is a result of the Andreev bound states being superpositions of both electrons and holes. The delta function in the rate expresses the conservation of energy during a scattering event. The energy of the initial state

$$E_i = \varepsilon_{\phi_i} - \frac{\varepsilon}{2} \tag{3.46}$$

is made up of the energy of the edge states connected to the lead (first part) and the Andreev bound state (second part). The energy of the final states are therefore

$$E_f = \varepsilon_{\phi_i} \pm \varepsilon_{k\downarrow/\uparrow} + \frac{\varepsilon}{2} \tag{3.47}$$

with $\varepsilon_{k\sigma}$ being the energy of a single electron with wave vector k and spin polarization σ in the edge states connected to the lead.

Combining this with

$$\sum_i \rho_i \langle \phi_i | c^\dagger_{Rk\sigma} c_{Rk\sigma} | \phi_i \rangle = \mathrm{Tr}[\rho c^\dagger_{Rk\sigma} c_{Rk\sigma}] = f(\varepsilon_{k\sigma}) \tag{3.48}$$

where $f(\cdot)$ is the Fermi function in the edge states connected to the lead, we can find the excitation rate due to the tunneling between the two sets of edge states to be

$$W_{10} = \gamma_t \varphi^2(0) f(\varepsilon) \tag{3.49}$$

where $\gamma_t = 2\pi\nu|t|^2/\hbar$ and ν is the density of states per length of the edge states connected to the lead at energy ε. Performing the same steps for relaxation processes yields the rate

$$W_{01} = \gamma_t \varphi^2(0)(1 - f(\varepsilon)). \tag{3.50}$$

The dynamics of the junction can be described with a master equation

$$\begin{aligned} \dot{\rho}_{00} = &\quad -W_{10}\rho_{00} + W_{01}\rho_{11}, \\ \dot{\rho}_{11} = &\quad W_{10}\rho_{00} - W_{01}\rho_{11} \end{aligned} \tag{3.51}$$

where ρ_{00} and ρ_{11} are the diagonal elements of the reduced density matrix describing the Andreev bound states. The off-diagonal elements decay exponentially. Using the normalization condition $\rho_{00} + \rho_{11} = 1$, the steady state solution is given by

$$\rho_{11} = \frac{W_{10}}{W_{10} + W_{01}} = f(\varepsilon), \tag{3.52}$$

which for low temperatures of the lead $T \to 0$ and no voltage drop between the superconductors and the lead is exponentially suppressed $\rho_{11} \sim \exp[-\varepsilon/(k_B T)]$. The system therefore stays in the instantaneous ground state $|0\rangle$ and features a 2π periodic energy phase relation.

Performing a critical current measurement of the system shown in Fig. 3.9 therefore should yield two different critical currents depending on whether or not the second set of edge states connected to the lead couples to the first set facilitating the Josephson effect. In order for such a measurement to be possible we require $\gamma_t^{-1} \ll \tau_J \ll \tau_{qp}$ where τ_J and τ_{qp} are the intrinsic time scale of the junction and the intrinsic quasiparticle poisoning time respectively.

3.5 Conclusion

Josephson junctions mediated by topological edge states in a sheet of silicene defined by electric fields offer a novel way to access the properties of topological Josephson junctions. First, we have shown in Sec. 3.2 by calculating the spin- and valley-dependent Chern numbers that the topology of silicene can be tuned by applying an electric field perpendicular to the silicene sheet and directly manipulating the induced mass parameter. We have further illustrated a way to tune topological edge states

forming at boundaries between regions of different electric fields from being valley-chiral and spin-helical to being valley-chiral and spin-degenerate.

When these edge states are used to build a Josephson junction, Andreev bound states form inside the junction. We have calculated these Andreev bound states analytically in the short junction limit and numerically in the long junction limit in Sec. 3.3. In the case where the edge states are spin-helical the resulting Andreev bound state energy phase relation resembles that of a Josephson junction mediated by the topological edge states of a quantum spin Hall insulator [25, 78]. Most notably, the energy phase relation is 4π periodic resulting in a 4π periodic Josephson current in the absence of fermion parity conservation breaking quasiparticle poisoning effects. At a phase difference of $\phi = \pi$ across the junction the Andreev bound states lie at zero energy and can be linearly combined to form two Majorana excitations.

When tuning the topological edge states to the spin-degenerate regime, the energy phase relation will generally be 2π periodic as intervalley scattering opens a gap at zero energy by coupling the Majorana excitations. In the absence of intervalley scattering the junction exhibits two sets of decoupled Andreev bound states of the form found in the spin-helical case. The periodicity of the energy phase relation and the Josephson current would therefore depend on the overall parity of the junction like in a Josephson junction covering both edges of a quantum spin Hall insulator [79]. However, because intervalley scattering is allowed by symmetry, we expect it to generally be present and couple these two sets of Andreev bound states and in turn reduce the periodicity to 2π. We have checked numerically that the main results will stay unchanged if the electric fields defining the topological edge states do not reach into the superconductors like we would expect when using top and bottom gates to create the electric fields.

Furthermore, we have proposed a setup in which a first set of spin-helical edge states mediates a Josephson junction and a

second set of spin-helical edge states couples to them via intervalley scattering. However, instead of connecting to the superconductors, this second set of edge states connect to a separate lead inducing dissipation in the first set of edge states (Fig. 3.9). For small temperatures in the lead the junction will always relax to its instantaneous ground state resulting in a nontopological Josephson effect. Removing the second set of edge states connected to the lead by changing the mass parameter configuration in turn restores the topological nature of the Josephson junction. In such a tunable junction we could measure the topology of the junction by measuring the critical current as it should differ by a factor of two in the two cases [78].

Finally, it is important to note that silicene is not the only system featuring the described tunability. Aside from further 2D hexagonal lattices of group IV elements like germanene (Ge), stanene (Sn), and plumbene (Pb), which are similar in structure to silicene, double layer quantum wells in HgTe [99] or InAs/GaSb type II quantum wells [100, 101] are further systems in which mass domains can be defined by electric fields. Electrically tunable coupling between topological edge states has also been predicted in single HgTe quantum wells containing constrictions [102]. Furthermore, experimental signatures of topology have already been demonstrated in both systems [46, 48, 50, 103, 104]. Voltage induced mass gaps have also been experimentally realized in bilayer graphene [105–107] and been proposed to be used as a Cooper pair splitter [93]. However, the edge states forming at voltage domain walls are not topologically protected as there are always two edge states of the same spin and chirality per valley. Using curved bilayer graphene [108] or combining bilayer graphene with transition metal dichalcogenides [109–111] can be used to increase the comparatively small spin-orbit interaction in graphene.

4

Quasiparticle Poisoning in Josephson Junctions

In the last chapter we have proposed and analyzed in detail a Josephson junction in silicene in which we can switch between a Josephson junction that is topological and one that is nontopological by changing electric fields applied perpendicular to the silicene sheet. Such a junction can potentially be used to find experimental signatures of topological Josephson junctions. We

briefly mentioned quasiparticle poisoning breaking conservation of fermion parity and determined a parameter regime for the proposed experiment. In this chapter we turn our focus to this quasiparticle poisoning and its effects on the dynamical properties of fractional Josephson junctions.

Fractional Josephson junctions, that is Josephson junctions that are mediated by spin-helical edge states of quantum spin Hall insulators, feature a 4π periodic energy phase relation and current phase relation [23, 25, 45, 49, 77, 112, 113]. This 4π periodicity stands in stark contrast to the 2π periodicity of nontopological junctions. Despite this clear difference between the two cases, experimental detection is complicated by the junctions coupling to the environment. The 4π periodicity is a consequence of the fermion parity, that is the number or fermions in the junction modulo 2, being a conserved quantity [25]. In isolated junctions this fermion parity is conserved so that one should be able to measure a 4π periodicity. In realistic settings however the junction couples to the environment such that electrons can tunnel between the junction and the environment [42, 114]. This process, which is called quasiparticle poisoning, changes the number of fermions in the junction by 1, so that the fermion parity is changed [81, 115–117]. Fermion parity is hence not a conserved quantity and the 4π periodicity is reduced to the usual 2π periodicity.

To overcome this complication, experimental schemes mostly focusing on dynamical properties of the junction have been theoretically proposed [118–126] and first experimental signatures of the 4π have been reported [45–49]. One such dynamical property can be observed by driving the junction with a time-periodic current of frequency ω, which results in the formation of Shapiro steps in the current voltage characteristic at voltages $V_n = n\hbar\omega/2e$ where n is an integer [51, 127, 128]. When performing such an experiment with fractional junctions, odd Shapiro steps are missing [23, 45], an effect which could be experimentally demonstrated

[46] in Josephson junctions mediated by the helical edge states of HgTe quantum wells.

Another proposal [78] instead focuses on dc measurements in long Josephson junctions where the length between the two superconductors L is large compared to the superconducting coherence length $\xi_{sc} = \hbar v_F/\Delta$ with v_F being the Fermi velocity of the helical edge states [50, 103, 129] and Δ the induced superconducting gap. It has been proposed that in such junctions the critical current should differ by a factor of 2 when comparing topological with nontopological junctions as long as the quasiparticle poisoning is slow and coming from a reservoir with low temperature.

In this chapter we set out to analyze the effects that quasiparticle poisoning has on the dynamics of fractional Josephson junctions. We model the junction with the resistively shunted junction (RSJ) model [128, 130, 131] in the overdamped limit describing the junction in the absence of quasiparticle poisoning. We include the effects of poisoning via two methods. First, we follow the analysis of [132] and rewrite the differential equation describing the RSJ model in terms of the Fokker-Planck equation [132, 133] as well as include a random thermal driving of the phase to model a finite junction temperature T. As the Fokker-Planck equation has the form of a master equation, we can include quasiparticle poisoning by introducing parity changing rates. We model these rates with a constant poisoning rate Γ multiplied by an equilibrium Fermi distribution of temperature T_b which can generally differ from the junction temperature.

While the Fokker-Planck equations are suitable for junctions with finite junction temperature, recent experiments have reached temperatures far below the superconducting gap Δ as well as far below the Thouless energy $E_T = \hbar v_F/L$. For such junctions we will devise a second method to include quasiparticle poisoning in the RSJ model valid at zero junction temperature. In this second approach the poisoning events are assumed to occur in-

stantaneously at specific times. Between these times the parity of the junction is conserved such that the differential equation of the RSJ model can be numerically solved. By iteratively solving the differential equations between two times at which poisoning events occur, the time-dependent phase difference across the junction and with it the voltage drop across the junction can be determined.

We start in Sec. 4.1 by introducing the RSJ model and the two numerical methods to include quasiparticle poisoning into the RSJ model. Following that, in Sec. 4.2 we find the current voltage characteristic of fractional Josephson junctions in the limits of vanishing junction temperature and of fast or slow poisoning. Finite junction temperatures as well as the effects of quasiparticle poisoning onto the current voltage characteristic are discussed in Sec. 4.3. With the proposal of [78] in mind we turn our focus to the critical currents in the zero temperature limit in Sec. 4.4. In Sec. 4.5 we devise multiple experimental schemes to measure the rate with which poisoning events occur via voltage measurements. After extending our model to extended junctions mediated by two sets of spin-helical edge states with a constriction allowing for electron tunneling between the two edges in Sec. 4.6, we finally summarize our results and give a brief outlook to further possible investigations in Sec. 4.7.

4.1 Model

We model a Josephson junction with the resistively shunted junction (RSJ) model [128] where the junction is described by an equivalent circuit (Fig. 4.1). An ideal Josephson junction is connected in parallel to a resistance R. Here we neglect the existence of a geometric capacity C, which is justified if the time scale of

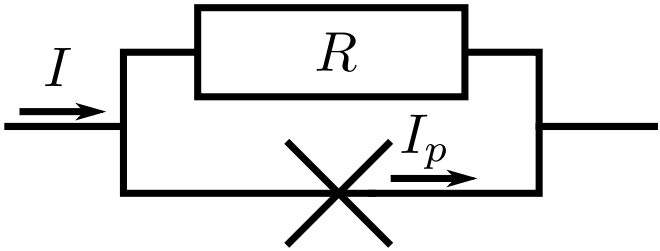

Figure 4.1: Equivalent circuit of a Josephson junction where an ideal junction (cross) is connected with a resistance R in parallel. The driving current I must be equal to the sum of the current through the junction I_p and the current through the resistor. Figure taken from the original publication [54]. ©2020 American Physical Society

the corresponding RC-circuit $\tau_{RC} = RC$ is small compared to the intrinsic time scale of the junction $\tau_J = \frac{\hbar}{2e}\frac{1}{I_c R}$ where I_c is the critical current of the junction [78, 128]. While the explicit values depend on the specific sample, typical values range between $R \sim 50 - 150\,\Omega$, $C \sim 1$ fF -1 aF, and $\tau_J \sim 10$ ps [46, 78, 94, 128]. Already fabricated junctions [46, 94] can therefore be described with the RSJ model.

Using Kirchhoff's rule, we can express the driving current through the entire circuit as

$$I = I_p(\phi) + \frac{V}{R} \tag{4.1}$$

where $I_p(\phi)$ is the current through the ideal Josephson junction and ϕ is the phase difference across the junction. The second term describes the current through the resistance described by Ohm's law where V is the voltage developing across the resistance which is equal to the voltage developing across the entire circuit by virtue of Kirchhoff's rule. Using the Josephson relation

$$V = \frac{\hbar}{2e}\dot{\phi}, \tag{4.2}$$

we can express the voltage developing across the junction as the time derivative of the phase difference across the junction. Inserting this into Kirchhoff's rule (4.1) yields

$$I = I_p(\phi) + \frac{\hbar}{2eR}\dot{\phi}, \tag{4.3}$$

which is a differential equation describing the dynamics of the Josephson junction. It holds for a fixed parity $p = 0$ (even) or $p = 1$ (odd). In order to analyze the effects that quasiparticle poisoning, which changes the parity p of the junction, has on the dynamics of the junction, we will have to adapt the model to allow for parity changes.

4.1.1 Fokker-Planck Equation

One way to introduce parity changing quasiparticle poisoning is to rewrite the differential equation (4.3) in terms of a Fokker-Planck equation. To that end, we can express the current flowing through an ideal Josephson junction as

$$I_p(\phi) = \frac{e}{\hbar}\partial_\phi E_p(\phi) \tag{4.4}$$

where $E_p(\phi)$ is the energy phase relation of the Josephson junction and we assume low junction temperatures. Inserting this into the differential equation (4.3), we get

$$\dot{\phi} = -\frac{\mu}{2}\partial_\phi U_p \tag{4.5}$$

where $\mu = 4e^2R/\hbar^2$ and

$$U_p = E_p(\phi) - \frac{\hbar I}{e}\phi. \tag{4.6}$$

Due to its form in short junctions, the potential U_p is often called the washboard potential [128].

For finite junction temperatures T thermal fluctuations can randomly drive the phase of the junction. Such effects can be included in eq. (4.5) via

$$\dot{\phi} = -\frac{\mu}{2}\partial_\phi U_p + \mu\zeta(t) \tag{4.7}$$

where the thermal driving $\zeta(t)$ is uncorrelated in time [132, 133]

$$\langle\zeta(t)\zeta(t')\rangle = \frac{k_B T\hbar^2}{2Re^2}\delta(t-t'). \tag{4.8}$$

Solving the differential equation (4.7) is equivalent to solving the Fokker-Planck equation [134, 135]

$$\partial_t \mathcal{P}_p = \mu\partial_\phi\left[\left(\frac{1}{2}\partial_\phi U_p\right)\mathcal{P}_p + k_B T\partial_\phi\mathcal{P}_p\right] \tag{4.9}$$

where $\mathcal{P}_p$ is the probability density of finding the junction at phase difference ϕ and in parity p.

Up to now this description does not include quasiparticle poisoning as each parity sector is described by an independent Fokker-Planck equation with an individual solution $\mathcal{P}_0$ or $\mathcal{P}_1$. Parity changing effects can be included by coupling the two differential equations of the two parity sectors. Because the Fokker-Planck equations have the form of a master equation, we can incorporate such coupling by adding additional terms of the form of transition rates [132]

$$\partial_t \mathcal{P}_p = \mu\partial_\phi\left[\left(\frac{1}{2}\partial_\phi U_p\right)\mathcal{P}_p + k_B T\partial_\phi\mathcal{P}_p\right] + \sum_{p'} W_{p'p}\mathcal{P}_{p'} - W_{pp'}\mathcal{P}_p \tag{4.10}$$

where $W_{pp'}$ is the rate the probability density $\mathcal{P}_p$ goes over into the probability density $\mathcal{P}_{p'}$[1]. Assuming the parity changing effects are due to electrons tunneling into or out of the junction,

[1] Due to multiple Andreev bound states forming inside of long Josephson junctions, there are multiple different states in a given parity sector. We

we can write these rates as [132]

$$W_{pp'} = \Gamma f\left[\frac{U_{p'} - U_p}{k_B T_b}\right] \tag{4.11}$$

where Γ is a constant poisoning rate specific to the system in question and $f[\cdot]$ is the Fermi function. The electrons facilitating the parity change come from a bath of temperature T_b which in general can be different from the junction temperature T.

In the Fokker-Planck formalism the voltage developing across the junction can be evaluated by [132]

$$V = \frac{\hbar}{2e}\langle\dot{\phi}\rangle = \frac{\hbar}{2e}\sum_p \int_0^{4\pi} d\phi\, \dot{\phi}\mathcal{P}_p = -\frac{eR}{\hbar}\sum_p \int_0^{4\pi} d\phi\, (\partial_\phi U_p)\mathcal{P}_p \tag{4.12}$$

where we have used eq. (4.5).

4.1.2 Time-Dependent Parity

The description via the Fokker-Planck equations assumes a finite junction temperature T. However, recent experiments in Josephson junctions have reached temperatures far below both the superconducting gap Δ and the Thouless energy $E_T = \hbar v_F/L$ where v_F is the Fermi velocity of the edge states facilitating the Josephson effect and L is the distance between the two superconductors forming the Josephson junction [46, 94]. We will therefore also want to look at the zero temperature limit. However, the Fokker-Planck equations no longer hold for low junction temperatures and driving currents below the critical current [135]. We

assume that the time it takes for the system to relax to the ground state within a given parity sector is much faster than all other time scales [136] so that the junction always evolves according to the ground state of each parity sector.

will therefore need to develop a new method to specifically look at the zero temperature limit.

To that end, we model quasiparticle poisoning as individual events that change the parity of the junction instantaneously, i.e. much faster than the timescale of the junction τ_J. Between the individual poisoning events the parity of the junction stays fixed so that the differential equation (4.3) holds. Numerically integrating this differential equation between two poisoning events yields the phase difference across the junction after this time interval and can be used as the initial condition to numerically solve the differential equation between the next two poisoning events. Performing these steps iteratively, we can find the time-dependent phase difference across the junction including poisoning events. Because the differential equation (4.3) holds at zero junction temperature, this model also describes the junction at zero temperature.

To implement this method, we start by randomly selecting (uniform distribution) $n = \mathrm{Int}(\Gamma\tau)$ [2] times t_i out of the time interval $[0, \tau]$. At these times the parity of the junction can change from p to p' with the probability $f[(U_{p'} - U_p)/(k_B T_b)]$ while it stays constant between these times. Iteratively solving the differential equation (4.3) between two times t_i and t_{i+1}, evaluating the probability of a parity flip at time t_{i+1}, and performing said parity change then results in the time-dependent phase $\phi(t)$ over the entire time interval $[0, \tau]$. The voltage developing across the junction can then be evaluated via

$$V = \frac{\hbar}{2e}\langle\dot{\phi}\rangle = \frac{\hbar}{2e}\frac{1}{\tau}\int_0^\tau dt\,\dot{\phi} = \frac{\hbar}{2e}\frac{\phi(\tau) - \phi(0)}{\tau}. \tag{4.13}$$

For this model to hold we require that $\tau \gg \tau_J; \Gamma^{-1}$.

[2] The function $\mathrm{Int}(\cdot)$ rounds to the nearest integer.

4.1.3 Energy Phase Relation of Topological Junctions

Both models described above can be applied to describe the dynamics of any Josephson junction including quasiparticle poisoning. However, we will focus on topological junctions in either the short junction ($L \ll \xi_{sc}$) or the long junction ($L \gg \xi_{sc}$) limit where ξ_{sc} is the superconducting coherence length.

The only point at which the specific type of junction enters our models is via its current phase relation $I_p(\phi)$ or its corresponding energy phase relation $E_p(\phi)$. The energy phase relation for short junction limit is given by [25]

$$E_p(\phi) = (-1)^p \Delta \cos\left(\frac{\phi}{2}\right) \tag{4.14}$$

and is 4π periodic since we consider topological Josephson junctions. To obtain the energy phase relation of the long junction limit, we can integrate the current phase relation given in [78] in the limit of $T \to 0, L \to \infty$ which yields

$$E_p(\phi) = \frac{E_T}{4\pi} \begin{cases} \begin{cases} \phi^2 & \phi \in [0, 2\pi) \\ (\phi - 4\pi)^2 & \phi \in [2\pi, 4\pi) \end{cases} & p = 0 \\ (\phi - 2\pi)^2 & p = 1 \end{cases} \tag{4.15}$$

for $\phi \in [0, 4\pi) \mod 4\pi$. While this energy phase relation was evaluated in the limit $T \to 0$, it will still be a good approximation if $k_B T < E_T$. Like in the short junction limit, it is 4π periodic, but now depends quadratically on the phase difference across the junction ϕ.

For the remainder of the chapter it will be beneficial to introduce normalized and dimensionless variables

$$\nu = \frac{V}{I_c R}, \qquad x = \frac{I}{I_c}, \qquad \gamma = \Gamma \tau_J \tag{4.16}$$

where $I_c = (e/\hbar)\xi$ and $\xi = \Delta$ or $\xi = E_T$ in the short or long junction limit respectively. It is important to note that in this definition I_c is not equal to the critical current in the short junction limit, but rather equal to twice the critical current. The intrinsic time scale of the junction $\tau_J = 2/(\mu\xi)$ [127] for junctions in question are on the order of $\tau_J \sim 10$ ps [46, 78, 94]. Intrinsic quasiparticle poisoning is expected to be on the order of $\tau_{qp} \sim 1\,\mu$s [81] so that in this case the junction should always be in the slow poisoning regime ($\gamma \ll 1$). However, artificial poisoning sources like described in Sec. 3.4 can potentially achieve higher poisoning rates. Furthermore, we will later discuss a scheme in which the normalized poisoning rate γ could potentially be increased. It will therefore be important to also look at the intermediate ($\gamma \sim 1$) and fast ($\gamma \gg 1$) poisoning regimes.

4.2 Effective Potentials

Both methods described in Sec. 4.1 can generally only be solved numerically. However, analytical limits can be obtained for $T \to 0$ and fast poisoning rates ($\gamma \gg 1$).

In this case we can treat the quasiparticle poisoning via effective potentials U_{eff} so that the Fokker-Planck equations (4.10) simplify to

$$\partial_t \mathcal{P} = \mu \partial_\phi \left[\left(\frac{1}{2} \partial_\phi U_{\text{eff}} \right) \mathcal{P} \right]. \tag{4.17}$$

In the case of stationary solutions $\partial_t \mathcal{P} = 0$ this further simplifies to

$$\begin{aligned} \left(\frac{1}{2} \partial_\phi U_{\text{eff}} \right) \mathcal{P} &= c \\ \Rightarrow \mathcal{P} &= 2c \left(\partial_\phi U_{\text{eff}} \right)^{-1} \end{aligned} \tag{4.18}$$

where c is a constant with respect to ϕ. The voltage developing across the junction is given by eq. (4.12) so that

$$V = -\frac{eR}{\hbar}\int_0^{4\pi} d\phi\,(\partial_\phi U_{\text{eff}})\mathcal{P} = -\frac{eR}{\hbar}\int_0^{4\pi} d\phi\,2c = -\frac{eR}{\hbar}8\pi c \tag{4.19}$$

or

$$\nu = -\frac{8\pi c}{\xi}. \tag{4.20}$$

The constant c can be determined via the normalization

$$\begin{aligned} 1 &= \int_0^{4\pi} d\phi\,\mathcal{P} = 2c\int_0^{4\pi} d\phi\;(\partial_\phi U_{\text{eff}})^{-1} \\ \Rightarrow c &= \frac{1}{2}\left[\int_0^{4\pi} d\phi\;(\partial_\phi U_{\text{eff}})^{-1}\right]^{-1} \end{aligned} \tag{4.21}$$

so that the voltage drop across the junction takes the form

$$\nu = -\frac{4\pi}{\xi}\left[\int_0^{4\pi} d\phi\;(\partial_\phi U_{\text{eff}})^{-1}\right]^{-1}. \tag{4.22}$$

In the case where the poisoning electrons come from a low temperature reservoir ($k_B T_b \ll \xi$), poisoning events will always relax the junction to its instantaneous ground state. If these poisoning events are frequent enough ($\gamma \gg 1$), the junction will always be in the lower of the two potentials so that the effective potential in this case is given by [132]

$$U_{\text{eff}} = \min_p \left[U_p\right]. \tag{4.23}$$

In the opposite case where the electrons facilitating the poisoning events come from a reservoir with high temperature ($k_B T_b \gg \xi$), poisoning events can both relax and excite the junction with equal probability. If the poisoning events are again frequent ($\gamma \gg 1$), the junction will now spend an equal amount of time in

Junction Type	**Poisoning**	**Voltage**
Short	no pois.	$\nu = \sqrt{x^2 - \left(\frac{1}{2}\right)^2}$
	low temp.	
	high temp.	$\nu = x$
Long	no pois.	$\nu = 2\left[\ln\left(\frac{x+1}{x-1}\right)\right]^{-1}$
	low temp.	$\nu = \left[\ln\left(\frac{x+\frac{1}{2}}{x-\frac{1}{2}}\right)\right]^{-1}$
	high temp.	

Table 4.1: Current voltage characteristics for short and long junctions with either no poisoning ($\gamma = 0$), low temperature poisoning ($k_B T_b \ll \Delta, \gamma \gg 1$), or high temperature poisoning ($k_B T_b \gg \Delta, \gamma \gg 1$). Table adapted from the original publication [54].

both potentials so that the effective potential can be expressed as

$$U_{\text{eff}} = \frac{U_0 + U_1}{2}. \tag{4.24}$$

With these effective potentials the integral in the expression for the voltage (4.22) can be solved. The resulting voltage current characteristics for both the short and long junction limit as well as the case without poisoning are summarized in Tab. 4.1.

In a short junction the cases without poisoning ($\gamma = 0$) and low temperature poisoning ($k_B T_b \ll \Delta, \gamma \gg 1$) are indistinguishable from each other in the current voltage characteristic. Only

the high temperature poisoning case ($k_B T_b \gg \Delta$) results in a resistive junction [132]. In contrast, the current voltage characteristic for the long junction limit differs for the cases with and without poisoning. More precisely, the critical current changes by a factor of two between the two cases, an effect already predicted in [78] for low temperature poisoning. Because the current voltage characteristic does not change when going from low temperature ($k_B T_b \ll E_T$) to high temperature ($k_B T_b \gg E_T$) poisoning in the long junction, the result of [78] can be extended to the high temperature poisoning case.

4.3 Finite Junction Temperature

The analytical solutions derived in Sec. 4.2 could only be obtained in the limit of zero junction temperature $T \to 0$. To include thermal fluctuations, we need to numerically solve the Fokker-Planck equations (4.10) and the expression for the voltage (4.12) (Fig. 4.2, dots).

For bias currents above the critical current where the junction becomes resistive the current voltage characteristic is well described by the analytical limits (Fig. 4.2, solid lines) from Tab. 4.1 in the cases of no ($\gamma = 0$) and fast ($\gamma \gg 1$) poisoning. Looking at the differential equation (4.7), we see that the time derivative of the phase difference across the junction $\dot{\phi}$ at high bias currents is mostly determined by the first term including the bias current and the thermal fluctuations $\mu\zeta(t)$ become negligible. At small bias currents however these fluctuations become comparatively large and result in a *"smearing out"* of the current voltage characteristic around the critical current so that a small but finite voltage will develop across the junction even below the analytically predicted critical current. In this regime

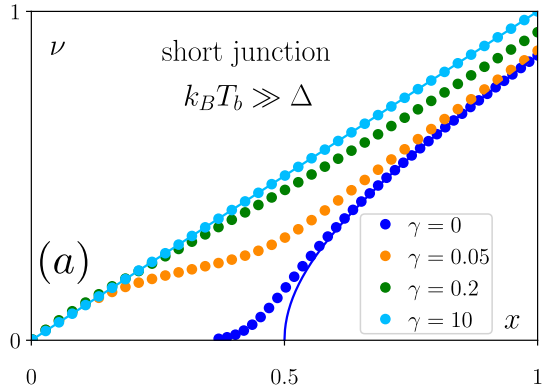
1
ν
short junction
$k_B T_b \gg \Delta$
$\gamma = 0$
$\gamma = 0.05$
$\gamma = 0.2$
$\gamma = 10$
(a)
x
0
0
0.5
1

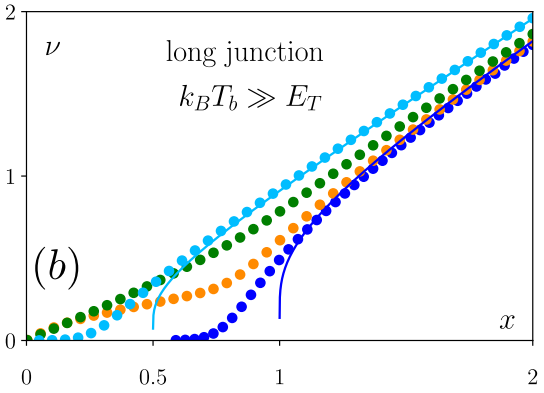
2
ν
long junction
$k_B T_b \gg E_T$
1
(b)
x
0
0
0.5
1
2

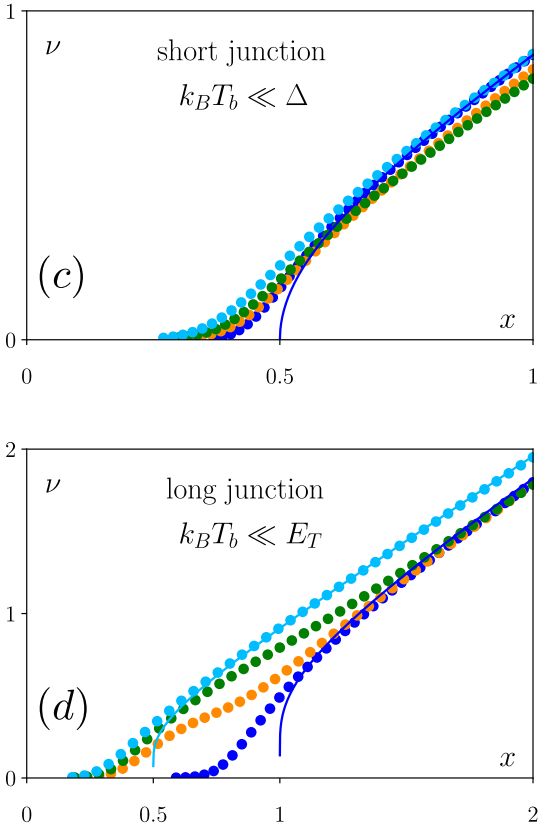

Figure 4.2: Current voltage characteristic for both short and long junctions for both high ((a) and (b)) and low ((c) and (d)) poisoning temperature at different poisoning rates γ. The dots are numerical solutions obtained by numerically solving the Fokker-Planck equations (4.10) for a finite junction temperature $k_B T = 0.03\xi$ and evaluating eq. (4.12). The solid lines are the analytical limits for $T \to 0$ and $\gamma = 0$ or $\gamma \to \infty$ taken from Tab. 4.1. Figure taken from the original publication [54].

the washboard potentials have minima at which $\partial_\phi U_p = 0$ so that because of eq. (4.7) $V \propto \dot{\phi} = 0$ after the phase ϕ has evolved into the minima (neglecting thermal fluctuations). No voltage should therefore develop across the junction. However, thermal fluctuations can randomly move the phase ϕ in both directions. At bias currents below but close to the critical current these thermal fluctuations are enough to move the phase out of the local potential minimum so that the phase can evolve further resulting in a finite voltage. This effect has already been described in nontopological junctions [134].

Intermediate poisoning rates (Fig. 4.2, orange and green) will interpolate between the two limits of no ($\gamma = 0$) and fast ($\gamma \gg 1$) poisoning if the poisoning temperature is high compared to the intrinsic energy scale of the junction $k_B T_b \gg \xi$ (Fig. 4.2, (a) and (b)). However, in the case of low poisoning temperature $k_B T_b \ll \xi$ (Fig. 4.2, (c) and (d)) an additional effect takes place at bias currents above the critical current. When starting from no poisoning ($\gamma = 0$) and increasing the poisoning rate, the voltage developing across the junction gets lowered for larger bias currents. A possible explanation of this effect can be found by looking at the corresponding washboard potentials (Fig. 4.3, (a)). In the short junction (the long junction can be explained in a similar fashion) the washboard potentials are 4π periodic. In the region $\phi \in [-\pi, \pi]$ the washboard potential for $p = 0$ first has a small slope for $\phi \in [-\pi, 0]$ and has a larger slope in the region $\phi \in [0, \pi]$. The opposite is true for the potential for $p = 1$. Because $k_B T_b \ll \Delta$, only relaxation processes are possible. For intermediate poisoning rates ($\gamma \approx 1$) the time between individual poisoning events (Fig. 4.3, black arrows) is comparable to the time it takes the junction to advance the phase ϕ by approximately 2π. Therefore, there will be approximately one poisoning event per 2π interval. Applying this logic to the interval $[-\pi, \pi]$, we can see (Fig. 4.3, (a) left) that a relaxation event happening around $\phi = 0$ will result in the junction first being evolved by

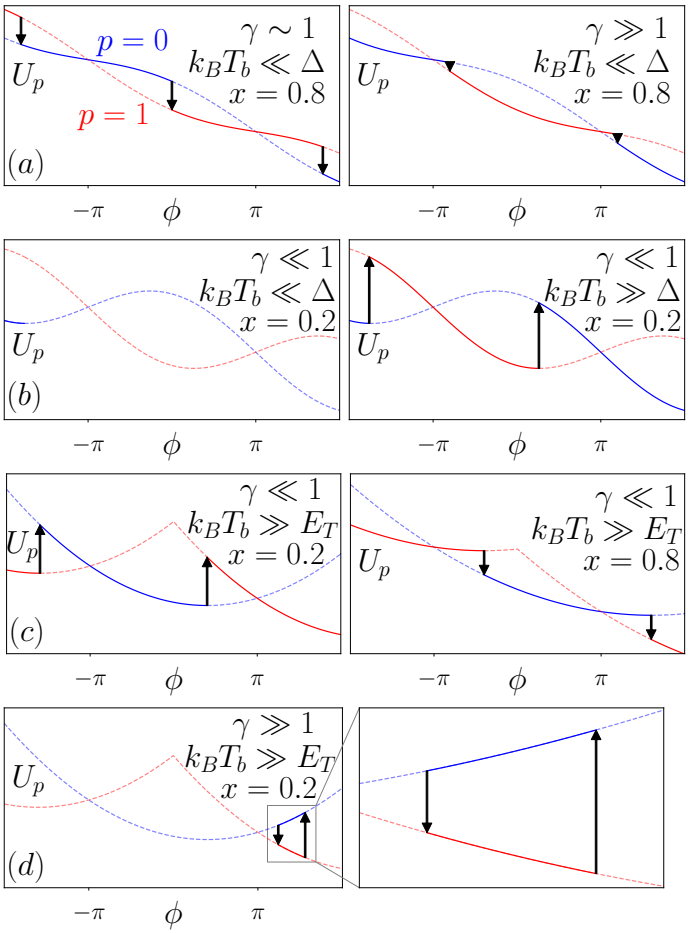

Figure 4.3: Example paths through which the short ((a) and (b)) and long ((c) and (d)) junctions can evolve. The two colors correspond to the two parities $p = 0, 1$ while the solid (dashed) lines correspond to the state the junction currently occupies (does not occupy). Black arrows indicate poisoning events which change the parity of the junction. Figure taken from the original publication [54].

the potential for $p = 0$ with a small slope and continue to be evolved by the small slope of the potential for $p = 1$ after the poisoning event. In contrast, should the poisoning be fast $\gamma \gg 1$ (Fig. 4.3, (a) right), the relaxation due to a poisoning event will happen shortly after $U_{p=1} < U_{p=0}$, which happens at $\phi = -\pi$. The junction therefore gets evolved by a steeper slope than in the case for intermediate poisoning ($\gamma \approx 1$) resulting in a higher voltage $V \propto \partial_\phi U_p$.

4.4 Zero Junction Temperature

Using the Fokker-Planck equations, we can analyze the current voltage characteristic for finite junction temperatures T. Current state of the art experiments however reach temperatures far below the superconducting gap Δ and Thouless energy E_T [46, 94]. To describe these experiments, it is therefore important to also look at the zero temperature limit. For driving currents below the critical current the Fokker-Planck equations no longer hold for low junction temperatures [135]. To analyze the zero temperature limit, we therefore employ the second method described in Sec. 4.1.2.

The resulting current voltage characteristics (Fig. 4.4) resemble those obtained via the Fokker-Planck equations (Fig. 4.2) above the critical currents. At driving currents around and below the critical currents the current voltage characteristic changes significantly when neglecting thermal fluctuations. For vanishing poisoning ($\gamma = 0$) and fast poisoning ($\gamma \gg 1$) they follow the analytical limits from Tab. 4.1 up to the critical currents and do not show the effect of *"smearing out"* like in the case for finite junction temperature. This makes the current model well suited to investigate the effects of poisoning at and below the critical

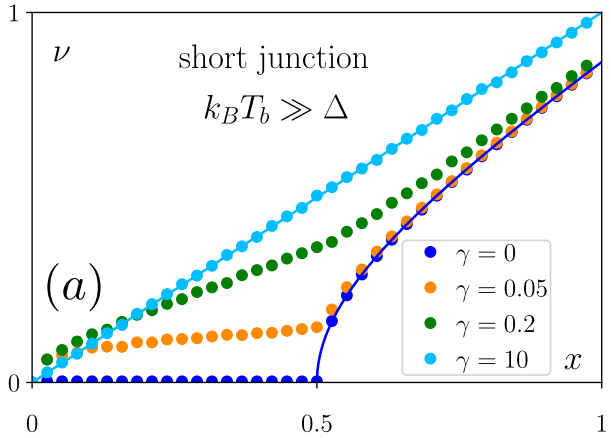
1
ν
short junction
$k_B T_b \gg \Delta$
(a)
$\gamma = 0$
$\gamma = 0.05$
$\gamma = 0.2$
$\gamma = 10$
x
0
0
0.5
1

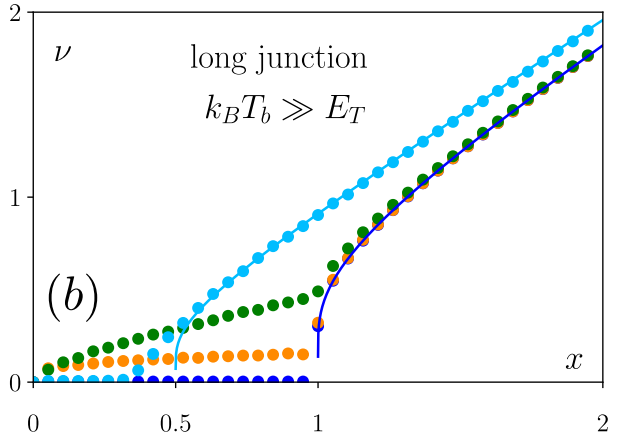
2
ν
long junction
$k_B T_b \gg E_T$
1
(b)
x
0
0
0.5
1
2

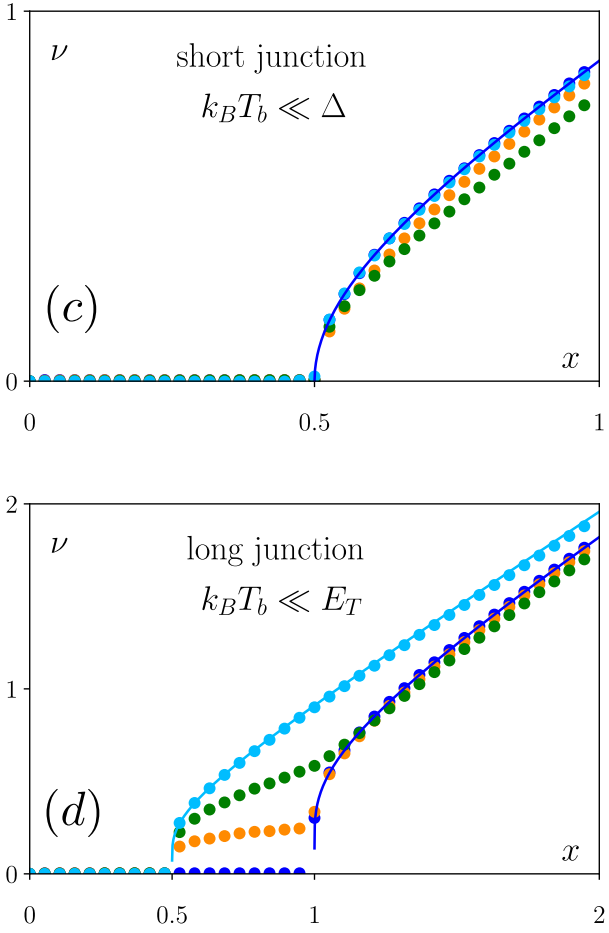

Figure 4.4: Current voltage characteristics for short and long junctions, high ($k_B T_b \gg \xi$) and low ($k_B T_b \ll \xi$) poisoning temperature, and different poisoning rates γ obtained by numerically implementing the second method described in Sec. 4.1.2 (dots). The solid lines are the analytical limits taken from Tab. 4.1. Adapted from [54].

current.

In the short junction with high poisoning temperature $k_B T_b \gg \Delta$ (Fig. 4.4, (a)) driving currents below the critical current ($x < 1/2$) result in a small but finite voltage drop across the junction due to a small poisoning rate. This finite voltage drop extends up to vanishing driving currents so that the critical current vanishes for finite poisoning rates $\gamma > 0$. In contrast to this, the critical current will stay unchanged if the temperature of the poisoning particles is small $k_B T_b \ll \Delta$ (Fig. 4.4, (c)). To understand this, we have to look at the corresponding washboard potentials (Fig. 4.3, (b)). For bias currents below the critical current the potential minimum for one parity coincides with a negative slope of the potential for the other parity. If the poisoning is slow ($\gamma \ll 1$), the junction will generally stay in one parity and evolve the phase to its corresponding potential minimum before a potential poisoning event takes place. In order for a poisoning event to change the parity of the junction, it must excite the junction to a higher energy state. When such an excitation happens, the junction then evolves the phase according to that potential of higher energy, which always has a negative slope at the time of the poisoning event. The phase will evolve to the next potential minimum at which point the process repeats itself. Because each poisoning event advances the phase of the junction by 2π, a small but finite average voltage will develop across the junction. Because the poisoning events need to excite the junction to a higher energy state in order for this process to occur, the particles facilitating the poisoning event must come from a bath of high temperature ($k_B T_b \gg \Delta$) where higher energy states are occupied in order to ensure energy conservation. A finite voltage therefore only develops in the case of high poisoning temperature ($k_B T_b \gg \Delta$) while no voltage develops when the temperature of the poisoning particles is small ($k_B T_b \ll \Delta$).

Similarly, in the long junction limit with high poisoning temperature $k_B T_b \gg E_T$ (Fig. 4.4, (b)) small and finite poisoning

($\gamma > 0$) again results in a finite voltage below the critical current. However, in contrast to the short junction limit, the same thing happens for driving currents $1/2 < x < 1$ in the case where the poisoning particles come from a bath with low temperature $k_B T_b \ll E_T$ (Fig. 4.4, (d)). Looking at the corresponding washboard potentials (Fig. 4.3, (c)), we note that the potential minimum of the potential of one parity always coincides with a negative slope of the potential of the other parity, like in the short junction. However, the cases $x < 1/2$ and $1/2 < x < 1$ differ in the energy spectrum of the two potentials. For $x < 1/2$ the potential minimum of one potential always lies energetically below the other potential so that poisoning events must excite the junction in order to change the parity. For $1/2 < x < 1$ the potential minima always lie energetically above the other potential so that changes in parity coincide with a relaxation of the junction. Because excitations require a high bath temperature of the poisoning particles ($k_B T_b \gg E_T$), a finite voltage for driving currents $x < 1/2$ only occurs in the case of high temperature poisoning. Meanwhile, relaxation processes are always possible so that a finite voltage due to poisoning develops for driving currents $1/2 < x < 1$ regardless of the temperature of the poisoning particles.

Like in short junctions, the critical current vanishes for intermediate poisoning rates ($\gamma \sim 1$) and high poisoning temperatures ($k_B T_b \gg E_T$). However, unlike in the short junction case, a finite critical current at half the original value ($x = 1/2$) reemerges when going to the fast poisoning regime ($\gamma \gg 1$). To see how the voltage drop for low driving currents $x < 1/2$ vanishes, we take a look at the corresponding washboard potentials (Fig. 4.3, (d)). The phase difference across the junction ϕ evolves to a position where the slopes of the potentials of both parities differ only by their signs. As poisoning events are much faster than the junction can evolve the phase in a given potential ($\gamma \gg 1$), the phase can never evolve away from this point and will only

ever make small movements in both directions. This will result in noise in the voltage signal which vanishes when averaged over larger times.

When going from the case of no poisoning ($\gamma = 0$) to the case of fast poisoning ($\gamma \gg 1$) in the long junction, the critical current changes from $x = 1$ to half its original value $x = 1/2$. This effect has been predicted for low poisoning temperatures [78]. As we have seen, this effect should also occur should the poisoning particles come from a high temperature bath. Furthermore, this effect can only be used as an indicator for the junction parity if the quasiparticle poisoning rate is sufficiently small, as even small poisoning rates will result in finite voltages developing across the junction for driving currents $x < 1$.

4.5 Poisoning Rates

In the preceding sections we have seen how changing the poisoning rates can have an impact on the resulting current voltage characteristics on Josephson junctions. These effects can also be used to directly measure the poisoning rates.

One way to measure the poisoning rate is possible in long junctions where the poisoning is fast ($\gamma \gg 1$) and coming from a high temperature bath ($k_B T_b \gg E_T$). At driving currents $x < 1/2$ the voltage developing across the junction vanishes due to the junction changing its parity rapidly back and forth (Fig. 4.3, (d)) so that the phase ϕ gets trapped at a fixed point. Because the two potentials corresponding to the two parities have opposite slopes, the voltage $V \propto \dot{\phi} \propto \partial_\phi U_p$ also jumps between two values which only differ in their sign. To determine the exact value of the voltages, we first have to find the phase ϕ at which this trapping of the phase occurs. The slopes of the two potentials

will be opposite if

$$\begin{aligned}
&\partial_\phi U_0 = -\partial_\phi U_1 \\
\Rightarrow &\partial_\phi \left[E_0(\phi) - \frac{\hbar I}{e}\phi \right] = -\partial_\phi \left[E_1(\phi) - \frac{\hbar I}{e}\phi \right] \\
\Rightarrow &\partial_\phi [E_0(\phi)] - \frac{\hbar I}{e} = -\partial_\phi [E_1(\phi)] + \frac{\hbar I}{e} \\
\Rightarrow &I_0(\phi) - I = -I_1(\phi) + I \\
\Rightarrow &\frac{I_0(\phi) + I_1(\phi)}{2} = I
\end{aligned} \tag{4.25}$$

meaning that the average current of the two parities must therefore equal the driving current. As this average always vanishes in short junctions due to the currents of the two parities differing only in their sign, this effect never happens in such junctions. In long junctions however this occurs at the phases

$$\phi = 2\pi \left(x + \frac{1}{2} \right) + 2\pi n, \qquad n \in \mathbb{Z}. \tag{4.26}$$

The voltage developing across the junction at this point in parity $p = 0$ is given by

$$\begin{aligned}
V = \frac{\hbar}{2e}\dot{\phi} &= -\frac{\hbar\mu}{4e}\partial_\phi U_0 = -\frac{\hbar^2\mu}{4e^2}(I_0(\phi) - I) = -R(I_0(\phi) - I) \\
&= -R\left[\frac{I_c}{2\pi} 2\pi \left(x + \frac{1}{2} \right) - I \right] = -R\left[I + \frac{1}{2}I_c - I \right] \\
&= -\frac{1}{2}RI_c.
\end{aligned} \tag{4.27}$$

Similarly, the voltage developing in parity $p = 1$ is given by

$$V = \frac{1}{2}RI_c \tag{4.28}$$

so that the voltage constantly jumps between the values $V = \pm RI_c/2 = \pm eRE_T/(2\hbar)$ ($\nu = \pm 1/2$) when changing from one

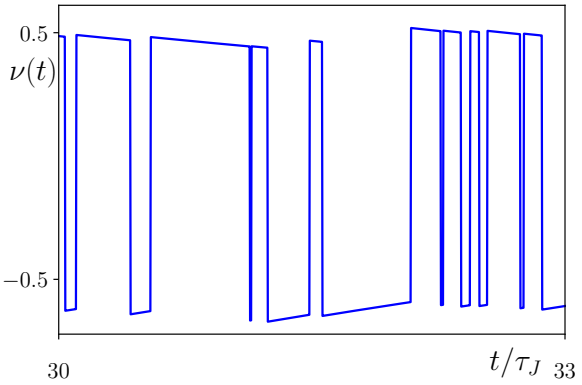

Figure 4.5: Time-dependent voltage signal of a long junction with fast poisoning $\gamma \gg 1$ and high poisoning temperature ($k_B T_b \gg E_T$) obtained by numerically implementing the second method described in Sec. 4.1.2. Figure taken from the original publication [54].

parity to the other (Fig. 4.5). By recording the time-dependent voltage signal one can count the number of times the voltage signal changes its sign in a fixed time frame and deduce the poisoning rate.

In case the poisoning is slow ($\gamma \ll 1$), this first scheme cannot be used to measure the poisoning rate. However, in this regime the poisoning rate can be obtained through another method as long as the junction is not in the short junction limit with low poisoning temperature ($k_B T_b \ll \Delta$). To see this we look at a long junction where the poisoning particles come from a bath with low temperature $k_B T_b \ll E_T$ (the high poisoning temperature cases $k_B T_b \gg E_T$ can be explained in a similar fashion). For driving currents $1/2 < x < 1$ slow poisoning ($\gamma \ll 1$) develops a small but finite voltage across the junction. Because the poisoning is slow, the junction will stay in one parity and evolve its phase to the minimum of the corresponding washboard potential before a poisoning event takes place and changes the parity of the junction (Fig. 4.3, (c)). After the poisoning event changed the parity of the junction, the phase will again be advanced to the next potential minimum. The phase difference between two potential minima is always 2π and most notably independent of the driving current. Because the poisoning is slow, we can assume that the phase will always evolve to a potential minimum before a poisoning event changes the parity of the junction so that each poisoning event corresponds to the phase being advanced by 2π. The time-dependent voltage signal will therefore feature voltage pulses right after a poisoning event with a vanishing voltage drop between the pulses when the phase stays in a potential minimum waiting for a poisoning event to occur. By recording the time-dependent voltage signal in a fixed time frame one can again deduce the rate with which these poisoning events occur. Furthermore, because the voltage pulses all have the same sign, they add up to a finite time averaged voltage $V = \hbar 2\pi\Gamma/(2e)$ ($\nu = 2\pi\gamma$) developing across the junction (Fig. 4.6) which can

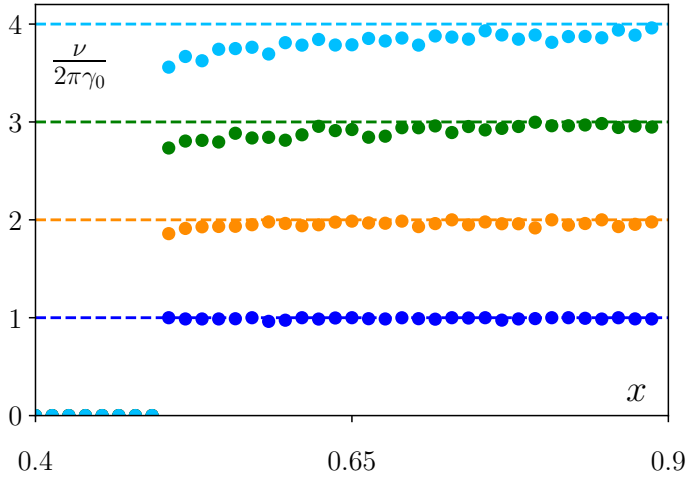

Figure 4.6: Time averaged voltage of a long junction with slow poisoning ($\gamma/\gamma_0 = 1, 2, 3, 4$ with $\gamma_0 = 10^{-3}$ from bottom to top) and low poisoning temperature ($k_B T_b \ll E_T$) obtained by numerically implementing the second method described in Sec. 4.1.2. Figure taken from the original publication [54]. ©2020 American Physical Society

also be used to measure the poisoning rate.

These two methods to measure the poisoning rate both require the poisoning to either be fast ($\gamma \gg 1$) or slow ($\gamma \ll 1$). However, there exists an experimental scheme (Fig. 4.7) in which the intermediate regime ($\gamma \sim 1$) can potentially be tuned into the fast poisoning regime. By shunting the Josephson junction with an external resistance R_{ext}, we can again produce an RSJ model with the effective resistance R_{tot} given by Kirchhoff's rule $R_{\text{tot}}^{-1} = R^{-1} + R_{\text{ext}}^{-1}$, which in the case of small external resistances $R_{\text{ext}} \ll R$ simplifies to $R_{\text{tot}} \approx R_{\text{ext}}$. Because the intrinsic time scale of the junction is inversely proportional to the resis-

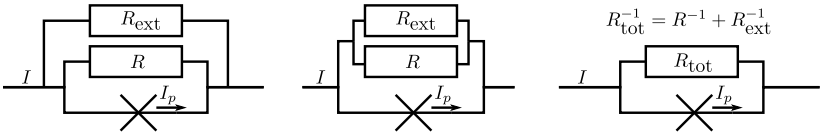

Figure 4.7: Three equivalent circuits where an external resistance R_{ext} shunts the Josephson junction. The shunted circuit (left) is equivalent with an RSJ model (right) with a modified resistance R_{tot}. Figure taken from the original publication [54]. ©2020 American Physical Society

tance of the RSJ model $\tau_J \propto R_{\mathrm{tot}}^{-1}$, we can increase this time scale τ_J by shunting the junction with small resistances. As the dimensionless poisoning rate $\gamma = \Gamma\tau_J$ increases with longer intrinsic time scales of the junction, the junction can be tuned from the slow or intermediate poisoning regime to the fast poisoning regime. The poisoning rates with different resistances scale like $\gamma/\gamma' = R_{\mathrm{tot}}/R'_{\mathrm{tot}}$. The intrinsic poisoning, for example, occurs on a time scale $\tau_{qp} \sim 1\,\mu$s while $\tau_J \sim 10$ ps for typical junctions so that intrinsic quasiparticle poisoning $\gamma \sim 10^{-5}$ should always be slow. When the intrinsic resistance is on the order of $R \sim 100\,\Omega$, the intrinsic quasiparticle poisoning can be tuned into the intermediate regime ($\gamma \sim 1$) by applying an external resistance of $R_{\mathrm{ext}} \sim 1$ mΩ. Similarly, to achieve the fast poisoning regime $\gamma \sim 10$ used in numerical calculations an external resistance of $R_{\mathrm{ext}} \sim 0.1$ mΩ would be necessary. However, as the effective resistance is always going to be smaller than the intrinsic resistance $R_{\mathrm{tot}} < R$, we can only ever increase the dimensionless poisoning rate γ by shunting the Josephson junction with a resistance.

4.6 Extended Josephson Junction

In the previous sections we have focused on Josephson junctions that are mediated by a single helical edge state. However, signatures of topology have been found in extended junctions where the Josephson current is carried by two sets of spin-helical edge states from opposite edges of a quantum spin Hall insulator [129, 132, 137–140]. We furthermore consider a constriction in the topological edge states [141] such that electrons from one edge can tunnel into the other edge (Fig. 4.8). The energy phase relation of the extended junction is given by[3]

$$E_{p_1,p_2}(\phi) = \frac{E_{p_1}(\phi) + E_{p_2}(\phi + \Phi)}{2} \tag{4.29}$$

where $E_{p_i}(\phi)$ is the energy phase relation of a single edge and p_i is the parity of the junction mediated by edge $i = 1, 2$. A flux Φ is threaded between the superconductors so that an additional phase difference exists between the two edges. Poisoning events described by the rates Γ_i can occur in both edges independently and change the parity $p_i \to p_i + 1 \mod 2$ of the corresponding edge while leaving the other parity $p_{i'}$ unchanged. In contrast to this, the tunneling of electrons between the two edges described by the rate Γ_c changes both parities $p_1 \to p_1 + 1 \mod 2$ and $p_2 \to p_2 + 1 \mod 2$ while leaving the total parity of the junction $p_1 + p_2$ unchanged.

[3] An additional factor of $1/2$ has been introduced in order to better compare the results from the extended junction to a junction mediated by a single edge.

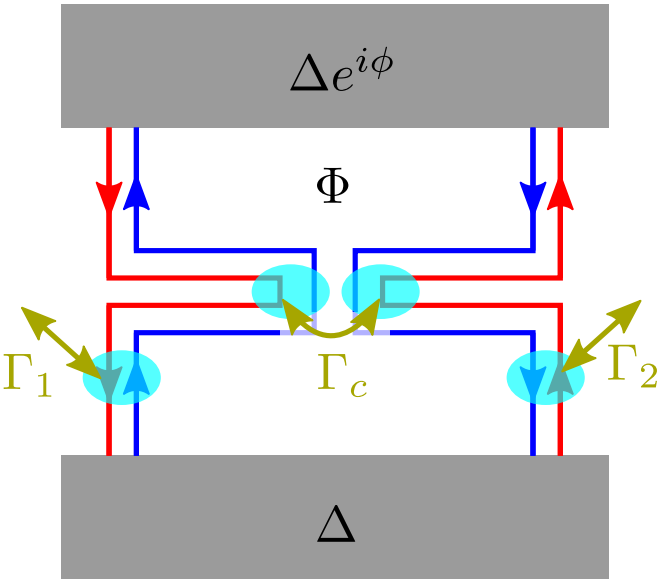

Figure 4.8: Josephson junction mediated by two sets of spin-helical edge states. Quasiparticle poisoning in both edges Γ_i can change the overall parity of the junction. Furthermore, electrons can tunnel between the two edges Γ_c which leaves the overall parity of the junction unchanged. A flux Φ is threaded between the two superconductors. Figure taken from the original publication [54].

4.6.1 Tunneling Rate

The tunneling from one helical edge into the other can be described with Fermi's golden rule

$$W_c = \frac{2\pi}{\hbar} \sum_{if} |\langle f|H_T|i\rangle|^2 \, \delta[\varepsilon_i - \varepsilon_f] \tag{4.30}$$

where

$$|i\rangle = |p_1\rangle \otimes |p_2\rangle \qquad \text{and} \qquad |f\rangle = |p_1'\rangle \otimes |p_2'\rangle \tag{4.31}$$

are the initial and final states of the two edges with $p_{1,2}$ being the parity of the two edges. The tunneling Hamiltonian H_T transfers an electron from one edge to the other so that the parities of both edges of the final state change

$$p_{1,2}' = p_{1,2} + 1 \mod 2. \tag{4.32}$$

Converting the sum into integrals yields

$$W_c = \frac{2\pi}{\hbar} \int d\varepsilon_{p_1} \rho_{p_1} \, d\varepsilon_{p_2} \rho_{p_2} \, d\varepsilon_{p_1'} \rho_{p_1'} \, d\varepsilon_{p_2'} \rho_{p_2'} \, |\langle f|H_T|i\rangle|^2 \, \delta[(\varepsilon_{p_1} + \varepsilon_{p_2}) - (\varepsilon_{p_1'} + \varepsilon_{p_2'})] \tag{4.33}$$

where ρ_α is the spectral density of the states $\alpha = p_1, p_2, p_1', p_2'$. In a completely isolated system (with no poisoning) the spectral density of the Andreev bound states would be a delta function. However, due to coupling to the environment, the spectral density will be broadened, for instance, through thermal broadening or poisoning events and we assume the spectral density to have the form of a Lorentz-Cauchy distribution

$$\rho_\alpha = \frac{1}{\pi} \frac{\gamma_\alpha}{(\varepsilon_\alpha - E_\alpha)^2 + \gamma_\alpha^2} =: L[\varepsilon_\alpha - E_\alpha, \gamma_\alpha] \tag{4.34}$$

with a full width at half maximum (FWHM) of $2\gamma_\alpha$ around the unperturbed energy E_α. When the matrix element of the tunneling Hamiltonian has a negligible energy dependence the tunneling rate simplifies to

$$W_c = \frac{2\pi}{\hbar} |\langle f|H_T|i\rangle|^2 \int d\varepsilon_{p_1}\rho_{p_1}\, d\varepsilon_{p_2}\rho_{p_2}\, d\varepsilon_{p_1'}\rho_{p_1'}\, d\varepsilon_{p_2'}\rho_{p_2'} \delta[(\varepsilon_{p_1}+\varepsilon_{p_2}) - (\varepsilon_{p_1'}+\varepsilon_{p_2'})]. \tag{4.35}$$

Substituting the spectral densities and performing the integral over the energy $\varepsilon_{p_2'}$ yields

$$\begin{aligned}\kappa :=& \int d\varepsilon_{p_1} d\varepsilon_{p_2} d\varepsilon_{p_1'} d\varepsilon_{p_2'} L[\varepsilon_{p_1} - E_{p_1}, \gamma_{p_1}] L[\varepsilon_{p_2} - E_{p_2}, \gamma_{p_2}] \\ & L[\varepsilon_{p_1'} - E_{p_1'}, \gamma_{p_1'}] L[\varepsilon_{p_2'} - E_{p_2'}, \gamma_{p_2'}] \delta[(\varepsilon_{p_1}+\varepsilon_{p_2}) - (\varepsilon_{p_1'}+\varepsilon_{p_2'})] \\ =& \int d\varepsilon_{p_1} d\varepsilon_{p_2} d\varepsilon_{p_1'} L[\varepsilon_{p_1} - E_{p_1}, \gamma_{p_1}] L[\varepsilon_{p_2} - E_{p_2}, \gamma_{p_2}] \\ & L[\varepsilon_{p_1'} - E_{p_1'}, \gamma_{p_1'}] L[\varepsilon_{p_1} + \varepsilon_{p_2} - \varepsilon_{p_1'} - E_{p_2'}, \gamma_{p_2'}].\end{aligned} \tag{4.36}$$

Noting that the integral over two Lorentz-Cauchy distributions is again a Lorentz-Cauchy distribution (see App. B)

$$\int d\varepsilon L[\varepsilon + a, \gamma] L[\varepsilon + b, \delta] = L[a - b, \gamma + \delta] \tag{4.37}$$

and that it is symmetric in its first argument $L[\varepsilon, \gamma] = L[-\varepsilon, \gamma]$, we can perform the remaining integrals over $\varepsilon_{p_1'}, \varepsilon_{p_2}$, and ε_{p_1} in

that order

$$\begin{aligned}
\kappa &= \int d\varepsilon_{p_1} d\varepsilon_{p_2} L[\varepsilon_{p_1} - E_{p_1}, \gamma_{p_1}] L[\varepsilon_{p_2} - E_{p_2}, \gamma_{p_2}] \\
&\qquad\qquad L[\varepsilon_{p_1} + \varepsilon_{p_2} - E_{p_1'} - E_{p_2'}, \gamma_{p_1'} + \gamma_{p_2'}] \\
&= \int d\varepsilon_{p_1} L[\varepsilon_{p_1} - E_{p_1}, \gamma_{p_1}] \\
&\qquad\qquad L[-\varepsilon_{p_1} + E_{p_1'} + E_{p_2'} - E_{p_2}, \gamma_{p_2} + \gamma_{p_1'} + \gamma_{p_2'}] \\
&= L[-E_{p_1} + E_{p_1'} + E_{p_2'} - E_{p_2}, \gamma_{p_1} + \gamma_{p_2} + \gamma_{p_1'} + \gamma_{p_2'}] \\
&= L[(E_{p_1'} + E_{p_2'}) - (E_{p_1} + E_{p_2}), D/2] \\
&= L[E_{p_1', p_2'} - E_{p_1, p_2}, D/2]
\end{aligned} \tag{4.38}$$

where we have defined $D/2 = \gamma_{p_1} + \gamma_{p_2} + \gamma_{p_1'} + \gamma_{p_2'}$ for the total broadening[4]. Abbreviating the matrix element $|t_c| = \langle f|H_T|i\rangle$ and defining the dimensionless broadening $d = D/E_T$ the tunneling rate therefore takes the form

$$\begin{aligned}
W_c &= \frac{2\pi}{\hbar} |t_c|^2 \frac{1}{\pi} \frac{\frac{D}{2}}{(E_{p_1', p_2'} - E_{p_1, p_2})^2 + \left(\frac{D}{2}\right)^2} \\
&= \frac{2\pi}{\hbar} |t_c|^2 \frac{1}{\pi} \frac{1}{E_T} \frac{\frac{d}{2}}{\left(\frac{E_{p_1', p_2'} - E_{p_1, p_2}}{E_T}\right)^2 + \left(\frac{d}{2}\right)^2} \\
&= \frac{2\pi}{\hbar} |t_c|^2 \frac{1}{\pi} \frac{1}{E_T} \frac{2}{d} \frac{\left(\frac{d}{2}\right)^2}{\left(\frac{E_{p_1', p_2'} - E_{p_1, p_2}}{E_T}\right)^2 + \left(\frac{d}{2}\right)^2} \\
&= \frac{\Gamma_c}{d} \frac{\left(\frac{d}{2}\right)^2}{\left(\frac{E_{p_1', p_2'} - E_{p_1, p_2}}{E_T}\right)^2 + \left(\frac{d}{2}\right)^2}
\end{aligned} \tag{4.39}$$

[4] We have also neglected a factor of 2 in the energy argument of the final Lorentz-Cauchy distribution so that our notation is consistent with the added factor of 1/2 in the definition (4.29).

where

$$\Gamma_c = \frac{2\pi}{\hbar} |t_c|^2 \frac{2}{\pi E_T}. \tag{4.40}$$

The tunneling rate W_c has the form of a Lorentz-Cauchy distribution with a FWHM of d centered around zero energy and has a maximum value of Γ_c/d.

4.6.2 Two Critical Currents

With the tunneling rates evaluated we can adapt the second method described in Sec. 4.1.2 and include the tunneling events in analogy to the poisoning events. Numerically implementing this method results in the current voltage characteristic shown in Fig. 4.9 (top).

Including the tunneling events only adds a voltage peak around $x = 1/2$ and leaves the current voltage characteristic unchanged for driving currents away from $x \approx 1/2$. Depending on the flux Φ that gets threaded between the two superconductors, we can make out two *"critical currents"* just like in short junctions [132]. For instance, looking at the specific case of vanishing flux $\Phi = 0$, there exists a critical current at $x \approx 1/2$ at which a finite voltage develops across the junction. However, a second *"critical current"* exists around $x \approx 1$ at which point the current voltage characteristic shows a kink where the voltage increases more rapidly than below $x \approx 1$.

To understand this we need to look at the possible parity states the junction can be in. The junction can be in one of four states described by the vector $\boldsymbol{p} = (p_1, p_2)$ where $p_i = 0, 1$ are the parities of the two edges. The two even states $(0, 0)$ and $(1, 1)$ feature a 4π periodic energy phase relation with a critical current of $x = 1$. The overall odd states $(1, 0)$ and $(0, 1)$ however feature a 2π periodic energy phase relation and have a critical current of half that value $x = 1/2$ [79]. For bias currents $1/2 < x < 1$ the

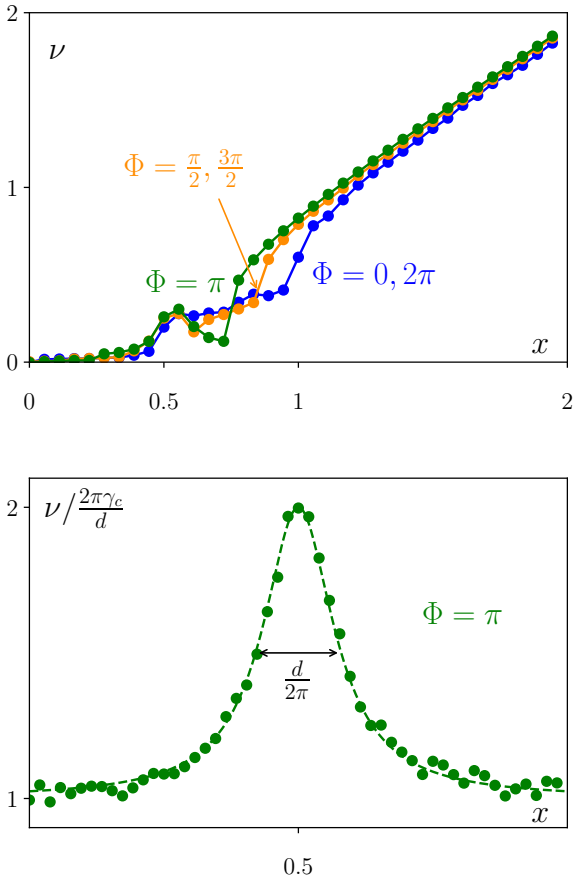

Figure 4.9: Current voltage characteristic for a long extended junction obtained by numerically implementing the second method described in Sec. 4.1.2. The poisoning rates are equal in both edges and equal to $\gamma_1 = \gamma_2 = 10^{-2}$ (10^{-4}) while the tunneling occurs at a rate of $\gamma_c = \Gamma_c \tau_J = 0.1$ (10^{-5}) at the top (bottom). The dashed line (bottom) is the analytically predicted value (4.49). Figure taken from the original publication [54].

extended junction can therefore be either in a resistive state when the overall parity of the junction is odd, or in a nonresistive state when the overall parity is even. The voltage developing across the junction in the resistive states can be evaluated similarly to the voltages from Tab. 4.1 and is given by

$$\nu_o = \left[\ln \left(\frac{x + \frac{1}{2}}{x - \frac{1}{2}} \right) \right]^{-1}. \tag{4.41}$$

As the junction can freely move between the overall even and odd states due to quasiparticle poisoning in both edges, the junction will spend some time in the resistive states and some time in the nonresistive states. When we denote the time spend in a resistive state as τ_o, the average voltage developing for bias currents $1/2 < x < 1$ can be expressed as

$$\nu = \tau_o \nu_o. \tag{4.42}$$

When driving the junction with a current $x > 1$, the overall even states also become resistive. The average voltage developing across the junction will therefore increase significantly resulting in the kink in the current voltage characteristic at $x \approx 1$.

4.6.3 Voltage Peak due to Tunneling

The emergence of two *"critical currents"* described above is independent of the tunneling between the two edges. Including tunneling events leaves the current voltage characteristic unchanged for bias currents away from $x \approx 1/2$ and only adds a voltage peak around $x = 1/2$. This voltage peak is independent of the threaded flux Φ (Fig. 4.9, top). However, for fluxes $\Phi = 0$ and $\Phi = 2\pi$ the finite voltage drop for driving currents $x > 1/2$ discussed above overshadows this peak. As tunneling events need to preserve energy conservation, such events can only occur at

phases where the washboard potentials U_{00} and U_{11} or the potentials U_{10} and U_{01} cross. Because the washboard potentials of the overall odd states are equivalent to the overall even states when shifting the flux by 2π so that $\Phi \to \Phi + 2\pi$, we can focus on the overall even junctions without loss of generality.

The two potentials U_{00} and U_{11} cross at the two phases

$$\phi_{c1} = \pi - \Phi/2, \qquad \phi_{c2} = 3\pi - \Phi/2. \tag{4.43}$$

In order for the junction to switch from the state $(0,0)$ to $(1,1)$, a tunneling event must occur at either of these two phases. In the case of small tunneling rates ($\gamma_c = \Gamma_c \tau_J \ll 1$) the junction will evolve the phase to a potential minimum before a potential tunneling event can take place. Therefore, in order for tunneling events to take place, the minimum of one potential must coincide with one of the two phases (4.43) at which the potentials cross. The potential minimum of U_{00} is located at

$$\phi_{\min} = 2\pi x - \Phi/2 \tag{4.44}$$

so that the phase difference between the minimum and the first crossing point

$$\phi_{\min} - \phi_{c1} = \pi(2x - 1) \tag{4.45}$$

is independent of the flux Φ and vanishes for a driving current $x = 1/2$. The potential minimum of the potential U_{11}

$$\phi'_{\min} = 2\pi x - \Phi/2 + 2\pi \tag{4.46}$$

is located exactly 2π away from the minimum of the potential U_{00} so that the phase difference between this minimum and the second crossing point

$$\phi'_{\min} - \phi_{c2} = \pi(2x - 1) \tag{4.47}$$

is again independent of the flux Φ and vanishes at $x = 1/2$.

When we drive the junction with a current $x = 1/2$, the crossing points of the two potentials U_{00} and U_{11} therefore always coincide with the potential minima of the two potentials. For slow tunneling ($\gamma_c \ll 1$) the junction will therefore evolve the phase to a potential minimum where the junction is going to stay until a tunneling event occurs. Because the potential minimum coincides with a crossing point of the two potentials, the tunneling event can take place and switch the junction to the other overall even state. The junction will then evolve the phase to the potential minimum of the second even state, which always lies exactly 2π apart from the potential minimum of the first potential. At this point the process can repeat itself so that the phase ϕ can slowly diffuse down the two washboard potentials. Because each tunneling event advances the phase by exactly 2π and the tunneling events occur with a frequency of Γ_c/d, the voltage developing due to tunneling is equal to $\nu = 2\pi\gamma_c/d$.

If the driving current is close to but not equal to $x = 1/2$, the phase difference between the crossing points and minima of the potentials will be finite which results in an energy difference of $\approx E_T\pi(2x-1)$ between the two potentials at the potential minima. In isolated systems where the spectral density is proportional to a delta distribution no tunneling events could occur and no additional voltage would develop across the junction due to tunneling. However, when coupling to the environment, this delta distribution gets broadened (see Sec. 4.6.1) so that tunneling events can still take place at a smaller rate. The voltage drop across the junction due to tunneling will therefore have the form

$$\nu_{\mathrm{tun}} = 2\pi\frac{\gamma_c}{d}\frac{\left(\frac{d}{4\pi}\right)^2}{\left(x-\frac{1}{2}\right)^2+\left(\frac{d}{4\pi}\right)^2} \tag{4.48}$$

which again has the form of a Lorentz-Cauchy distribution coming from the spectral density with a FWHM of $d/(2\pi)$ and maximum voltage of $\nu = 2\pi\gamma_c/d$ centered around the driving current $x = 1/2$.

As the poisoning events in each individual edge can also develop a voltage drop of $\nu_{\rm pois} = 2\pi\gamma_1$ (see Sec. 4.4) and because these two effects are independent of each other, the overall voltage developing is given by (Fig. 4.9, bottom)

$$\nu = \nu_{\rm tun} + \nu_{\rm pois} = 2\pi\frac{\gamma_c}{d}\frac{\left(\frac{d}{4\pi}\right)^2}{\left(x-\frac{1}{2}\right)^2+\left(\frac{d}{4\pi}\right)^2} + 2\pi\gamma_1. \qquad (4.49)$$

In order to measure this voltage peak, we need to tune the flux Φ away from $\Phi = 0$ and $\Phi = 2\pi$ as the finite voltage developing due to two of the four parity states of the junction being resistive would overshadow this voltage peak.

4.7 Conclusion

In this chapter we have analyzed the effects that quasiparticle poisoning has on the dynamics of fractional Josephson junctions in both the long and short junction regimes. We described the dynamics of such junctions via an RSJ model and used two methods to model the parity changing quasiparticle poisoning. First, we have rewritten the differential equation describing the RSJ model in the form of Fokker-Planck equations modeling the junction at low but finite junction temperature and included poisoning in the form of Fermi's golden rule rates [132]. We assume the poisoning particles to come from a bath of temperature T_b, which can generally differ from the junction temperature. However, similar results should occur if a nonequilibrium distribution of the quasiparticles facilitating the parity changes is assumed as long as they lie at energies $\sim k_B T_b$. To describe Josephson junctions at zero temperature, we developed a second method to obtain the current voltage characteristics by iteratively solving the differen-

tial equations of the RSJ model for small time intervals during which the parity of the junction stays fixed.

We have seen that the halving of the critical current in long junctions when going from topological to nontopological junctions as predicted by [78] for low poisoning temperatures can also be extended to the high poisoning temperature case. We have furthermore devised schemes to measure the poisoning rate in long junctions either by a time-resolved voltage measurement in the case of fast poisoning, or a time-averaged voltage measurement for slow poisoning. As the poisoning rate plays an important role in the stability of topological qubits [2, 81, 113, 142, 143] formed out of Majorana excitations [23, 29–31, 40, 144], knowledge of these poisoning rates is of great interest.

Finally, we have considered extended long junctions where two sets of spin-helical edge states mediate the Josephson effect and an additional flux is threaded between the two superconductors similar to [132]. We furthermore considered a constriction in the two sets of edge states such that electrons can tunnel from one edge to the other. The tunneling of electrons between the edges results in a voltage peak at bias currents of one half of the critical current with a height proportional to the tunneling rate. The width of the peak is bounded from below by the sum of the poisoning rates of all four parity states. This voltage peak adds another way in which fractional Josephson junctions can be characterized.

In future works it would be interesting to also include a time-periodic part in the driving current in order to study the formation of Shapiro steps and the effect that quasiparticle poisoning has on the emergence and disappearance of odd Shapiro steps. Also, considering nonequilibrium distributions of poisoning particles as well as bias voltages between superconductors and the bath the quasiparticles come from could offer new insights into the dynamics of fractional Josephson junctions.

5

Effective Lengths of Josephson Junctions

In the previous chapter we have discussed in detail the effects that quasiparticle poisoning has on the current phase relation of fractional Josephson junctions. Specifically, we have devised schemes in which the poisoning rate can be obtained through a voltage measurement. Often times these measurements relied on the junction being in the long junction regime, that is the regime in which the distance L between the two superconductors is large compared to the superconducting coherence length ξ. In

this chapter we turn our focus to this constraint and propose possible schemes in which junctions that are physically in the short junction regime can be tuned to resemble larger junctions.

Fractional Josephson junctions that are currently fabricated typically have lengths of $L \sim 100 - 500$ nm [46, 103, 105, 129]. The superconducting gap of the host superconductor is usually around $\Delta \sim 1$ meV so that considering typical Fermi velocities $v_F \sim 10^5$ m/s results in typical superconducting coherence lengths of $\xi = \hbar v_F/\Delta \sim 65$ nm. Therefore, the abovementioned junctions should lie in the long junction limit. However, because the superconductivity is induced through the proximity effect, the induced superconducting gap is generally lower than the gap of the host superconductor. When this induced superconducting gap is on the order of one magnitude smaller than the gap of the host superconductor, the resulting superconducting coherence length would be $\xi \sim 650$ nm. In this case the abovementioned junctions would lie in the short to intermediate junction regime. In these short junctions, many of the measurements proposed in Chap. 3 would become inaccessible.

To overcome this problem, we propose a scheme in which we couple the helical edge states facilitating the fractional Josephson effect to an additional spin-degenerate channel or to a spin-degenerate quantum dot. Due to this coupling, the energy phase relation of the Josephson junction will be altered in a way that is dependent on the chemical potential of the channel or on the quantum dot level energy. The key observation is that the altered energy phase relation resembles that of a Josephson junction which has a longer distance between the two superconductors L_{eff} than the actual physical distance L. An intuitive way to understand this increase in effective junction length is to consider the Fermi velocity under such a coupling. It has been shown [145] that the Fermi velocity decreases by such a coupling in a way that is dependent on the chemical potential. Because $\xi \propto v_F$, the system behaves like a system with a lowered superconducting

coherence length, which in turn can be interpreted as a longer effective junction length. By tuning the chemical potential or the quantum dot level energy, we can then tune the effective length L_{eff} of the junction.

In a related setup Vinkler-Aviv *et al.* [37] considered a single spin impurity coupled to the helical edge states facilitating a fractional Josephson effect. In this setup the periodicity of the Josephson effect became 8π periodic and the junction hosted $\mathbb{Z}_4$ parafermions instead of Majorana excitations. However, the coupling to a spin impurity considered by Vinkler-Aviv *et al.* is a very different physical process from the one considered in this chapter such that the results obtained here will differ quite significantly.

We start by reviewing Andreev reflections and their resulting Andreev bound states in Sec. 5.1. Noting that the slope of the energy phase relation at zero energy is significantly different for long and short junctions, we derive a general expression for the slope at zero energy. In Sec. 5.2 we propose a first scheme in which the effective junction length can be increased by coupling the spin-helical edge states to an additional spin-degenerate channel. We calculate the slope of the energy phase relation analytically and consider its limit at zero energy in order to define an effective length of the junction. In the next section (Sec. 5.3) we show that this effect is not unique to the system described in Sec. 5.2 by coupling the helical edge states to a single quantum dot and showing that similar effects occur. By treating the coupling to the dot with a scattering matrix approach, we again calculate the slope of the energy phase relation analytically allowing us to define an effective junction length. In Sec. 5.4 we propose to realize the two described models by a Kane-Mele model, which describes 2D hexagonal structures like graphene (with enhanced spin-orbit interaction), silicene, and germanene. In this case the energy phase relations are obtained by numerically diagonalizing the Kane-Mele tight binding model illustrating the effect of in-

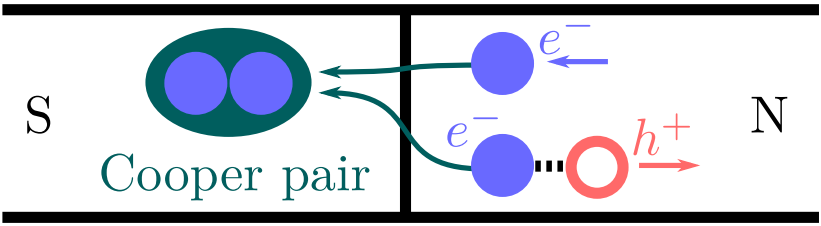

Figure 5.1: Andreev reflection occurs when an electron e^- coming from a normally conducting region N is reflected as a hole h^+ at an interface to a superconductor S. A Cooper pair is created inside of the superconductor in the process.

creasing the effective junction length. Finally, we give a short summary of our findings and outlook in Sec. 5.5.

5.1 Andreev Bound States

When an electron coming from a normal conducting region approaches an interface to a superconducting region, it cannot tunnel into that region if its energy E lies below the superconducting gap Δ as there are no states below that energy inside the superconducting region. It can however enter the superconductor if a second electron with energy $-E$ simultaneously enters the superconductor and forms a Cooper pair with the first electron. During this process called Andreev reflection a hole is reflected at the interface to the superconducting region, which then propagates in the opposite direction to the original electron (Fig. 5.1).

5.1.1 General Case

During this reflection the wave function of the scattered hole acquires a phase shift of [95]

$$-\arccos(E/\Delta) - \phi_i \tag{5.1}$$

with respect to the wave function of the incident electron. Here E is the energy of the electron and ϕ_i the phase of the superconductor at which the electron gets Andreev reflected. When connecting two superconducting regions S with one normally conducting region in an SNS Josephson junction, the Andreev reflected hole will also get Andreev reflected as an electron at the interface to the second superconductor. During this second Andreev reflection the wave function of the reflected electron will acquire an additional phase shift of [95]

$$-\arccos(E/\Delta) + \phi_{i'} \tag{5.2}$$

with respect to the wave function of the incident hole where $\phi_{i'}$ is the phase of the second superconductor.

If the phase picked up in an entire round trip is equal to an integer multiple of 2π

$$\varphi - 2\arccos\left(\frac{E}{\Delta}\right) \pm \phi = 2\pi m, \qquad m \in \mathbb{Z}, \tag{5.3}$$

the wave functions will interfere constructively and a bound state called an Andreev bound state will form. Here $\phi = \phi_i - \phi_{i'}$ is the phase difference between the two superconductors and φ is the phase that the electron and hole pick up while propagating in the normal region N. The sign in front of ϕ in eq. (5.3) results from multiple Andreev bound states being able to form inside the junction. One Andreev bound state forms in the way described above. As the normal region N supports electron transport in both directions, another Andreev bound state can form by propagating

in the opposite direction, i.e. first being Andreev reflected as a hole at the second superconductor which is then being Andreev reflected as an electron at the first superconductor. Solving the relation (5.3) for the Andreev bound state energy E yields the energy phase relation of the Andreev bound states.

As we will see in the remainder of this chapter, coupling the states of the normal region to an additional nondispersive channel or a quantum dot and letting electrons scatter between these systems significantly alters the phase φ and therefore the energy phase relation of the Andreev bound states. Because we want to analyze the effects that such scattering in the normal region has on the effective length of the junction, we will have to define a measure for this effective length. To that end we notice that the slope of the energy phase relation at zero energy in the long junction limit $E_T/2$ with the Thouless energy $E_T = \hbar v_F/L$ is much smaller than the slope in the short junction limit $\Delta/2$. We can therefore use the slope at zero energy to distinguish between junctions that behave more like long junctions and those that behave more like short junctions. Taking the derivative of (5.3) with respect to the energy E yields

$$\begin{aligned} &\partial_E(\varphi) + \frac{2}{\Delta\sqrt{1-\left(\frac{E}{\Delta}\right)^2}} \pm \partial_E(\phi) = 0 \\ &\Rightarrow \partial_E(\phi) = \pm\left[\partial_E(\varphi) + \frac{2}{\Delta\sqrt{1-\left(\frac{E}{\Delta}\right)^2}}\right] \end{aligned} \tag{5.4}$$

which after inverting gives us the slope of the energy phase relation

$$\partial_\phi E = \pm\left[\partial_E(\varphi) + \frac{2}{\Delta\sqrt{1-\left(\frac{E}{\Delta}\right)^2}}\right]^{-1}. \tag{5.5}$$

Using this relation, we can analytically obtain the slope of the energy phase relation even in cases where analytical closed form

solutions for the energy phase relation itself are not possible.

5.1.2 Propagation without Scattering

The eqs. (5.3) and (5.5) are valid in the general case where φ can take any form depending on the system in question and yield the energy phase relation and its slope respectively. When considering the case where electrons and holes only propagate in the normal region and are not coupled to additional systems, the phase picked up during propagation is given by $\varphi = k \cdot x$ where $k = E/\hbar v_F$ is the wave vector of the electron / hole and x is the distance it traveled. The phase picked up in an entire round trip is therefore given by

$$\varphi = \frac{2EL}{\hbar v_F} = 2\frac{E}{E_T} \tag{5.6}$$

so that the condition for the energy phase relation reads

$$2\frac{E}{E_T} - 2\arccos\left(\frac{E}{\Delta}\right) \pm \phi = 2\pi m, \qquad m \in \mathbb{Z}, \tag{5.7}$$

which cannot be solved analytically without further simplifications.

If the distance between the two superconductors L is short compared to the superconducting coherence length $\xi = \hbar v_F/\Delta$, the phase φ can be neglected as $|E| \leq \Delta \ll E_T$. The resulting relation can be solved for the energy E analytically to yield the well-known energy phase relation of short junctions [25, 95, 146]

$$E = \pm\Delta \cos\left(\frac{\phi}{2}\right). \tag{5.8}$$

In the opposite limit, where the distance between the two superconductors is long compared to the superconducting coherence length, we can approximate $\arccos(E/\Delta) \approx \pi/2$ for small

$|E| \ll \Delta$ so that we can again obtain the energy phase relation of the Andreev bound states

$$E = E_T \left(\pi m + \frac{\pi}{2} \pm \frac{\phi}{2} \right) \tag{5.9}$$

which is valid for the first couple of Andreev bound states ($|E| \sim E_T \ll \Delta$).

Inserting eq. (5.6) into eq. (5.5) we can evaluate the slope of the energy phase relation

$$\partial_\phi E = \pm \left[\frac{2}{E_T} + \frac{2}{\Delta \sqrt{1 - \left(\frac{E}{\Delta}\right)^2}} \right]^{-1}, \tag{5.10}$$

which at zero energy simplifies to

$$\begin{aligned} \partial_\phi E|_{E=0} &= \pm \left[\frac{2}{E_T} + \frac{2}{\Delta} \right]^{-1} = \pm \frac{\Delta}{2} \left[1 + \frac{\Delta}{E_T} \right]^{-1} \\ &= \pm \frac{\Delta}{2} \left[1 + \frac{L}{\xi} \right]^{-1}. \end{aligned} \tag{5.11}$$

For short junctions ($\Delta \ll E_T$) the slope is given by

$$\partial_\phi E \approx \pm \frac{\Delta}{2} \sqrt{1 - \left(\frac{E}{\Delta} \right)^2} \xrightarrow{E \to 0} \pm \frac{\Delta}{2} \tag{5.12}$$

whereas in the opposite limit of long junctions ($E_T \ll \Delta$) we can find for the first few Andreev bound states ($|E| \sim E_T \ll \Delta$)

$$\partial_\phi E \approx \pm \frac{E_T}{2}, \tag{5.13}$$

which is much smaller than the slop at zero energy of short junctions. Comparing the slopes at zero energy with these two limits of short and long junctions without scattering will allow us to define effective lengths for junctions including scattering inside the normal region.

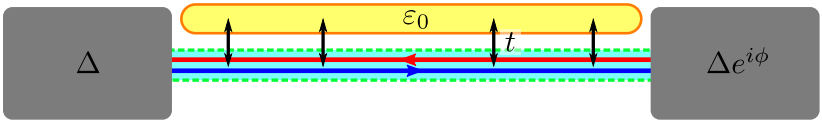

Figure 5.2: Josephson junction mediated by helical edge states (blue and red) that are coupled to an additional nondispersive channel at energy ϵ_0 (yellow).

5.2 Nondispersive Channel

To see how coupling the states facilitating the Josephson effect can result in a gate tunable effective length of the Josephson junction, we consider a system where the helical edge states facilitating the Josephson effect are coupled to a nondispersive spin-degenerate channel at energy ϵ_0 (Fig. 5.2). A proposal for a physical realization of this model will be given in Sec. 5.4. The system between the two superconductors can be described with the Hamiltonian

$$H = \sum_{k\sigma} (\hbar v_F \sigma k - \mu) \psi^\dagger_{k\sigma} \psi_{k\sigma} + (\epsilon_0 - \mu) \sum_{k\sigma} d^\dagger_{k\sigma} d_{k\sigma} + t \sum_{k\sigma} \psi^\dagger_{k\sigma} d_{k\sigma} + \text{H.c.} \tag{5.14}$$

where $\psi_{k\sigma}$ and $d_{k\sigma}$ annihilate and electron with wave vector k and spin polarization σ in the helical edge states and the nondispersive channel respectively. The first (second) term describes the electrons in the helical edge states (nondispersive channel) at chemical potential μ and the third describes tunneling of strength $t \in \mathbb{R}$ between the two subsystems. Because the additional nondispersive channel is not coupled to a lead, the number of fermions and therefore the fermion parity inside the junction does not change by this tunneling. The junction is therefore still frac-

tional and we should expect a 4π periodicity in the energy phase relation.

Rewriting the Hamiltonian as

$$H = \sum_{k\sigma} \Psi^{\dagger}_{k\sigma} \begin{pmatrix} \hbar v_F \sigma k - \mu & t \\ t & \epsilon_0 - \mu \end{pmatrix} \Psi_{k\sigma}, \qquad \Psi_{k\sigma} = \begin{pmatrix} \psi_{k\sigma} \\ d_{k\sigma} \end{pmatrix}, \tag{5.15}$$

we can perform a simple matrix diagonalization to find the eigenstates with corresponding eigenenergies ϵ which are enumerated by their wave vector

$$k = \frac{1}{\hbar v_F \sigma} \left((\epsilon + \mu) + \frac{t^2}{\epsilon_0 - (\epsilon + \mu)} \right). \tag{5.16}$$

When building a Josephson junction mediated by these states like in Fig. 5.2, Andreev bound states will form due to electrons and holes being consecutively Andreev reflected. When propagating in the eigenstates of the normal system, the electrons and holes pick up a phase of $k \cdot x$ where x again is the distance traveled. In an entire round trip the electrons and holes therefore pick up the phase

$$\varphi = \frac{1}{E_T} \left(2E + \frac{t^2}{(\epsilon_0 - \mu) - E} - \frac{t^2}{(\epsilon_0 - \mu) + E} \right). \tag{5.17}$$

Here, we have replaced the eigenenergy ϵ with the Andreev bound state energy E and neglected the overall sign σ as an additional sign in φ does not result in additional solutions to eq. (5.3). The first term is equivalent with the phase picked up in the case without scattering (eq. (5.6)) while the second (third) term arises due to electrons (holes) scattering into the nondispersive channel. The phase φ diverges when the Andreev bound state energy is in resonance with $\pm(\epsilon_0 - \mu)$ which according to eq. (5.3) should result in a vanishing slope of the energy phase relation at that energy.

When looking at the resulting slope of the energy phase relation of the Andreev bound states

$$\frac{\partial E}{\partial \phi} = \pm \left[\frac{1}{E_T} \left(2 + \frac{t^2}{[(\epsilon_0 - \mu) - E]^2} + \frac{t^2}{[(\epsilon_0 - \mu) + E]^2} \right) + \frac{2}{\Delta \sqrt{1 - \left(\frac{E}{\Delta}\right)^2}} \right]^{-1}, \tag{5.18}$$

we see that it vanishes at the resonance energies $E = \pm(\epsilon_0 - \mu)$ in addition to vanishing at the superconducting gap $E = \pm\Delta$. For energies far away from the resonance energies the slope can be approximated by the case without scattering

$$\frac{\partial E}{\partial \phi} \xrightarrow{|E \mp (\epsilon_0 - \mu)| \gg t} \pm \left[\frac{2}{E_T} + \frac{2}{\Delta \sqrt{1 - \left(\frac{E}{\Delta}\right)^2}} \right]^{-1}. \tag{5.19}$$

The scattering into the nondispersive channel therefore only significantly effects the energy phase relation around the resonance energies $\pm(\epsilon_0 - \mu)$.

The connection to the case without scattering becomes even clearer when we consider the slope of the energy phase relation at zero energy

$$\begin{aligned} \left.\frac{\partial E}{\partial \phi}\right|_{E=0} &= \pm \left[\frac{1}{E_T} \left(2 + 2 \frac{t^2}{(\epsilon_0 - \mu)^2} \right) + \frac{2}{\Delta} \right]^{-1} \\ &= \pm \frac{\Delta}{2} \left[1 + \frac{\Delta}{E_T} \left(1 + \left[\frac{t}{\epsilon_0 - \mu} \right]^2 \right) \right]^{-1} \\ &= \pm \frac{\Delta}{2} \left[1 + \frac{L}{\xi} \left(1 + \left[\frac{t}{\epsilon_0 - \mu} \right]^2 \right) \right]^{-1}, \end{aligned} \tag{5.20}$$

which can be written as

$$\left.\frac{\partial E}{\partial \phi}\right|_{E=0} = \pm\frac{\Delta}{2}\left[1+\frac{L_{\text{eff}}}{\xi}\right]^{-1} \tag{5.21}$$

where we have defined the effective length

$$L_{\text{eff}} = L\left(1+\left[\frac{t}{\epsilon_0-\mu}\right]^2\right). \tag{5.22}$$

Around zero energy the junction of length L including scattering into the nondispersive channel therefore features an energy phase relation like a junction of length L_{eff} without scattering.

The effective length L_{eff} is bounded from below by the actual length of the junction L, which can be achieved by tuning the chemical potential far away from the channel energy $|\mu-\epsilon_0| \gg t$. When tuning the chemical potential to lie near the channel energy however $|\mu-\epsilon_0| \ll t$, the effective length of the junction near zero energy increases and can even diverge. That way we can electrically tune a junction that is physically in the short junction limit $L \ll \xi$ to either effectively behave around zero energy like a short junction or like a long junction $L \ll \xi \ll L_{\text{eff}}$.

This effect can be seen when numerically evaluating eq. (5.3) for different chemical potentials (Fig. 5.3). Because the junction is physically in the short junction regime ($L = 0.1\xi$), the energy phase relation resembles that of a short junction when the chemical potential is further away from the channel energy ϵ_0. When tuning the chemical potential closer to the channel energy however, the slope of the energy phase relation at zero decreases and the energy phase relation resembles one of a longer junction.

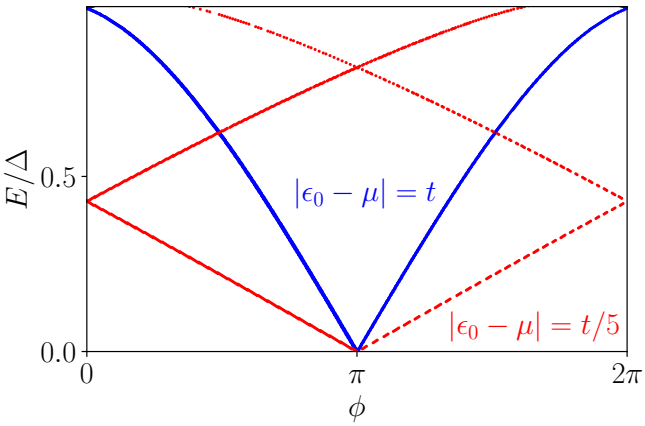

Figure 5.3: Energy phase relation of a Josephson junction of length $L = 0.1\xi$ mediated by spin-helical edge states that are coupled to a nondispersive spin-degenerate channel like in Fig. 5.2 obtained by numerically solving eq. (5.3) together with eq. (5.17) for two different chemical potentials. The numerical solution is obtained by sampling both E and ϕ with equidistant points, calculating both sides of eq. (5.3), and showing only the points, for which the difference between the left and right sides of eq. (5.3) are below a certain threshold. Only positive energies are shown.

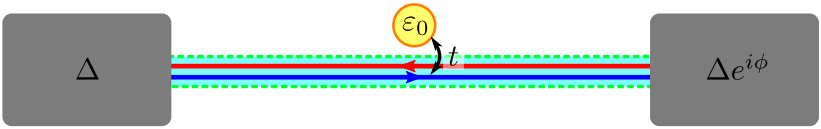

Figure 5.4: Josephson junction mediated by helical edge states (blue and red) that are coupled to a quantum dot at energy ϵ_0 (yellow).

5.3 Quantum Dot

To see that the system described in Sec. 5.2 is not the only one in which such tunability is possible, we shift our focus to a system in which the helical edge states mediating the Josephson effect are coupled to a single quantum dot (Fig. 5.4) instead of an entire nondispersing channel. Such a system is described by the Hamiltonian

$$H = \underbrace{\sum_{k\sigma}(\hbar v_F \sigma k - \mu)\psi^\dagger_{k\sigma}\psi_{k\sigma} + \epsilon_0 \sum_\sigma d^\dagger_\sigma d_\sigma}_{H_0} + \underbrace{\sqrt{\frac{L}{2\pi}}t \sum_\sigma \psi^\dagger_\sigma(0) d_\sigma + \text{H.c.}}_{V} \tag{5.23}$$

where the first part H_0 describes the helical edge states and quantum dot whereas the second part V describes the coupling of strength t between the two. The operators $\psi_{k\sigma}$ and d_σ annihilate an electron in spin polarization σ either in the helical edge states with a wave vector k or on the dot respectively. The coupling is assumed to be local and spin-independent. A proposal for a physical realization of this model will again be given in Sec. 5.4.

Because the system is no longer translationally invariant due

to the local scattering, we can no longer employ the same method to obtain the phase φ picked up while propagating between the two superconductors. Instead, we will use a scattering matrix approach to calculate the phase picked up by considering the eigenstates of the helical edge states without scattering $|k\sigma\rangle$ as incoming and outgoing waves and the dot as the scattering region. The scattering matrix at energy ϵ can be evaluated via the Mahaux-Weidenmüller formula [147–149]

$$S = 1 + 2\pi i W^\dagger \frac{1}{H_0^d - \epsilon - i\pi W W^\dagger} W \tag{5.24}$$

where

$$H_0^d = \epsilon_0 \sum_\sigma d_\sigma^\dagger d_\sigma \tag{5.25}$$

is the Hamiltonian describing the scatterer (quantum dot) and

$$W = \sqrt{\rho} V \tag{5.26}$$

is the scattering part of the Hamiltonian scaled with the density of states

$$\rho = \frac{1}{2\pi} \frac{L}{\hbar v_F} = \frac{1}{2\pi E_T} \tag{5.27}$$

of the helical edge states[1].

As the system is time-reversal symmetric and the helical edge states are spin-helical, an incoming wave cannot be backscattered at the quantum dot. Furthermore, due to energy conservation, the outgoing wave must always have the same wave vector as the incoming wave. The only finite matrix elements of the S-matrix are therefore its diagonal elements

$$S_k := \langle k|S|k\rangle = 1 + 2\pi i \langle k|W^\dagger \frac{1}{H_0^d - \epsilon - i\pi W W^\dagger} W|k\rangle \tag{5.28}$$

[1] Another approach is to express the S-matrix in terms of the T-matrix. Using the Lippmann-Schwinger equation, one can calculate the T-matrix elements via a geometric series.

with $|k\rangle = \psi^\dagger_{k\sigma}|0\rangle$ where $|0\rangle$ denotes the vacuum state. We have neglected the index σ in the helical edge states because the spin is always preserved during a scattering event. The second part can be evaluated by inserting the unity matrix

$$1 = \sum_\mu |\mu\rangle \langle\mu| \tag{5.29}$$

where $\{|\mu\rangle\}$ is the complete and orthonormal set of all possible single electron states, that is either $|k\rangle$ for an electron in a helical edge state or $|d\rangle = d^\dagger_\sigma|0\rangle$ for an electron on the quantum dot. Using this identity, we can find

$$\begin{aligned}\langle k|W^\dagger \frac{1}{H_0^d - \epsilon - i\pi WW^\dagger} W|k\rangle \\ = \sum_{\mu\mu'} \langle k|W^\dagger|\mu'\rangle \langle\mu'| \frac{1}{H_0^d - \epsilon - i\pi WW^\dagger}|\mu\rangle \langle\mu|W|k\rangle .\end{aligned} \tag{5.30}$$

Using the Fourier transformation

$$\psi_\sigma(x) = \sqrt{\frac{2\pi}{L}} \sum_k e^{-ikx}\psi_{k\sigma}, \tag{5.31}$$

we can express the scattering part of the Hamiltonian as

$$W = \sqrt{\rho}\sqrt{\frac{L}{2\pi}}t \sum_\sigma \psi^\dagger_\sigma(0)d_\sigma + \text{H.c.} = \sqrt{\rho}t \sum_{k\sigma} \psi^\dagger_{k\sigma} d_\sigma + \text{H.c.} \tag{5.32}$$

so that

$$\langle\mu|W|k\rangle = \sqrt{\rho}t\delta_{\mu,d}. \tag{5.33}$$

Inserting this into eq. (5.30) yields

$$\begin{aligned}\langle k|W^\dagger \frac{1}{H_0^d - \epsilon - i\pi WW^\dagger} W|k\rangle &= \rho t^2 \langle d| \frac{1}{H_0^d - \epsilon - i\pi WW^\dagger}|d\rangle \\ &= \frac{\rho t^2}{\epsilon_0 - \epsilon - i\pi\rho t^2}\end{aligned} \tag{5.34}$$

with which we can evaluate the S-matrix elements

$$S_k = 1 + \frac{2\pi i \rho t^2}{\epsilon_0 - \epsilon - i\pi\rho t^2}. \tag{5.35}$$

Using some basic algebra, one can show that

$$S_k = e^{i\delta}, \qquad \delta = 2\arg\left\{(\epsilon - \epsilon_0) - i\frac{t^2}{2E_T}\right\}, \tag{5.36}$$

which for $\epsilon \neq \epsilon_0$ simplifies to

$$\delta = -2\arctan\left(\frac{t^2}{2E_T(\epsilon - \epsilon_0)}\right) \tag{5.37}$$

and $\delta = \pm\pi$ if $\epsilon = \epsilon_0$.

The overall phase φ picked up by the electron and hole in a round trip is given by

$$\varphi = \frac{2E}{E_T} - 2\arctan\left(\frac{t^2}{2E_T(E - \epsilon_0)}\right) - 2\arctan\left(\frac{t^2}{2E_T(E + \epsilon_0)}\right) \tag{5.38}$$

where the first term describes propagation without scattering and the second (third) term describes scattering by the electrons (holes) along the dot. Looking at the slope of the energy phase relation

$$\frac{\partial E}{\partial \phi} = \pm\left[\frac{1}{E_T}\left(2 + \frac{t^2}{(E-\epsilon_0)^2 + \left(\frac{t^2}{2E_T}\right)^2} + \frac{t^2}{(E+\epsilon_0)^2 + \left(\frac{t^2}{2E_T}\right)^2}\right) + \frac{2}{\Delta\sqrt{1 - \left(\frac{E}{\Delta}\right)^2}}\right]^{-1}, \tag{5.39}$$

it only vanishes at the superconducting gap $E \to \pm\Delta$, unlike in the case with the nondispersive channel. In the weak coupling limit $t^2 \ll E_T(E \pm \epsilon_0)$ the second term of the denominator resulting from the scattering can be neglected

$$\frac{\partial E}{\partial \phi} \xrightarrow{t^2 \ll E_T(E\pm\epsilon_0)} \pm \left[\frac{1}{E_T} \left(2 + \frac{t^2}{(E-\epsilon_0)^2} + \frac{t^2}{(E+\epsilon_0)^2} \right) + \frac{2}{\Delta\sqrt{1-\left(\frac{E}{\Delta}\right)^2}} \right]^{-1} \tag{5.40}$$

so that the slope has the same form as the case with the nondispersive channel where now the dot energy ϵ_0 acts as the resonance energies. The cases of electrons coupled to a nondispersive channel and of electrons coupled to a single quantum dot can therefore not be distinguished in the energy phase relation in the weak coupling limit.

In the opposite limit of strong coupling $t^2 \gg E_T(E \pm \epsilon_0)$

$$\frac{\partial E}{\partial \phi} \xrightarrow{t^2 \gg E_T(E\pm\epsilon_0)} \pm \left[\frac{2}{E_T} + \frac{2}{\Delta\sqrt{1-\left(\frac{E}{\Delta}\right)^2}} \right]^{-1} \tag{5.41}$$

the slope of the case without scattering is recovered. This at first counterintuitive result can be understood by considering the phase (5.38) in this limit. The phase picked up by an electron or hole due to scattering approaches its maximum value of $\pm\pi$ for strong couplings. As both the electron and hole scatter along the dot, a total phase of $2\pi n$ with $n \in \mathbb{Z}$ is picked up in an entire round trip. However, an additional phase of $2\pi n$ does not change the energy phase relation (see eq. (5.3)) so that the energy phase relation looks as if no scattering took place.

To determine the effective length of this junction, we calculate

the slope of the energy phase relation at zero energy

$$\begin{aligned}\left.\frac{\partial E}{\partial \phi}\right|_{E=0} &= \pm\frac{\Delta}{2}\left[1+\frac{\Delta}{E_T}\left(1+\frac{t^2}{\epsilon_0^2+\left(\frac{t^2}{2E_T}\right)^2}\right)\right]^{-1} \\ &= \pm\frac{\Delta}{2}\left[1+\frac{L}{\xi}\left(1+\frac{t^2}{\epsilon_0^2+\left(\frac{t^2}{2E_T}\right)^2}\right)\right]^{-1}\end{aligned} \tag{5.42}$$

so that the slope at zero energy takes the form

$$\left.\frac{\partial E}{\partial \phi}\right|_{E=0} = \pm\frac{\Delta}{2}\left[1+\frac{L_{\text{eff}}}{\xi}\right]^{-1} \tag{5.43}$$

with the effective length

$$L_{\text{eff}} = L\left(1+\frac{t^2}{\epsilon_0^2+\left(\frac{t^2}{2E_T}\right)^2}\right). \tag{5.44}$$

Just like in the case with the nondispersive channel, the energy phase relation around zero energy of a junction with physical length L including the coupling with the dot looks like the energy phase relation of a junction of length L_{eff} without scattering.

The effective length is again bounded from below by the physical length L of the junction. It can be electrically tuned by changing the energy level of the quantum dot ϵ_0 which is measured from the chemical potential. However, in contrast to the case with a nondispersive channel, the effective length has a maximal value to which it can be electrically tuned by tuning $\epsilon_0 = 0$. In this case the effective length is given by

$$L_{\text{eff}}^{\max} = L\left(1+4\frac{E_T^2}{t^2}\right). \tag{5.45}$$

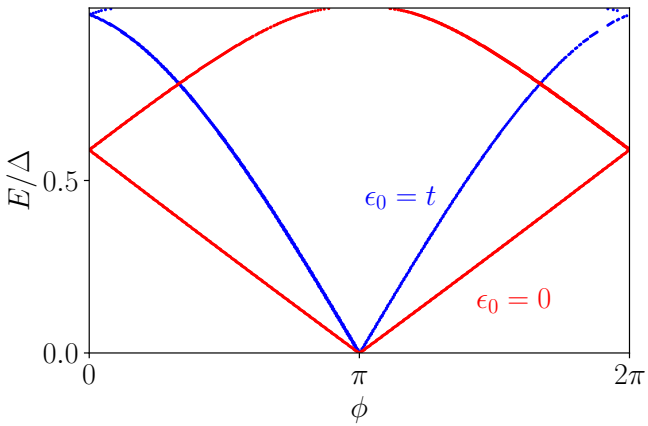

Figure 5.5: Energy phase relation of a Josephson junction of length $L = 0.1\xi$ mediated by spin-helical edge states that are coupled with strength $t = 5\Delta$ to a quantum dot like in Fig. 5.4 obtained by numerically solving eq. (5.3) together with eq. (5.38) in a similar fashion to Fig. 5.3 for two different dot energies ϵ_0. Only positive energies are shown.

In the weak coupling limit this effective length diverges while it approaches L in the strong coupling limit which is consistent with our analysis in eq. (5.41).

The changing of the slope around zero energy when chaining the energy level of the quantum dot can also be seen directly in the energy phase relation (Fig. 5.5), which can be obtained by numerically solving eq. (5.3) together with eq. (5.38). Because the junction is physically in the short junction regime ($L = 0.1\xi$), the energy phase relation resembles that of a short junction when tuning the energy level of the quantum dot ϵ_0 far away from the Andreev bound states energies. When the dot energy level gets lowered, the slope of the energy phase relation diminishes as more Andreev bound states form inside of the junction and the junction resembles a longer one.

5.4 Kane-Mele Model

In the previous two sections we proposed two models in which the effective length of a Josephson junction can be tuned electrically by external gates. We now turn our attention to a potential physical system in which such tunable junctions might be possible. As a realization of spin-helical topological edge states we chose the edge states of the Kane-Mele model (2.34) in the quantum spin Hall insulating regime (see App. C), which describes graphene with enhanced spin-orbit interaction, silicene, germanene, and similar 2D hexagonal structures. We choose the edge to be zigzag terminated (see Fig. 5.6) while additional atoms can be coupled to the zigzag edge [145].

5.4.1 Nondispersive Channel

In order to model the nondispersive channel discussed in Sec. 5.2, we couple additional atoms to the edge like in Fig. 5.6. Because the added atoms do not couple among each other, these added atoms form a nondispersive channel which is coupled to the edge of the sample hosting the topological edge states. By numerically implementing this tight binding model, the energy phase relation can be obtained via matrix diagonalization (Fig. 5.7).

For chemical potentials away from the channel energy ϵ_0 the energy phase relation around zero energy has a slope of $\approx \pm\Delta/2$ as the junction is physically in the short junction regime $L = 0.1\xi$. Just like analytically predicted and also seen in the numerical solution in Fig. 5.3, the slope around zero energy decreases when tuning the chemical potential to be closer to the channel energy ϵ_0. However, the slope for $|\epsilon_0 - \mu| = t/5$ in the Kane-Mele model (Fig. 5.7) is still larger as analytically predicted. Furthermore,

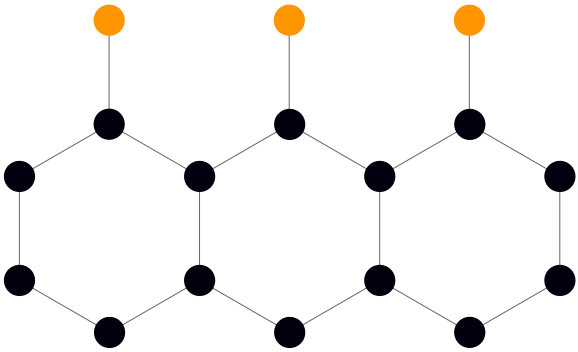

Figure 5.6: The spin-helical edge states are realized by the Kane-Mele model describing a single sheet of graphene or similar structures (black) in a zigzag edge configuration. Additional atoms (yellow) are coupled to the zigzag edge which do not couple to each other and form the nondispersive channel.

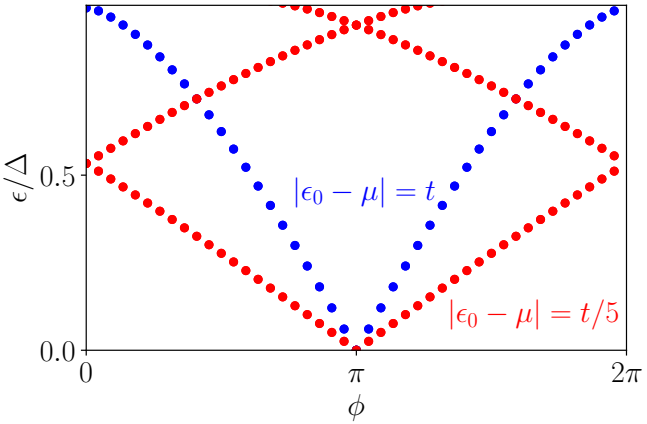

Figure 5.7: Energy phase relation of a Josephson junction of length $L = 0.1\xi$ mediated by helical edge states coupled to a nondispersive channel at energy ϵ_0 obtained by numerically solving the Kane-Mele tight binding model for two different chemical potentials μ.

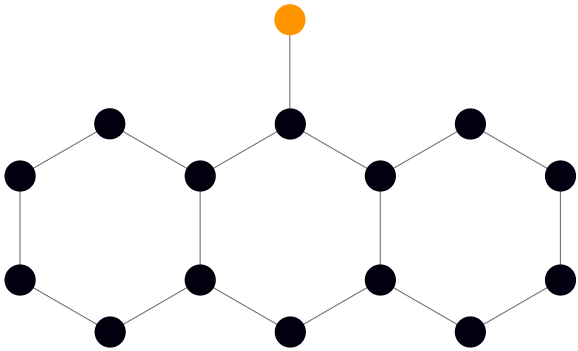

Figure 5.8: The spin-helical edge states are realized by the Kane-Mele model describing a single sheet of graphene or similar structures (black) in a zigzag edge configuration. The quantum dot coupled to the helical edge states can be modeled by a single added atom (yellow) coupled to the zigzag edge.

according to eq. (5.21) the slope should approach zero when tuning the chemical potential to coincide with the channel energy. However, the slope stays finite in this case in the Kane-Mele model. This discrepancy can be explained by the fact, that the model discussed in Sec. 5.2 is only an idealized model for the Kane-Mele model such that quantitatively equal results cannot be expected. Regardless, the results observed in the Kane-Mele model and the model discussed in Sec. 5.2 are qualitatively similar.

5.4.2 Quantum Dot

A physical realization for the second model looked at in Sec. 5.3 can be achieved in a similar fashion (Fig. 5.8). Instead of coupling many atoms to the zigzag edge to form a nondispersive channel, we now only couple a single atom to the edge. This

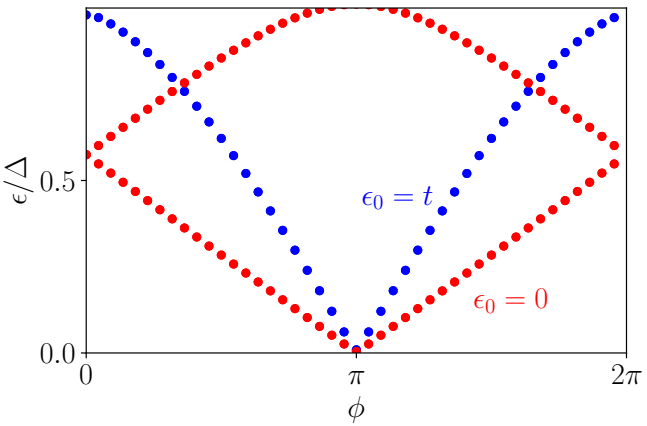

Figure 5.9: Energy phase relation of a Josephson junction of length $L = 0.1\xi$ mediated by helical edge states coupled with strength $t = 5\Delta$ to a quantum dot at energy ϵ_0 obtained by numerically solving the Kane-Mele tight binding model for two different dot energies ϵ_0.

single atom has a single energy level at energy ϵ_0 and describes a quantum dot. Just like in the case with the nondispersive channel, we can obtain the energy phase relation via a matrix diagonalization (Fig. 5.9)

The resulting energy phase relations match the ones obtained by numerically solving eq. (5.3) (Fig. 5.5) and have slopes around zero energy that follow the analytical prediction (5.43). Unlike the case with the nondispersive channel, higher order hopping terms do not effect the energy phase relation because there is only a single quantum dot.

The Kane-Mele model in a zigzag edge configuration with additional atoms added to the edge is therefore a possible physical realization of two models described in Sec. 5.2 and 5.3. By changing either the chemical potential (first setup) or the quantum dot energy (second setup) the energy phase relation gets changed in

a way that resembles a different distance L_{eff} between the two superconductors. This effective junction length is well described by the analytical results obtained in Sec. 5.2 and 5.3 as long as the hopping t between the channel and the zigzag edge is not to large in the first case.

5.5 Conclusion

In this chapter we have proposed two models in which the effective length of a Josephson junction mediated by spin-helical edge states can be tuned electrically by external electric gates. In the first proposed setup the spin-helical edge states are coupled to a spin-degenerate nondispersive channel. When tuning the chemical potential of the region between the two superconductors to be far away from the energy of the channel, the coupling to the channel does not change the energy phase relation of the Andreev bound states of the junction. However, if the chemical potential is tuned close to the channel energy, the energy phase relation of the junction will change. The resulting energy phase relation resembles that of a junction which has a longer distance between the two superconductors than the studied junction. We calculated the effective length of the junction by evaluating the slope of the energy phase relation of the Andreev bound states at zero energy.

In the second proposed setup the spin-helical edge states couple only to a single quantum dot. By tuning the dot energy by an external electrical gate the effective length of the junction can again be tuned. Similarly to the first setup, by tuning the dot energy far away from the Andreev bound states the energy phase relation of the Andreev bound states are unaffected by the scattering between the helical edge states and the quantum

dot. However, by tuning the dot energy towards zero energy the energy phase relation again changes in a way that resembles a junction with an increased distance between the two superconductors. We again calculated the effective junction length by analyzing the slope of the energy phase relation of the Andreev bound states around zero energy. With both setups the effective length of the Josephson junction can be increased by external electrical gates. This increase in effective junction length is bound in the case with the quantum dot while it grows boundless when the coupling is to a nondispersive channel.

As a possible physical realization of these models we proposed the Kane-Mele model in the quantum spin Hall insulating regime as a realization for the spin-helical edge states. This model describes the electronic properties of 2D systems such as graphene (with enhanced spin-orbit interaction), silicene, germanene, and similar 2D hexagonal structures. As an example realization of a spin-degenerate nondispersive channel or a quantum dot we proposed to couple additional atoms to a zigzag terminated edge. These additional atoms in turn form a nondispersive channel. If only a single atom is coupled to the zigzag edge, this atom will realize a single level quantum dot. Such coupling of additional atoms to the zigzag edge of the Kane-Mele model can potentially be achieved by functionalizing structures like graphene. Both the functionalization of the basal plane [150–153], as well as the edge [154, 155] of graphene have received considerable attention in the recent past.

We treated this model numerically and have seen that the growth of the effective junction length is indeed observed in both cases. However, the growth of the junction length is bounded by a maximum effective junction length even in the case with many atoms added to the zigzag edge as higher order hopping terms effectively couple the added atoms and turn the modeled channel dispersive.

Finally, it is important to note that adding atoms to the

zigzag edge is not the only way to realize the additional channel or quantum dot. Instead, by utilizing the electric tunability of structures like silicene (see Chap. 3) spin-helical channels can be defined by electric gates. Furthermore, when these edge states form around a small region, these edge states quantize to discrete energy levels [156–160]. If the size of the region around which these edge states form is small enough, the energy gap between energy levels will be large enough to neglect higher energy levels so that the resulting system can be treated as a single quantum dot.

6

Conclusion

In this thesis we have developed and discussed new methods of characterizing fractional Josephson junctions hosting Majorana excitations.

In the first setup we considered a Josephson junction in silicene. Due to the buckled structure of silicene, we can tune the topology of individual regions in silicene by external gates. Using this tunability, we devised a scheme in which topological edge states forming at the boundary of two such regions can be electrically tuned between being spin-helical and spin-degenerate. When building a Josephson junction mediated by these topological edge states, Andreev bound states form inside of the junc-

tion. While the energy phase relation of these Andreev bound states is 4π periodic when the edge states are spin-helical, intervalley scattering reduces this periodicity to 2π in the case of spin-degenerate edge states. As this change in periodicity coincides with the destruction of Majorana excitations inside of the junction, it can be used to indicate the junction changing from a fractional topological state hosting Majorana excitations to a nonfractional nontopological state without Majorana excitations.

The 4π periodicity of the energy phase relation of fractional Josephson junctions depends on the fermion parity being conserved inside such junctions. Experiments to unveil this topological nature of the Josephson junction are therefore dependent on the fermion parity being conserved. This parity is however generally broken by quasiparticle poisoning. To analyze and characterize this quasiparticle poisoning was the goal of the second proposed setup where we described the dynamics of such topological Josephson junctions with an RSJ model and included quasiparticle poisoning events into this model through multiple means. We found that the critical current in long junctions differs by a factor of two when switching between topological and nontopological junctions even when the parity changes result in excitations of the junction rather than relaxations. We furthermore developed multiple schemes through which the quasiparticle poisoning rate can be measured via voltage measurements. As the quasiparticle poisoning rate plays an important role in the stability of topological qubits build out of Majorana excitations, this last result is of particular interest to characterizing Josephson junctions.

Many of the proposed effects of the second setup rely on the junction to be in the long junction limit. Some of the currently manufactured junctions do however potentially lie in the short to intermediate junction limit, making such measurements impossible. To overcome this limitation, we proposed to couple an additional channel or a single quantum dot to the helical edge states mediating the Josephson effect in a third setup. With

such a coupling, the resulting energy phase relation changes in a way that resembles a Josephson junction that is longer than it physically is. By electrically tuning either the chemical potential or the quantum dot level energy, we can tune the effective length of the resulting Josephson junction. As a potential physical realization we proposed the Kane-Mele model in the quantum spin Hall insulating regime, which describes structures like graphene with enhanced spin-orbit interaction. In this model the channel and quantum dot can be achieved by coupling additional atoms to the sample edge of a sheet of e.g. graphene. However, similar setups can be achieved by again utilizing the electric tunability of silicene to electrically define channels or localized levels inside of a sheet of silicene.

All three setups discussed in this thesis represent a means to characterize fractional Josephson junctions but approach the problem from different angles. The first setup aims to provide an experimental scheme by which we can electrically tune between fractional and nonfractional Josephson junctions. That way, experiments performed to distinguish the topology of a junction can be done in a single sample rather than relying on multiple manufactured samples that differ in some system parameter to achieve both topological and nontopological junctions. The second setup proposes a way to experimentally measure the quasiparticle poisoning rate. Furthermore it addresses the question of the parameter regime quasiparticle poisoning can be in while still being able to determine the topology of long Josephson junctions through measuring its critical current. As both of the first two setups either benefit from or entirely rely on the junction to lie in the long junction limit, our third setup addresses this limitation by proposing a means to effectively increase the length of a Josephson junction.

Finally, it is important to note that this study of means to characterize fractional Josephson junctions is by no means exhaustive. First, the material system discussed in Chap. 3 is not

the only system in which a junction with the desired tunability can be created. Setups based on double layer quantum wells in HgTe or InAs/GaSb are predicted to be electrically tunable in a similar manner to silicene [99–101]. It would be interesting to generalize the concept devised in Chap. 3 to more readily available material systems. How the intervalley scattering necessary to produce the desired results arises e.g. out of random disorder is also an avenue for further investigations.

Furthermore, the analysis of Chap. 4 focused on dc measurements. However, as many experiments rely on ac properties of Josephson junctions, it is of general interest how the effects of quasiparticle poisoning discussed in Chap. 4 apply to this ac regime. Of particular interest is its effects on the existence of Shapiro steps, specifically on the existence of odd Shapiro steps, as the absence of these odd steps is an indication of topology of the underlying Josephson junction.

Also, the setup discussed in Chap. 5 only looked at the energy phase relation of junctions. Further research needs to be done into how the described scattering affects other important quantities such as the total energy of the junction or the current phase relation. The latter is particularly interesting as the current is a directly measurable quantity. Another interesting question is if and how other types of fermion parity preserving scattering can potentially be engineered to achieve arbitrary tunability of the effective junction length. Overall, the field of finding signatures of topology in Josephson junctions and characterization of said junctions is still ripe with unexplored avenues and possibilities and may play a key role in the building of future superconducting quantum devices.

Appendices

A

Values for Numerical Simulation of Chap. 3

In Chap. 3 we perform numerical simulations based on the tight binding models (2.32) and (2.34). When simulations were performed with the discretized low energy model (2.32) both the spin helical and spin degenerate regimes were considered and resulted in two different parameter choices (see Tab. A.1). In both regimes all energies are therefore measured in multiples of $\hbar v_F/b$. When simulations were performed with the tight binding model on a hexagonal lattice (2.34) only the spin helical regime was considered resulting in only a single set of parameters (see Tab. A.2)

Parameter	**Spin Helical Regime**	**Spin Degenerate Regime**
$\frac{\hbar v_F}{b}$	1	1
m_1	0.5	-0.5
m_2	1	1
t_s	0.5	0.5
Δ_{SO}	0.75	0
Δ	0.2	0.2
δ	0	0.05

Table A.1: Numeric values chosen for the simulations in Chap. 3 using the discretized low energy model (2.32) for both the spin helical and spin degenerate regime.

In this case all energies are measured in multiples of the hopping energy t. Unless stated otherwise in the main text these parameters were chosen for all respective simulations.

Parameter	**Value**
t	1
m_1	1
m_2	0.5
Δ_{SO}	0.75
Δ	0.2

Table A.2: Numeric values chosen for the simulations in Chap. 3 using the tight binding model on a hexagonal lattice (2.34).

B

Integral over two Lorentz-Cauchy Distributions

In the derivation of the tunneling rate between two helical edges in Sec. 4.6 we have used the relation

$$\int d\varepsilon L[\varepsilon + a, \gamma] L[\varepsilon + b, \delta] = L[a - b, \gamma + \delta] \tag{B.1}$$

multiple times. To validate this equation we rewrite the Lorentz-Cauchy distribution as

$$L[\varepsilon,\gamma] = \frac{1}{\pi}\frac{\gamma}{\varepsilon^2+\gamma^2} = \frac{\gamma}{\pi}\frac{1}{(\varepsilon+i\gamma)}\frac{1}{(\varepsilon-i\gamma)}, \tag{B.2}$$

which has two poles at $\varepsilon = \pm i\gamma$ and is analytic elsewhere in the complex plane. Inserting this into the left hand side of eq. (B.1) we get

$$\int d\varepsilon L[\varepsilon+a,\gamma]L[\varepsilon+b,\delta] = \frac{\gamma\delta}{\pi^2}\chi \tag{B.3}$$

with the integral

$$\chi = \int d\varepsilon \frac{1}{(\varepsilon+a+i\gamma)}\frac{1}{(\varepsilon+a-i\gamma)}\frac{1}{(\varepsilon+b+i\delta)}\frac{1}{(\varepsilon+b-i\delta)} \tag{B.4}$$

to be evaluated. The integrand has four poles at $\varepsilon = -a \pm i\gamma$ and $\varepsilon = -b \pm i\delta$ and is analytic elsewhere in the complex plane. When performing a contour integral along the real axis and closing the contour in the upper complex half plane ($\Im(\varepsilon) > 0$), two of the four poles at $\varepsilon = -a+i\gamma$ and $\varepsilon = -b+i\delta$ get enclosed in the closed contour. Because the integrand vanishes in the upper complex half plane for large absolute values $|\varepsilon|$, the integral χ is equal to this contour integral. The residua of the integrand at the two enclosed poles are

$$\frac{1}{2i\gamma}\frac{1}{(b-a)+i(\gamma+\delta)}\frac{1}{(b-a)+i(\gamma-\delta)} \tag{B.5}$$

at $\varepsilon = -a+i\gamma$ and

$$\begin{aligned} &\frac{1}{(a-b)+i(\delta+\gamma)}\frac{1}{(a-b)+i(\delta-\gamma)}\frac{1}{2i\delta} \\ =&\frac{1}{2i\delta}\frac{1}{(b-a)-i(\delta+\gamma)}\frac{1}{(b-a)+i(\gamma-\delta)}, \end{aligned} \tag{B.6}$$

at $\varepsilon = -b + i\delta$. Adding these two residua together yields

$$\begin{aligned}
&\frac{1}{2i}\frac{1}{(b-a)+i(\gamma-\delta)} \\
&\qquad\qquad \left[\frac{1}{\gamma}\frac{1}{(b-a)+i(\gamma+\delta)} + \frac{1}{\delta}\frac{1}{(b-a)-i(\delta+\gamma)}\right] \\
=&\frac{1}{2i}\frac{1}{(b-a)+i(\gamma-\delta)}\frac{1}{\gamma\delta} \\
&\qquad\qquad \frac{\delta[(b-a)-i(\delta+\gamma)]+\gamma[(b-a)+i(\gamma+\delta)]}{(b-a)^2+(\gamma+\delta)^2} \\
=&\frac{1}{2i}\frac{1}{(b-a)+i(\gamma-\delta)}\frac{1}{\gamma\delta}\frac{(b-a)(\delta+\gamma)+i(\delta+\gamma)(\gamma-\delta)}{(b-a)^2+(\gamma+\delta)^2} \\
=&\frac{1}{2i}\frac{1}{(b-a)+i(\gamma-\delta)}\frac{1}{\gamma\delta}\frac{(\delta+\gamma)[(b-a)+i(\gamma-\delta)]}{(b-a)^2+(\gamma+\delta)^2} \\
=&\frac{1}{2i}\frac{1}{\gamma\delta}\frac{(\delta+\gamma)}{(b-a)^2+(\gamma+\delta)^2} \\
=&\frac{1}{2i}\frac{\pi}{\gamma\delta}L[a-b,\gamma+\delta]
\end{aligned} \tag{B.7}$$

so that the integral evaluates to

$$\chi = 2\pi i\frac{1}{2i}\frac{\pi}{\gamma\delta}L[a-b,\gamma+\delta] = \frac{\pi^2}{\gamma\delta}L[a-b,\gamma+\delta]. \tag{B.8}$$

Inserting this into eq. (B.3) we finally get

$$\int d\varepsilon L[\varepsilon+a,\gamma]L[\varepsilon+b,\delta] = \frac{\gamma\delta}{\pi^2}\frac{\pi^2}{\gamma\delta}L[a-b,\gamma+\delta] = L[a-b,\gamma+\delta] \tag{B.9}$$

which proves the relation (B.1).

C

Values for Numerical Simulation of Chap. 5

In Chap. 5 we performed numerical simulations based on the tight binding model of the hexagonal lattice (2.34). The values taken for these simulations can be taken from Tab .C.1. All energies are therefore measured in multiples of the spin orbit interaction strength Δ_{SO}. Here t_h refers to the hopping energy of the Kane-Mele model on the hexagonal lattice and t to the hopping energy between the zigzag edge of the Kane-Mele model and the atoms coupled to the edge. It is important to note that especially in the case of the nondispersive channel it might be physically more

Parameter	**Value**
Δ_{SO}	1
t_h	$\frac{2}{\sqrt{3}}$
Δ	0.01
μ	0
t	0.1

Table C.1: Numeric values chosen for the simulations in Chap. 5 using the tight binding model on a hexagonal lattice (2.34).

realistic to change the chemical potential μ and leave the channel energy ϵ_0 unchanged. As all results shown only depend on the absolute difference $|\epsilon_0 - \mu|$ we have chosen to fix the chemical potential $\mu = 0$ and instead vary the channel energy ϵ_0. Unless stated otherwise in the main text these parameters were chosen for all simulations.

Bibliography

[1] R. P. Feynman, Int. J. Theor. Phys. **21**, 467 (1982).

[2] C. Nayak, S. H. Simon, A. Stern, M. Freedman, and S. Das Sarma, Rev. Mod. Phys. **80**, 1083 (2008).

[3] P. W. Shor, in Proceedings 35th annual symposium on foundations of computer science (1994), pp. 124–134.

[4] M. Nielsen and I. Chuang, *Quantum computation and quantum information: 10th anniversary edition* (Cambridge University Press, 2010).

[5] D. P. DiVincenzo, Fortschr. Phys. **48**, 771 (2000).

[6] P. O. Boykin, T. Mor, M. Pulver, V. Roychowdhury, and F. Vatan, in 40th annual symposium on foundations of computer science (1999), pp. 486–494.

[7] D. Deutsch and R. Penrose, P. R. Soc. Lond. A Mat. **400**, 97 (1985).

[8] D. Deutsch and R. Jozsa, P. R. Soc. Lond. A Mat. **439**, 553 (1992).

[9] R. Cleve, A. Ekert, C. Macchiavello, and M. Mosca, P. R. Soc. Lond. A Mat. **454**, 339 (1998).

[10] P. W. Shor, Phys. Rev. A **52**, R2493 (1995).

[11] A. R. Calderbank and P. W. Shor, Phys. Rev. A **54**, 1098 (1996).

[12] A. Steane, P. R. Soc. Lond. A Mat. **452**, 2551 (1996).

[13] D. Gottesman, Phys. Rev. A **57**, 127 (1998).

[14] D. Aharonov and M. Ben-Or, in Proceedings of the twenty-ninth annual acm symposium on theory of computing, STOC '97 (1997), pp. 176–188.

[15] J. M. Leinaas and J. Myrheim, Nuovo Ciment. B **37**, 1 (1977).

[16] G. A. Goldin, R. Menikoff, and D. H. Sharp, J. Math. Phys. **22**, 1664 (1981).

[17] Y.-S. Wu, Phys. Rev. Lett. **52**, 2103 (1984).

[18] A. Kitaev, Ann. Phys. New York **303**, 2 (2003).

[19] P. A. M. Dirac, P. R. Soc. Lond. A-Conta. **117**, 610 (1928).

[20] E. Majorana, Nuovo Cimento **5**, 171 (1937).

[21] F. Wilczek, Nat Phys. **5**, 614 (2009).

[22] N. Read and D. Green, Phys. Rev. B **61**, 10267 (2000).

[23] A. Y. Kitaev, Phys. Usp. **44**, 131 (2001).

[24] L. Fu and C. L. Kane, Phys. Rev. Lett. **100**, 096407 (2008).

[25] L. Fu and C. L. Kane, Phys. Rev. B **79**, 161408 (2009).

[26] R. M. Lutchyn, J. D. Sau, and S. Das Sarma, Phys. Rev. Lett. **105**, 077001 (2010).

[27] Y. Oreg, G. Refael, and F. von Oppen, Phys. Rev. Lett. **105**, 177002 (2010).

[28] A. C. Potter and P. A. Lee, Phys. Rev. Lett. **105**, 227003 (2010).

[29] X.-L. Qi and S.-C. Zhang, Rev. Mod. Phys. **83**, 1057 (2011).

[30] J. Alicea, Rep. Prog. Phys. **75**, 076501 (2012).

[31] C. Beenakker, Annu. Rev. Conden. Ma. P. **4**, 113 (2013).

[32] C. W. J. Beenakker, SciPost Phys. Lect. Notes, 15 (2020).

[33] S. D. Sarma, M. Freedman, and C. Nayak, npj Quantum Inf. **1**, 15001 (2015).

[34] F. Zhang and C. L. Kane, Phys. Rev. Lett. **113**, 036401 (2014).

[35] C. P. Orth, R. P. Tiwari, T. Meng, and T. L. Schmidt, Phys. Rev. B **91**, 081406 (2015).

[36] J. Alicea and P. Fendley, Annu. Rev. Conden. Ma. P. **7**, 119 (2016).

[37] Y. Vinkler-Aviv, P. W. Brouwer, and F. von Oppen, Phys. Rev. B **96**, 195421 (2017).

[38] C. Fleckenstein, N. T. Ziani, and B. Trauzettel, Phys. Rev. Lett. **122**, 066801 (2019).

[39] S. R. Elliott and M. Franz, Rev. Mod. Phys. **87**, 137 (2015).

[40] V. Mourik, K. Zuo, S. M. Frolov, S. R. Plissard, E. P.A. M. Bakkers, and L. P. Kouwenhoven, Science **336**, 1003 (2012).

[41] K. T. Law, P. A. Lee, and T. K. Ng, Phys. Rev. Lett. **103**, 237001 (2009).

[42] K. Flensberg, Phys. Rev. B **82**, 180516 (2010).

[43] S. Nadj-Perge, I. K. Drozdov, B. A. Bernevig, and A. Yazdani, Phys. Rev. B **88**, 020407 (2013).

[44] S. Nadj-Perge, I. K. Drozdov, J. Li, H. Chen, S. Jeon, J. Seo, A. H. MacDonald, B. A. Bernevig, and A. Yazdani, Science **346**, 602 (2014).

[45] L. P. Rokhinson, X. Liu, and J. K. Furdyna, Nat. Phys. **8**, 795–799 (2012).

[46] J. Wiedenmann, E. Bocquillon, R. S. Deacon, S. Hartinger, O. Herrmann, T. M. Klapwijk, L. Maier, C. Ames, C. Brüne, C. Gould, A. Oiwa, K. Ishibashi, S. Tarucha, H. Buhmann, and L. W. Molenkamp, Nat. Commun. **7**, 10303 (2016).

[47] E. Bocquillon, R. S. Deacon, J. Wiedenmann, P. Leubner, T. M. Klapwijk, C. Brüne, K. Ishibashi, H. Buhmann, and L. W. Molenkamp, Nat. Nanotechnol. **12**, 137 (2017).

[48] R. S. Deacon, J. Wiedenmann, E. Bocquillon, F. Domínguez, T. M. Klapwijk, P. Leubner, C. Brüne, E. M. Hankiewicz, S. Tarucha, K. Ishibashi, H. Buhmann, and L. W.
Molenkamp, Phys. Rev. X **7**, 021011 (2017).

[49] D. Laroche, D. Bouman, D. J. van Woerkom, A. Proutski, C. Murthy, D. I. Pikulin, C. Nayak, R. J. J. van Gulik, J. Nygård, P. Krogstrup, L. P. Kouwenhoven, and A. Geresdi, Nat. Commun. **10**, 245 (2019).

[50] M. König, S. Wiedmann, C. Brüne, A. Roth, H. Buhmann, L. W. Molenkamp, X.-L. Qi, and S.-C. Zhang, Science **318**, 766 (2007).

[51] S. Shapiro, Phys. Rev. Lett. **11**, 80 (1963).

[52] D. Frombach, S. Park, A. Schroer, and P. Recher, Phys. Rev. B **98**, 205305 (2018).

[53] A. Schuray, D. Frombach, S. Park, and P. Recher, Eur. Phys. J. Spec. Top. **229**, 593 (2020).

[54] D. Frombach and P. Recher, Phys. Rev. B **101**, 115304 (2020).

[55] C. L. Kane and E. J. Mele, Phys. Rev. Lett. **95**, 226801 (2005).

[56] H. Min, J. E. Hill, N. A. Sinitsyn, B. R. Sahu, L. Kleinman, and A. H. MacDonald, Phys. Rev. B **74**, 165310 (2006).

[57] C.-C. Liu, H. Jiang, and Y. Yao, Phys. Rev. B **84**, 195430 (2011).

[58] A. H. Castro Neto, F. Guinea, N. M. R. Peres, K. S. Novoselov, and A. K. Geim, Rev. Mod. Phys. **81**, 109 (2009).

[59] B. Bernevig and T. Hughes, *Topological insulators and topological superconductors* (Princeton University Press, 2013).

[60] G. Giovannetti, P. A. Khomyakov, G. Brocks, P. J. Kelly, and J. van den Brink, Phys. Rev. B **76**, 073103 (2007).

[61] B. Sachs, T. O. Wehling, M. I. Katsnelson, and A. I. Lichtenstein, Phys. Rev. B **84**, 195414 (2011).

[62] N. D. Drummond, V. Zólyomi, and V. I. Fal'ko, Phys. Rev. B **85**, 075423 (2012).

[63] M. Ezawa, New J. Phys. **14**, 033003 (2012).

[64] M. Ezawa, J. Phys. Soc. Jpn. **84**, 121003 (2015).

[65] S. K. Wang, J Wang, and K. S. Chan, New J. Phys. **16**, 045015 (2014).

[66] C. Wu, B. A. Bernevig, and S.-C. Zhang, Phys. Rev. Lett. **96**, 106401 (2006).

[67] C. Xu and J. E. Moore, Phys. Rev. B **73**, 045322 (2006).

[68] J. C. Budich, F. Dolcini, P. Recher, and B. Trauzettel, Phys. Rev. Lett. **108**, 086602 (2012).

[69] T. L. Schmidt, S. Rachel, F. von Oppen, and L. I. Glazman, Phys. Rev. Lett. **108**, 156402 (2012).

[70] W. Chen, W.-Y. Deng, J.-M. Hou, D. N. Shi, L. Sheng, and D. Y. Xing, Phys. Rev. Lett. **117**, 076802 (2016).

[71] I. Belopolski, S.-Y. Xu, N. Koirala, C. Liu, G. Bian, V. N. Strocov, G. Chang, M. Neupane, N. Alidoust, D. Sanchez, H. Zheng, M. Brahlek, V. Rogalev, T. Kim, N. C. Plumb, C. Chen, F. Bertran, P. Le Fèvre, A. Taleb-Ibrahimi, M.-C. Asensio, M. Shi, H. Lin, M. Hoesch, S. Oh, and M. Z. Hasan, Sci. Adv. **3** (2017).

[72] L. Susskind, Phys. Rev. D **16**, 3031 (1977).

[73] H. Nielsen and M. Ninomiya, Phys. Lett. B **105**, 219 (1981).

[74] B. Messias de Resende, F. C. de Lima, R. H. Miwa, E. Vernek, and G. J. Ferreira, Phys. Rev. B **96**, 161113 (2017).

[75] Y.-F. Zhou, H. Jiang, X. C. Xie, and Q.-F. Sun, Phys. Rev. B **95**, 245137 (2017).

[76] C. W. Groth, M. Wimmer, A. R. Akhmerov, and X. Waintal, New J. Phys. **16**, 063065 (2014).

[77] C. L. Kane and F. Zhang, Phys. Scr. **T164**, 014011 (2015).

[78] C. W. J. Beenakker, D. I. Pikulin, T. Hyart, H. Schomerus, and J. P. Dahlhaus, Phys. Rev. Lett. **110**, 017003 (2013).

[79] F. Crépin and B. Trauzettel, Phys. Rev. Lett. **112**, 077002 (2014).

[80] J. Pachos, *Introduction to topological quantum computation* (Cambridge University Press, 2012).

[81] D. Rainis and D. Loss, Phys. Rev. B **85**, 174533 (2012).

[82] F Geissler, J. C. Budich, and B Trauzettel, New J. Phys. **15**, 085030 (2013).

[83] J. Wang, Y. H. Yang, and K. S. Chan, Phys. Rev. B **89**, 064501 (2014).

[84] S. Rachel and M. Ezawa, Phys. Rev. B **89**, 195303 (2014).

[85] J. Wang, L. Hao, and J.-F. Liu, Phys. Rev. B **93**, 155405 (2016).

[86] H. Li, R. Wang, and C. S. Ting, Phys. Rev. B **94**, 085422 (2016).

[87] D. Kuzmanovski, J. Linder, and A. Black-Schaffer, Phys. Rev. B **94**, 180505 (2016).

[88] J. Linder and T. Yokoyama, Phys. Rev. B **89**, 020504 (2014).

[89] X. Zhou and G. Jin, Phys. Rev. B **95**, 195419 (2017).

[90] E. McCann, K. Kechedzhi, V. I. Fal'ko, H. Suzuura, T. Ando, and B. L. Altshuler, Phys. Rev. Lett. **97**, 146805 (2006).

[91] M. Z. Hasan and C. L. Kane, Rev. Mod. Phys. **82**, 3045 (2010).

[92] I. Martin, Y. M. Blanter, and A. F. Morpurgo, Phys. Rev. Lett. **100**, 036804 (2008).

[93] A. Schroer, P. G. Silvestrov, and P. Recher, Phys. Rev. B **92**, 241404 (2015).

[94] J. B. Oostinga, L. Maier, P. Schüffelgen, D. Knott, C. Ames, C. Brüne, G. Tkachov, H. Buhmann, and L. W. Molenkamp, Phys. Rev. X **3**, 021007 (2013).

[95] Y. Nazarov and Y. Blanter, *Quantum transport: introduction to nanoscience* (Cambridge University Press, 2009).

[96] C. Ishii, Prog. Theor. Phys. **44**, 1525 (1970).

[97] J. Bardeen and J. L. Johnson, Phys. Rev. B **5**, 72 (1972).

[98] A. V. Svidzinsky, T. N. Antsygina, and E. N. Bratus', J. Low Temp. Phys. **10**, 131 (1973).

[99] P. Michetti, J. C. Budich, E. G. Novik, and P. Recher, Phys. Rev. B **85**, 125309 (2012).

[100] C. Liu, T. L. Hughes, X.-L. Qi, K. Wang, and S.-C. Zhang, Phys. Rev. Lett. **100**, 236601 (2008).

[101] F. Qu, A. J. A. Beukman, S. Nadj-Perge, M. Wimmer, B.-M. Nguyen, W. Yi, J. Thorp, M. Sokolich, A. A. Kiselev, M. J. Manfra, C. M. Marcus, and L. P. Kouwenhoven, Phys. Rev. Lett. **115**, 036803 (2015).

[102] V. Krueckl and K. Richter, Phys. Rev. Lett. **107**, 086803 (2011).

[103] I. Knez, R.-R. Du, and G. Sullivan, Phys. Rev. Lett. **109**, 186603 (2012).

[104] I. Knez, R.-R. Du, and G. Sullivan, Phys. Rev. Lett. **107**, 136603 (2011).

[105] J. B. Oostinga, H. B. Heersche, X. Liu, A. F. Morpurgo, and L. M. K. Vandersypen, Nat. Mater. **7**, 151 (2008).

[106] M. T. Allen, J. Martin, and A. Yacoby, Nat. Commun. **3**, 934 (2012).

[107] M. Eich, R. Pisoni, H. Overweg, A. Kurzmann, Y. Lee, P. Rickhaus, T. Ihn, K. Ensslin, F. c. v. Herman, M. Sigrist, K. Watanabe, and T. Taniguchi, Phys. Rev. X **8**, 031023 (2018).

[108] J. Klinovaja, G. J. Ferreira, and D. Loss, Phys. Rev. B **86**, 235416 (2012).

[109] M. Gmitra and J. Fabian, Phys. Rev. B **92**, 155403 (2015).

[110] J. Y. Khoo, A. F. Morpurgo, and L. Levitov, Nano Lett. **17**, 7003 (2017).

[111] A. M. Alsharari, M. M. Asmar, and S. E. Ulloa, Phys. Rev. B **97**, 241104 (2018).

[112] H.-J. Kwon, V. M. Yakovenko, and K. Sengupta, Low Temp. Phys. **30**, 613 (2004).

[113] J. Alicea, Y. Oreg, G. Refael, F. von Oppen, and M. P. A. Fisher, Nat. Phys. **7**, 412 (2011).

[114] J. C. Budich, S. Walter, and B. Trauzettel, Phys. Rev. B **85**, 121405 (2012).

[115] J. Männik and J. E. Lukens, Phys. Rev. Lett. **92**, 057004 (2004).

[116] J. Aumentado, M. W. Keller, J. M. Martinis, and M. H. Devoret, Phys. Rev. Lett. **92**, 066802 (2004).

[117] M. Leijnse and K. Flensberg, Semicond. Sci. Tech. **27**, 124003 (2012).

[118] D. M. Badiane, M. Houzet, and J. S. Meyer, Phys. Rev. Lett. **107**, 177002 (2011).

[119] M. Houzet, J. S. Meyer, D. M. Badiane, and L. I. Glazman, Phys. Rev. Lett. **111**, 046401 (2013).

[120] P. San-Jose, E. Prada, and R. Aguado, Phys. Rev. Lett. **108**, 257001 (2012).

[121] F. Domínguez, F. Hassler, and G. Platero, Phys. Rev. B **86**, 140503 (2012).

[122] B. van Heck, F. Hassler, A. R. Akhmerov, and C. W. J. Beenakker, Phys. Rev. B **84**, 180502 (2011).

[123] D. I. Pikulin and Y. V. Nazarov, Phys. Rev. B **86**, 140504 (2012).

[124] P. Virtanen and P. Recher, Phys. Rev. B **88**, 144507 (2013).

[125] P. San-Jose, J. Cayao, E. Prada, and R. Aguado, New J. Phys. **15**, 075019 (2013).

[126] J. D. Sau and F. Setiawan, Phys. Rev. B **95**, 060501 (2017).

[127] P. Russer, J. Appl. Phys. **43**, 2008 (1972).

[128] M. Tinkham, *Introduction to superconductivity*, International series in pure and applied physics (McGraw Hill, 1996).

[129] S. Hart, H. Ren, T. Wagner, P. Leubner, M. Mühlbauer, C. Brüne, H. Buhmann, L. W. Molenkamp, and A. Yacoby, Nat. Phys. **10**, 638–643 (2014).

[130] F. Domínguez, O. Kashuba, E. Bocquillon, J. Wiedenmann, R. S. Deacon, T. M. Klapwijk, G. Platero, L. W. Molenkamp, B. Trauzettel, and E. M. Hankiewicz, Phys. Rev. B **95**, 195430 (2017).

[131] J. Picó-Cortés, F. Domínguez, and G. Platero, Phys. Rev. B **96**, 125438 (2017).

[132] S.-P. Lee, K. Michaeli, J. Alicea, and A. Yacoby, Phys. Rev. Lett. **113**, 197001 (2014).

[133] Y. Peng, F. Pientka, E. Berg, Y. Oreg, and F. von Oppen, Phys. Rev. B **94**, 085409 (2016).

[134] V. Ambegaokar and B. I. Halperin, Phys. Rev. Lett. **22**, 1364 (1969).

[135] P. Hänggi, P. Talkner, and M. Borkovec, Rev. Mod. Phys. **62**, 251 (1990).

[136] D. G. Olivares, A. L. Yeyati, L. Bretheau, Ç.Ö. Girit, H. Pothier, and C. Urbina, Phys. Rev. B **89**, 104504 (2014).

[137] B. Baxevanis, V. P. Ostroukh, and C. W. J. Beenakker, Phys. Rev. B **91**, 041409 (2015).

[138] G. Tkachov, P. Burset, B. Trauzettel, and E. M. Hankiewicz, Phys. Rev. B **92**, 045408 (2015).

[139] T. H. Galambos, S. Hoffman, P. Recher, J. Klinovaja, and D. Loss, arXiv: 2004.01733 (2020).

[140] V. S. Pribiag, A. J. A. Beukman, F. Qu, M. C. Cassidy, C. Charpentier, W. Wegscheider, and L. P. Kouwenhoven, Nat. Nanotechnol. **10**, 593 (2015).

[141] J. Strunz, J. Wiedenmann, C. Fleckenstein, L. Lunczer, W. Beugeling, V. L. Müller, P. Shekhar, N. T. Ziani, S. Shamim, J. Kleinlein, H. Buhmann, B. Trauzettel, and L. W. Molenkamp, Nat. Phys. **16**, 83 (2019).

[142] T. Karzig, C. Knapp, R. M. Lutchyn, P. Bonderson, M. B. Hastings, C. Nayak, J. Alicea, K. Flensberg, S. Plugge, Y. Oreg, C. M. Marcus, and M. H. Freedman, Phys. Rev. B **95**, 235305 (2017).

[143] Y. Peng, Y. Vinkler-Aviv, P. W. Brouwer, L. I. Glazman, and F. von Oppen, Phys. Rev. Lett. **117**, 267001 (2016).

[144] A. Das, Y. Ronen, Y. Most, Y. Oreg, M. Heiblum, and H. Shtrikman, Nat. Phys. **8**, 887 (2012).

[145] M. Malki and G. S. Uhrig, Phys. Rev. B **95**, 235118 (2017).

[146] C. W. J. Beenakker, Phys. Rev. Lett. **67**, 3836 (1991).

[147] C. Mahaux and H. A. Weidenmüller, *Shell-model approach to nuclear reactions* (North-Holland Publishing Company, 1969).

[148] J. Nilsson, A. R. Akhmerov, and C. W. J. Beenakker, Phys. Rev. Lett. **101**, 120403 (2008).

[149] M. Sumetsky, Phys. Rev. A **100**, 013801 (2019).

[150] C. K. Chua and M. Pumera, Chem. Soc. Rev. **42**, 3222 (2013).

[151] M. Pumera and C. H. A. Wong, Chem. Soc. Rev. **42**, 5987 (2013).

[152] S. Eigler and A. Hirsch, Angew. Chem. Int. Edit. **53**, 7720 (2014).

[153] C. Zhou, S. Chen, J. Lou, J. Wang, Q. Yang, C. Liu, D. Huang, and T. Zhu, Nanoscale Res. Lett. **9**, 26 (2014).

[154] A. Bellunato, H. Arjmandi Tash, Y. Cesa, and G. F. Schneider,
ChemPhysChem **17**, 785 (2016).

[155] Z. Xiang, Q. Dai, J.-F. Chen, and L. Dai, Adv. Mater. **28**, 6253 (2016).

[156] Z.-F. Jiang and W.-Y. Shan, arXiv:0908.0890 (2009).

[157] R.-L. Chu, J. Li, J. K. Jain, and S.-Q. Shen, Phys. Rev. B **80**, 081102 (2009).

[158] J. Maciejko, E.-A. Kim, and X.-L. Qi, Phys. Rev. B **82**, 195409 (2010).

[159] P. Michetti and P. Recher, Phys. Rev. B **83**, 125420 (2011).

[160] G. Tkachov and E. M. Hankiewicz, Phys. Rev. B **83**, 155412 (2011).